DISSERTATION

VEGETATION AND LITHOLOGIC INFLUENCES ON CHANNEL MORPHOLOGY IN THE SOUTHWESTERN U.S.

Submitted by

Celeste Wieting

Department of Geosciences

In partial fulfillment of the requirements

For the Degree of Doctor of Philosophy

Colorado State University

Fort Collins, Colorado

Summer 2024

Doctoral Committee:

Advisor: Sara Rathburn

Ellen Wohl
Dan McGrath
Ryan Morrison
Jonathan Friedman

ABSTRACT

VEGETATION AND LITHOLOGIC INFLUENCES ON CHANNEL MORPHOLOGY

IN THE SOUTHWESTERN U.S.

Vegetation and lithology play critical roles in shaping landscapes, creating diverse river and gully morphologies. Vegetation stabilizes banks and alters flow dynamics. In the Southwestern United States, non-native, invasive plant species contributed to regional trends of river channel narrowing and simplification and degraded diverse riparian habitats throughout the 20th century. More recently, efforts to remove invasive riparian vegetation (IRV) have been widespread, especially since 1990. Restoration practitioners who perform IRV treatments often focus on wildlife or vegetation response; however, geomorphic processes should be considered in restoration planning because they drive flow, sediment transport, and aquatic habitat and vegetation dynamics, and because of the potential for damage to downstream people and infrastructure. Depending on the restoration goal, management practices can be used to enhance or minimize the increase in channel dynamism caused by IRV removal.

At the river reach scale, I investigated biogeomorphic feedbacks at one of the 15 previously analyzed study sites, the Rio Grande in Texas. Along the Rio Grande in Big Bend National Park (BIBE), restoration goals to remove invasive giant cane (*Arundo donax*) include decreasing channel narrowing and increasing water and sediment conveyance. Recent work has indicated that removal of giant cane has successfully reduced its extent, but the geomorphic effects of giant cane treatment and subsequent revegetation are still not well understood. A

general lack of reach-scale studies of riparian plant pronation during flow inundation and the biogeomorphic feedbacks between plants, flow, and sediment transport contribute to this knowledge gap. I quantified morphological-effect plant traits for three common riparian plant species: invasive giant cane, native baccharis (*Baccharis salicifolia*), and native phragmites (*Phragmites australis*). I collected data at the plant, plot, and reach scales and created upright and flexible frontal area and vegetation roughness curves using photographs of plants and stem counts of plots. Then, I used these data in a reach-scale 2D hydraulic model to simulate species-specific effects and the effects of giant cane removal on channel hydraulics. Results indicate that the mean vegetation roughness is similar for all three species at the plant scale, but at the plot scale, vegetation roughness is higher for giant cane and phragmites due to higher stem densities. Hydraulic modeling results suggest that vegetation increased velocities in the center of the channel and decreased velocities on the channel margins. When all the vegetation was represented as giant cane, reach-scale water surface elevations were the highest and reach-scale velocities the lowest. Removing giant cane decreased water surface elevations, indicating increased conveyance.

To determine the effects of IRV removal on a regional scale across the Southwest U.S., treated and untreated reaches at 15 sites along 13 rivers were compared before and after IRV treatment using repeat aerial imagery to assess long-term (~10 year) channel change. Resolving observations of channel change into separate measures of floodplain destruction and formation provided more information on underlying processes than simple measurements of channel width and centerline migration rate. IRV treatment significantly increased channel width and floodplain destruction. Treated reaches had higher floodplain destruction than untreated reaches at 14 of 15 sites, and IRV treatment increased floodplain destruction by a median factor of 1.9. The effect of

treatment increased with the stream power of the largest flow over the study period. From the results, I suggest that restoration managers consider the system's susceptibility to change, downstream threats, and desired process changes when defining their geomorphic restoration goal because treatment of a dominant species over a large area can be expected to have major fluvial geomorphic consequences.

In addition to vegetation, the lithology and surficial sediment properties influence hydrological processes, sediment transport, and gully and channel morphology. In semi-arid environments where vegetation is lacking, and precipitation is sufficient to drive erosion, sediment yields tend to be greatest. Increased landscape erosion is predicted as more extreme weather causes frequent or intense rainfall, and flooding. In Wupatki National Monument (WUPA), heavy rainstorms over the past decade, lack of vegetation, and presence of unconsolidated volcanic-derived cinders expose archaeological sites to erosion, a concern to cultural resource managers. To identify archaeological sites of highest vulnerability to erosion, I analyzed gully morphologic change over a 5-year period. I found that 35 measured gullies are actively eroding, with statistically significant changes in gully depth from 2016 to 2021. Up to 0.5 m of incision was documented over a five-year period. A structure-from-motion analysis at the hillslope scale confirmed gully morphological changes and supports the applicability of conducting similar analyses on a larger scale. More erosion occurred in gullies with catchments predominantly covered with cinders because of cinder mobility. A weak relationship was noted between gully catchment area and gully head slope, likely related to runoff processes from outcrops of resistant sedimentary rocks forming cliffs and characteristics of cinders that maximize infiltration and transport. Based on assessment of gully morphologic change and

substrate characteristics, 22 archaeological sites along Wupatki Wash were identified as having a high vulnerability to erosion.

ACKNOWLEDGEMENTS

I would like to first thank my family. My husband, Colin, believed in me, cheered me on, and provided unwavering support throughout this journey. He was willing to come home early from work for the entire Spring semester to take care of our son Augie, while I would work evenings. He was always willing to help when I had questions about fluvial processes or even hydraulic modeling. Words cannot describe how indebted I am to him for all of his support and help. The love and support of my parents has also been a driving force behind my success. They are extremely hard working and inspiring in both their careers and personal life, and that has continued to motivate me to succeed. Augie has also motivated me, and I hope one day he is proud of his mom for completing this degree.

Thank you to members of the CSU community who helped me along the way, including Shayla “Aunt Yaya” Triantafillou and Danny White. Aunt Yaya watched Augie while I had meetings, cooked me dinner when I was too busy to cook, and was always there to listen and support. I would have finished years from now without Danny’s help, still trying to write code on my own. He not only assisted with coding challenges but also provided invaluable insights, particularly in navigating the unique experience of balancing parenthood with doctoral studies. I will never forget the many trips we did together and the many meetings we had trying to figure out how to model plants bending over in water.

Thank you to my committee, especially Jonathan Friedman. Without Jonathan, I would not have been able to finish my first manuscript. Jonathan was extremely helpful with addressing reviewer comments, interpreting statistical results, editing our first manuscript, and so much more. He knew that I was taking care of a newborn and needed all the help I could ask for. For my fourth chapter, Jonathan’s help was invaluable. Jonathan helped me in the field and was the

one who spearheaded the idea of collecting data at the plant- and plot-scale, which turned out to be extremely important. He met with me weekly for a few months straight to talk about converting our plant data into vegetation roughness curves. His genuine love and curiosity of everything related to plants is heart-warming and inspiring.

Lastly, thank you to my advisor, Sara Rathburn. Sara offered guidance and encouragement along the way and enabled me to pursue my research interests. We created unforgettable memories together while in the field and I wouldn't have been able to complete this degree without her. She has played an important role in shaping my career and I am forever grateful to her mentorship, support, and friendship.

DEDICATION

I dedicate this dissertation to my son, August (Augie) Barry. Te amo mucho. Besos.

TABLE OF CONTENTS

ABSTRACT ii
ACKNOWLEDGEMENTS vi
DEDICATION viii
CHAPTER 1: INTRODUCTION 1
References 5
CHAPTER 2: A MULTISCALE ANALYSIS OF VEGETATION INFLUENCES ON CHANNEL HYDRAULICS ALONG THE RIO GRANDE IN BIG BEND NATIONAL PARK[1] 8
2.1 Introduction 8
2.1.1 Previous Research on the Relationships Between Vegetation and Flow Hydraulics 10
2.1.2 Previous Rio Grande Research in BIBE 13
2.1.3 Research Questions and Hypotheses 14
2.1.4 Study Area 16
2.2 Methods 19
2.2.1 Field Data Collection 19
2.2.2 Field Data Analysis 23
2.3 Results 38
2.3.1 Plant and plot traits 38
2.3.2 Depth-varied vegetation roughness 43
2.3.3 Vegetation on flood surfaces 45
2.3.3 Hydraulic Modeling 48
2.4 Discussion 53
2.4.1 Plant and plot scale data 53
2.4.2 Hydraulic modeling 58
2.4.3 Management Implications 60
2.4.4 Limitations and Future Work 63
2.5 Conclusions 66
References 68
CHAPTER 3: RIVER CHANNEL RESPONSE TO INVASIVE PLANT TREATMENT ACROSS THE AMERICAN SOUTHWEST[2] 79
3.1 Introduction 79

3.2 Methods 83
3.2.1 Study Region and Reaches 83
3.2.2 Aerial imagery collection 88
3.2.3 Change metrics 89
3.2.4 Statistical and hydrologic analyses 93
3.3 Results 94
3.4 Discussion 98
3.5 Management Implications 102
3.6 Conclusions 105
References 106
CHAPTER 4: EVALUATION OF GULLY EROSION FOR ARCHAEOLOGICAL PRESERVATION IN WUPATKI NATIONAL MONUMENT[3] 116
4.1 Introduction 116
4.2 Previous Research 117
4.3 Study Objectives 118
4.4 Study Area 119
4.4.1 Site Characteristics 119
4.5 Study Methods 126
4.5.1 Baseline Geomorphological Data Collection 126
4.5.2 Topographic Data Collection and Landscape Analyses 128
4.5.3 Archaeological Site Vulnerability Assessment 132
4.6 Results 134
4.6.1 Cinder and Moenkopi-derived sediment differences 134
4.6.2 Catchment Data 137
4.6.3 Slope-Area Analysis and Gully Prediction 138
4.6.4 Gully Change Analysis 139
4.7 Discussion and Conclusions 143
4.7.1 Discussion 143
4.7.2 Conclusions 146
References 148
CHAPTER 5: CONCLUSION 153
APPENDIX A: CHAPTER TWO SUPPLEMENTARY MATERIALS 155
SA1. Derivation of vegetation roughness for use in SRH-2D modeling 165

APPENDIX B: CHAPTER THREE SUPPLEMENTARY MATERIALS 166
APPENDIX C: CHAPTER FOUR SUPPLEMENTARY MATERIALS 167

LIST OF TABLES

Table 2.1. Modeling scenarios outlining roughness and plant configurations, and corresponding inlet discharge. 29
Table 2.2. Manning's n values for channel roughness during calibration runs at flow discharges of 18.5 m^3/s and 244 m^3/s. The floodplain roughness for the upland regions was kept constant assuming that flow would not reach these regions during calibration and because data in these regions were lacking. Shaded rows highlight calibrated (and validated) roughness values used in hydraulic modeling analyses. 34
Table 2.3. Summary of morphological-effect plant and plot traits. Individual plant and plot traits are provided in Appendix A, Tables A3 and A4. 41
Table 2.4. Summary of mean maximum flexible plant and plot vegetation roughness and where those maximums occur within the flow column (Figure 13). 44
Table 2.5. The percentage of total area each plant species occupies on geomorphic surfaces within the study reach. The sum of these total areas suggests that 65% of the mapped geomorphic surfaces are covered by vegetation. AC refers to active channel, and FS1, FS2, and FS3 refer to flood surfaces 1, 2 and 3, respectively. 45
Table 2.6. Approximate inundating discharges (m^3/s) for specific plant species with respect to geomorphic units. The last row shows the median inundating discharge for each geomorphic surface. 46
Table 2.7. Non-normalized median frontal area and flexural rigidity comparisons for upright individual plants between this study and others. 55
Table 3.1. Characteristics of study sites where IRV was treated along >1 km reach of river (RO = Russian olive, TAM = Tamarisk, GC: Giant cane, WP = Whole-plant, CS = Cut-stump, HH = Helicopter herbicide). 86
Table 3.2. Peak stream discharge information obtained from USGS stream gaging stations near study sites. Unit stream power was calculated using the peak discharge, the channel slope (Table 2.1), and the pre-treated average channel width. 87
Table 3.3. Aerial imagery information used in the analysis of change metrics including imagery source, spatial resolution, and the year the imagery was collected (HRO = High-resolution Orthoimagery, NAPP = National Aerial Photography Program, NAIP = National Agriculture Imagery Program, MAI = Multispectral Aerial Imagery). 89
Table 3.4. Summary of change metrics and calculation methods using ArcGIS Pro. Each of the metrics was calculated using pre- and post-treated imagery in the treated and untreated reaches. To calculate the four change metrics, channel area, length, and width were first calculated from the delineated channel polygon. The units of all metrics are meters of change in channel or floodplain width or centerline location. 93
Table 3.5. Comparison of untreated and treated reaches using the Wilcoxon Signed Rank Test. A low test statistic, W, indicates a strong effect of the change metric variable. 95
Table 3.6. Linear model results for change metrics using stream power as the predictor variable. Stream power and change metrics were log transformed to meet model assumptions. 97

Table A1. Stem count data for vegetation plots. These data were used to calculate upright and deflected frontal area at the plot scale. 156
Table A2. Plant characteristics used to calculate deflected frontal area and vegetation roughness. 158
Table A3. Plot characteristics used to calculate deflected frontal area and vegetation roughness. 158
Table A4. Elevation statistics for each plant species-geomorphic surface combination with respect to the 2018 low-water surface elevation. 159
Table A5. Summary statistics of flow depth and velocity within vegetated regions across all simulated discharges. 160
Table A6. Summary statistics of flow depth and velocity within the active channel across all simulated discharges. 161
Table A7. Summary statistics of flow depth and velocity within the unvegetated floodplain across all simulated discharges. 163
Table B1. Archaeological site vulnerability assessment based on proximity to cliff bands and measured gullies. 167
Table B2. A summary table of gully catchment characteristics and erosion ranking of yellow, orange, and red based on the change in median elevation (Figure 17). Additionally, archaeological sites that fell within the buffered region of a gully are provided. 170

LIST OF FIGURES

Figure 2.1. Conceptual diagrams illustrate (A) plant/plot height versus cumulative upright frontal area for non-native giant cane and native phragmites and baccharis. The additional drag caused by plants is proportional to frontal area, and the cumulative upright frontal area and plant height is higher for giant cane compared to native phragmites and baccharis. Considering the higher drag from giant cane, (B) vegetation roughness of giant cane is higher. As flexible plants become inundated, frontal area decreases and vegetation roughness also decreases. 16
Figure 2.2. Location map of Boquillas Canyon study area along the Rio Grande and Texas-Mexico border. Sand bar locations correspond to monumented study sites. The red box outlines the study reach used within the flood surface-vegetation analysis and hydraulic model. 19
Figure 2.3. Examples of edited photos to use within ELA for quantifying upright plant frontal area. Images are of giant cane (left) and baccharis (right). 21
Figure 2.4. Measuring the force-displacement relationship for a baccharis plant to calculate flexural rigidity. 22
Figure 2.5. ArcGIS PRO model builder workflow to create overlapping geomorphic and vegetation point data. 27
Figure 2.6. Modeling scenarios to quantify the influence of species-specific native and invasive vegetation, and the effect of invasive removal, on hydraulics. A no-vegetation scenario (1) was used to compare against vegetated scenarios (2-6). All vegetation polygons (shown in green) were mapped as giant cane in scenario 2, baccharis for scenario 3, and phragmites for scenario 4. A realistic distribution of giant cane, baccharis, and phragmites is represented in scenario 5. Lastly, giant cane is removed and native baccharis and phragmites remain in scenario 6. 30
Figure 2.7. Generalized distribution of common riparian vegetation found in the study area on flood surfaces near the channel. Inundating flows for each flood surface, determined from Blythe (2018), were used to design model scenario flows (Q1-Q5). 31
Figure 2.8. Downstream boundary condition stage-discharge rating curve for Reach 1 including bars 6 and 7. The original rating curve was created by Blythe (2018) and was adjusted for this study for topographic agreement between all topographic-related datasets in the hydraulic model analysis. 32
Figure 2.9. Spatially varied calibrated manning's roughness values for the channel. Calibrated values arose from increasing baseline bed roughness values by 40% to minimize RMSE between measured and modeled WSE at 244 m^3/s. 36
Figure 2.10. Map depicting the cross-section (XS) location (solid black line) used to analyze model results. The cross-section overlaps monumented sand bar 6 on river left and intersects patches of vegetation on river right. 37
Figure 2.11. Average non-normalized upright frontal area curves for individual plants. These curves are essentially the raw data from the photographs of plants taken with a red background. 39
Figure 2.12. Relationships between (a) plant height and non-normalized upright frontal area, and (b) average stem diameter and flexural rigidity. Average stem diameter data are from stem sample collections. 40

Figure 2.13. Frontal area curves for upright (top) and flexible (bottom) plants. Curves are normalized by plant canopy area. Solid lines represent individual plants and the dashed line represents the mean. 42
Figure 2.14. Frontal area curves for upright (top) and flexible (bottom) plots. Curves are normalized by plot area. Solid lines represent individual plants and the dashed line represents the mean. 43
Figure 2.15. Depth-varied vegetation roughness for specific plant species calculated at the individual plant and plot scales. 44
Figure 2.16. Maps of (A) geomorphic units (Blythe, 2018), and (B) vegetation units in the modeled study reach. 47
Figure 2.17. Cumulative histograms of detrended elevation for Giant Cane, Baccharis, Phragmites and all surface cover types on the (a) active channel, (b) flood surface 1, and (c) flood surface 2 48
Figure 2.18. Mean values for flow depth and velocity within (left) vegetated regions, (middle) the active channel, and (right) the unvegetated floodplain. These data along with median, standard deviation, minimum, and maximum are included in Appendix A, Tables A5-A7. 49
Figure 2.19. A comparison of the influence of vegetation (Scenario 5) to the no-vegetation scenario (Scenario 1) at the reach scale and at a cross section at Bar 6 for (a) 200 m^3/s, (b) 500 m^3/s, and (c) 1490 m^3/s. 50
Figure 2.20. Reach-scale velocity results for scenarios 2-4 at a simulated discharge of 200 m^3/s. Cross-section results include both depth and velocity for each scenario. 51
Figure 2.21. Reach-scale effects of giant cane removal on velocity. Cross-section results include both depth and velocity for each scenario. 52
Figure 2.22. Centerline WSEs for different modeling scenarios. WSE converges at the downstream boundary of the modeled reach due to the stage-discharge rating curve boundary condition. 53
Figure 2.23. A comparison of the vegetation roughness curves calculated for flexible plants in this study and others. 58
Figure 3.1. Study sites within the SW showing dominant IRV type at each site. Study site numbers correspond to the information provided in Table 2.1. The Lake Mead and Lake Powell reservoirs are not shown. River lines are sourced from the "USA major rivers" shapefile from ESRI. 84
Figure 3.2. Example of untreated (green) and treated (black) reach locations along the Pecos River in Texas. 85
Figure 3.3. Conceptual diagram of change metrics measured and calculated using ArcGIS Pro. Yellow and green polygons are generated using the symmetrical-difference tool in ArcGIS Pro by overlaying pre- and post-treated polygons to quantify floodplain destruction and floodplain formation in treated and untreated reaches. Blue polygons are generated using the feature-to-polygon tool in ArcGIS Pro and sum the area between the pre- and post-treatment channel centerlines to quantify centerline migration. Channel width is measured by dividing channel area by channel length. 92
Figure 3.4. Floodplain destruction (A), floodplain formation (B), width difference (C), and migration (D) for treated (black) and untreated (green) reaches by study site. 96

Figure 3.5. Boxplots showing the effect of treatment through floodplain destruction, formation, width difference, and migration change metrics. Boxes represent the interquartile range (IQR) between the first and third quartiles, thick horizontal line represents the median, horizontal lines represent minimum and maximum values, and individual points represent extreme values that are greater than 1.5*IQR. 97
Figure 3.6. Determining a geomorphic restoration goal: How much of an increase in channel activity is desired when IRV is removed? This determination is based on consideration of desired process changes, downstream threats, and susceptibility of the system to change. Susceptibility to change is a function of the hydrologic regime and channel characteristics. For example, if threats and susceptibility to geomorphic change are both high and there is not an interest in promoting the occurrence of disturbance-dependent native vegetation, then the practitioner may choose to minimize any increase in channel activity resulting from IRV treatment using techniques described in the text. 104
Figure 4.1. Drainage basin map of Deadman and Wupatki Washes. The callout box displays the confluence of the main Wupatki and Deadman Wash channels, near the WUPA Visitor Center. 121
Figure 4.2. Monthly precipitation totals at WUPA, summarized from daily precipitation data. Daily precipitation and other weather data come from COOP station ID USC00029542, located within the monument. 122
Figure 4.3. The August 15, 2022 rainstorm (1.67 inches in 30 minutes) is the equivalent to a 100- to 200-year precipitation event (NOAA, 2023). 123
Figure 4.4. Map illustrating locations of points (P) and recesses (R) formed by linear cliff bands of Moenkopi Formation. Map adapted from Anderson (2021). 124
Figure 4.5. Conceptual diagram of the interaction between local geology and hydrological processes including infiltration, overland flow, and runoff. Following a rainstorm, water flows on the surface of catchments as either non-channelized or minor channelized overland flow, pours over cliff bands of Moenkopi sandstone, flows down hillslopes through rockfall, and eventually concentrates in gullies formed within cinder deposits on top of Moenkopi bedrock. Gully heads generally form near the base of rockfall material where channels initiated in cinder deposits. Depending on surface conditions in the gully catchment, I expect differences in the runoff response following a rainstorm (upper left graph): quicker, flashier runoff in catchments composed of predominantly Moenkopi sediments and bedrock compared to a more delayed and muted runoff response from catchments covered with cinders. 125
Figure 4.6. Classification of gullies at WUPA (red boxes) using the elementary gully classification proposed by Thwaites et al. (2021). Gully erosion classifications including “erosion activity” and “dominant process” were investigated within this study and thus not outlined. 126
Figure 4.7. The locations of 35 total gullies surveyed within WUPA and nearby archeological resources. 128
Figure 4.8. Example of topographic surveying methods used at each gully. (A) Surveys began at the top of the catchment, proceeded down the center of the catchment, and down the channel centerline. (B) Three cross-sections across the channel near the top, middle, and bottom of the gully were also surveyed. Yellow dots illustrate examples of points used for gully width and

depth calculations for a single cross-section. For gully width, the top of bank locations was used and for gully depth, the vertical distance was calculated between the cross-section minimum elevation (bottom point) and lower of the two top bank elevations. 129
Figure 4.9. Grid system used for collecting photographs for SfM analysis. 132
Figure 4.10. Flowchart used to assign erosion vulnerability classifications to archaeological sites. 133
Figure 4.11. Cumulative infiltration curves from infiltrometer experiments. Less water infiltrated into the Moenkopi-dominated sediments compared to the cinder-dominated, and at a slower rate. 134
Figure 4.12. Estimates of hydraulic conductivity for various soil types derived from cumulative infiltration data collected in the field using the infiltrometer. Van Genuchten parameters for sand were used for calculation of hydraulic conductivity of cinders. 135
Figure 4.13. Grain size distribution plots for gullies with bed and banks made of cinders (left) and Moenkopi-sediments (right). 136
Figure 4.14. Map of gully catchment areas. The catchment area for gully 15 extends South beyond this image. 137
Figure 4.15. Slope-area relationship for 21 of the 35 measured gullies that all contained cliff bands and formed within cinders. The linear regression (solid red line) was shifted downward to the base of the data to create a gully erosion threshold (dashed red line). The values of the threshold coefficient and scaling exponent are 0.10 and 0.13, respectively. Data collected from Grand Canyon National Park are from Pederson et al. (2006). 138
Figure 4.16. Barplots comparing gully geometries from 2016 to 2021. Gully depth (top) and width (bottom) are shown. 139
Figure 4.17. Change in median elevation from 2016 to 2021. All measured gullies had a negative MED suggesting widespread erosion. 140
Figure 4.18. Gully slope changes from 2016 to 2021. The slope of gully 23 changed the most, decreasing from 0.15 to 0.12. 141
Figure 4.19. Results from a DEM of Differencing (DoD) analysis using 2016 aerial LiDAR and 2021 iPhone imagery. A semi-transparent hill shade of the 2016 DEM was used as the background. White polygons indicate where vegetation was manually removed from the imagery. Refer to Figure 3.7 for the location of the DoD analysis. 142
Figure A1. Edited plant photographs used to calculate upright frontal area of (a) giant cane, (b) baccharis, and (c) phragmites. Red scale bars were used to iteratively calculate frontal area with increasing plant height based on pixel size. 155
Figure A2. Non-normalized cumulative frontal area curves for individual upright plants. These curves are essentially the raw data from the photographs of plants taken with a red background. 156
Figure A3. Cauchy versus flow depth at the plant scale (top) and plot scale (bottom) for giant cane, baccharis, and phragmites. 159
Figure B1. Example of active channel delineations at the untreated (top) and treated (bottom) reaches of the Pecos River NM site. This example highlights a portion of the reach where a large change in channel morphology occurred due to IRV treatment. The channel was delineated and

then a centerline was mapped using pre-treated imagery in 2009 (left) and post-treated imagery in 2020 (right). 166

CHAPTER 1: INTRODUCTION

Vegetation exerts a fundamental control on river morphodynamics (Corenblit et al., 2007; Gurnell, 2014) through mechanical and hydrological processes acting on the streambank (Abernethy and Rutherford, 2000: Pollen-Bankhead and Simon, 2010), and these processes can contribute to or detract from bank stability depending on local and regional factors such as vegetation type, bank materials, flow regime, and climate. In the arid and semi-arid Southwestern (SW), river regulation and drought have amplified the expansion of non-native, invasive riparian vegetation (IRV) and contributed to channel narrowing and simplification (Dean & Schmidt, 2013; Scott et al., 2018; Cadol et al., 2011; Vincent et al., 2009; Keller et al., 2014). IRV has been targeted for treatment in the SW as a part of environmental restoration since the 1960s (González et al., 2015; Shafroth et al., 2005), with treatment efforts increasing exponentially since 1990 (Bernhardt et al., 2005). Treatment of the dominant invasive vegetation can decrease hydraulic roughness and bank stability, at least temporarily, and can lead to channel widening and increased rate of channel migration (Jaeger & Wohl, 2011; Keller et al., 2014; Vincent et al., 2009). It is unknown, however, whether this is a frequent, widespread, and long-term response. While IRV treatment within river corridors has continued to increase along with overall channel restoration efforts, the post-IRV treatment monitoring has not kept pace (Rubin et al., 2017). Furthermore, numerical modeling studies on the hydraulic and geomorphic effects of IRV treatment are lacking (Gilbert and Wilcox, 2021; Eckermann et al., 2022). To address this knowledge gap, I conducted a multiscale analysis starting at the individual plant scale and ending at the regional scale to fully capture how vegetation interacts with and influences hydraulics and sediment transport, and thus channel morphology. There is abundant literature on the hydraulic

effects of individual plants and there are hydraulic models capable of incorporating vegetation roughness at the reach scale, but connecting these scales requires approaches that capture the spacing between plants and the distribution of plants on the floodplain. In this study, I bridged this gap by combining plant and plot data to estimate roughness for floodplain patches. Then, I incorporated spatially and depth-varied vegetation roughness into a two-dimensional hydraulic model of a river reach, and also modeled the removal of invasive vegetation to determine the effects on channel hydraulics. This work was focused on the Rio Grande in Boquillas Canyon in Big Bend National Park (BIBE), where the proliferation of invasive giant cane prompted a decade-long treatment and monitoring program (Briggs et al., 2021). The model domain included detailed topographic and field-based data on riparian plant traits that describe plant flexibility and influence flow and sediment transport. Field-data were collected at plant, plot, and reach scales. Modeling flexible vegetation is complex, and many studies (e.g. Musleh and Cruise, 2006; Kim et al., 2015; Bywater-Reyes et al., 2018) assume vegetation is rigid to avoid calculating pronated frontal areas at various flow depths. However, accurate descriptions of plant geometry and flexibility at a variety of spatial scales are essential to understanding the biogeomorphic interactions that influence channel hydraulics and ultimately drive channel morphologic change. Then, at the regional scale, I quantified channel response to IRV treatment in a study comparing treated and untreated reaches of rivers across the SW (Wieting et al., 2023).

In addition to vegetation, lithology and surficial soil properties control gully and channel morphology by influencing hydrological processes including infiltration, overland flow, and runoff. At Wupatki National Monument (WUPA) located in northern Arizona, lithological differences between volcanic cinders and underlying sedimentary rocks, and surface runoff processes influence the progression of channelized gullies at or near archaeological sites

(Wieting et al., 2024). Heavy sporadic rainstorms in the past decade, lack of vegetation, and presence of unconsolidated volcanic-derived cinders expose archaeological sites to erosion. These landscape and climate conditions offer unique challenges for cultural resource managers at the National Park Service (NPS), who seek to protect and preserve the archaeological record at WUPA.

This dissertation focuses on three main objectives as follows: 1) investigating the invasive vegetation directly to quantify the influence of specific plant species on channel hydraulics, 2) further quantifying channel response following invasive vegetation treatment, and 3) identifying landscape processes affecting archaeological sites. Chapters 2 and 3 focus on the interactions between channel morphology and vegetation presence and treatment at different spatial and temporal scales. In Chapter 2, I quantified plant-traits of common riparian plants found in the SW and evaluated how plant-trait differences between select invasive and native plants influence channel morphodynamics. I used abundant field data to quantify depth-varied vegetation roughness for individual plants and vegetation plots and applied the roughness data to a two-dimensional reach-scale hydraulic model. Six modeling scenarios were performed where different vegetation configurations and their associated roughness were assigned to field-mapped vegetation polygons. In Chapter 3, I used aerial imagery to investigate channel morphologic change over time following invasive plant treatment on a regional scale. I focused the analysis on mechanical and chemical methods of IRV treatment, and three dominant introduced floodplain plant species found in the SW: tamarisk (*Tamarix* spp.), Russian olive (*Elaeagnus angustifolia*), and giant cane (*Arundo donax*). I tested the hypothesis that IRV treatment increases streambank erosion and channel mobility by comparing channel metrics such as channel width and migration before and after removal in a paired design of treated and untreated reaches. I aimed to quantify

the response of river channels to IRV treatment and determine the influence of flood magnitude on the response to IRV treatment.

In Chapter 4, I collected baseline geomorphological data to analyze the hydrologic and erosional processes influencing the integrity of archaeological resources at WUPA to assist resource managers preserve archaeological sites. I analyzed lithological differences between volcanic cinders and underlying sedimentary rocks, assessed channelized gullies based on changes in gully morphology, and categorized archaeological sites based on vulnerability to erosion and runoff processes. Chapter 5 concludes with a summary of the findings presented in Chapters 2 through 4 and provides future research recommendations.

References

Bernhardt, E. S., Palmer, M. A., Allan, J. D., Alexander, G., Barnas, K., Brooks, S., … Sudduth, O. (2005). Synthesizing U.S. river restoration efforts. *Science*, *308*(5722), 636–637. https://doi.org/10.1126/science.1109769

Briggs, M. K., Poulos, H. M., Renfrow, J., Ochoa-Espinoza, J., Larson, D., Manning, P., … Crawford, K. (2021). *Choked out: Battling invasive giant cane along the Rio Grande/ Bravo Borderlands*. https://doi.org/10.1002/rra.3858

Cadol, D., Rathburn, S. L., & Cooper, D. J. (2011). *Aerial Photographic Analysis of Channel Narrowing and Vegetation Expansion in Canyon de Chelly National Monument, Arizona, USA, 1935-2004*. 1935–2004. https://doi.org/10.1002/rra.1399

Castro, J. M., & Thorne, C. R. (2019). The stream evolution triangle: Integrating geology, hydrology, and biology. *River Research and Applications*, *35*(4), 315–326. https://doi.org/10.1002/rra.3421

Dean, David J., & Schmidt, J. C. (2013). The geomorphic effectiveness of a large flood on the Rio Grande in the Big Bend region: Insights on geomorphic controls and post-flood geomorphic response. *Geomorphology*, *201*, 183–198. https://doi.org/10.1016/j.geomorph.2013.06.020

Gilbert, J. T., & Wilcox, A. C. (2021). An Biogeomorphic Framework Coupling Sediment Modeling With Invasive Riparian Vegetation Dynamics. *Journal of Geophysical Research: Earth Surface*, *126*(6). https://doi.org/10.1029/2021JF006071

González, E., Sher, A. A., Tabacchi, E., Masip, A., & Poulin, M. (2015). Restoration of riparian

vegetation: a global review of implementation and evaluation approaches in the international, peer-reviewed literature. Journal of Environmental Management, 158, 85-94.

Jaeger, K. L., & Wohl, E. (2011). Channel response in a semiarid stream to treatment of tamarisk and Russian olive. *Water Resources Research*, *47*(2). https://doi.org/10.1029/2009WR008741

Keller, D. L., Laub, B. G., Birdsey, P., & Dean, D. J. (2014). Effects of flooding and tamarisk treatment on habitat for sensitive fish species in the San Rafael River, Utah: Implications for fish habitat enhancement and future restoration efforts. *Environmental Management*, *54*(3), 465–478. https://doi.org/10.1007/s00267-014-0318-7

Ritter, D.F., Kochel, R.C., Miller, J.R. (2011). Process Geomorphology, Fifth Edition. Long Grove, IL: Waveland Press, Inc.

Rubin, Z., Kondolf, G. M., & Rios-Touma, B. (2017). Evaluating stream restoration projects: What do I learn from monitoring? *Water (Switzerland)*, Vol. 9. https://doi.org/10.3390/w9030174

Scott, M. L., Reynolds, L. V., Shafroth, P. B., & Spence, J. R. (2018). The role of a non-native tree in riparian vegetation expansion and channel narrowing along a dryland river. *Ecohydrology*, *11*(7), 1–17. https://doi.org/10.1002/eco.1988

Shafroth, P. B., Cleverly, J. R., Dudley, T. L., Taylor, J. P., Van Riper, C., Weeks, E. P., & Stuart, J. N. (2005). Control of Tamarix in the western United States: Implications for water salvage, wildlife use, and riparian restoration. *Environmental Management*, *35*(3), 231–246.

Vincent, K. R., Friedman, J. M., & Griffin, E. R. (2009). Erosional consequence of saltcedar control. *Environmental Management*, *44*(2), 218–227. https://doi.org/10.1007/s00267-009-9314-8

CHAPTER 2: A MULTISCALE ANALYSIS OF VEGETATION INFLUENCES ON CHANNEL HYDRAULICS ALONG THE RIO GRANDE IN BIG BEND NATIONAL PARK[1]

2.1 Introduction

Invasive non-native riparian vegetation has altered stream channel morphologies along rivers across the American Southwest (Manners et al., 2014; Bywater-Reyes et al., 2017; Scott et al., 2018; Wieting et al., 2023). Changes to a river's natural flow regime due to flow regulation and climate change (Mcshane et al., 2015; Blythe & Schmidt, 2018) have allowed colonization of invasive riparian vegetation (IRV), contributing to channel narrowing (Graf, 1978; Dean & Schmidt, 2011; Manners et al., 2014; Scott et al., 2018). Treatment of IRV has thus become an increasingly common restoration practice to restore riparian habitat, increase channel conveyance, and promote channel widening (Shafroth et al., 2005; Vincent et al., 2009; Shafroth et al., 2013). Depending on the restoration goal, the post-restoration effects on conveyance and channel morphology may be limited, however, due to altered flow regimes and/or revegetation. Revegetation increases the stream power threshold needed to achieve change, as banks are once again stabilized by root systems increasing bank strength (Wieting et al., 2022). Methods to treat invasive species include biological, mechanical, chemical, grazing, burning, flooding, and integrated control methods (Shafroth et al., 2010). IRV treatment monitoring efforts focus on vegetation (Harms & Hiebert, 2006; González et al., 2017a, 2017b) or wildlife (Sogge et al., 2008; Valente et al., 2019) response, but geomorphic processes are important drivers of riparian ecosystem dynamics and hence response to IRV treatment (Stromberg et al., 2007). Furthermore,

[1]Manuscript in preparation for *Journal of Geophysical Research: Earth Surface*.

flow regulation constrains vegetation-sedimentation feedbacks focusing research on the geomorphic drivers of morphologic change (Butterfield et al., 2020). The effectiveness of IRV treatments on stream channel change has been evaluated using field measurements (González et al., 2017; Jaeger & Wohl, 2011), aerial imagery (Keller et al., 2014; Gilbert & Wilcox, 2021; Wieting et al., 2023), various modeling approaches including hydraulic (Eckermann et al., 2022), bank stability (Pollen-Bankhead et al., 2009), sediment transport (Gilbert & Wilcox, 2021), and DEM differencing (Perignon et al., 2013; Gilbert & Wilcox, 2021). Using field measurements (Jaeger and Wohl, 2011) and bank stability modeling (Pollen-Bankhead et al., 2009), channel widening was observed along Chinle Creek in Canyon de Chelly National Monument, Arizona following treatment of invasive Tamarisk (*Tamarix ramosissima*) and Russian-olive (*Elaeagnus angustifolia*), but it was determined that large floods would be needed to shift the current incised channel morphology back to its former braided nature (Cadol et al., 2011). Using historical aerial imagery, Wieting et al., (2023) investigated channel change due to IRV treatment on 13 rivers across the Southwest U.S. Results of that study indicated treatment significantly increased channel width and floodplain destruction. Numerical modeling studies have assessed the effects of vegetation on hydraulics and channel change in field settings using patch (Manners et al., 2013; Diehl et al., 2018) and reach-scale models (Griffin et al., 2005; Manners et al., 2013; Bywater-Reyes et al., 2017, 2018; Diehl et al., 2018), but limited modeling studies exist on the hydraulic and geomorphic effects of IRV treatment (Gilbert & Wilcox, 2021; Eckermann et al., 2022), To address this knowledge gap, I numerically modeled the effect of IRV removal on flow hydraulics along the Rio Grande in Boquillas Canyon in Big Bend National Park (BIBE), where the proliferation of invasive giant cane prompted a decade-long treatment and monitoring program (Briggs et al., 2021).

2.1.1 Previous Research on the Relationships Between Vegetation and Flow Hydraulics

Quantifying changes in hydraulic roughness from various types of riparian vegetation in field settings and numerical simulations is critical to understanding process drivers of river form (Manners et al., 2013), and for shaping management strategies for natural biogeomorphic functions (Manners et al., 2013; Perignon et al., 2013; Bywater-Reyes et al., 2017; Diehl et al., 2018a; Butterfield et al., 2020). Vegetation has a dynamic effect on flow that depends on vegetation structure. Plant traits such as plant frontal area, flexural rigidity, and architecture affect the flow of water, transport of sediment, and stabilization of landforms (Diehl et al., 2017). Numerous experiments have measured flow resistance of real and artificial plants (Järvelä, 2002; Luhar & Nepf, 2011, 2013; Vargas-Luna et al., 2015; Lightbody et al., 2019; Zhang & Nepf, 2020), yet it is still not possible to accurately predict the effects on flow for a variety of riparian plant species (Vargas-Luna et al., 2015). Bywater-Reyes et al. (2017) modeled rigid cottonwood (*Populus trichocarpa*) on a point bar to predict how channel-bend hydraulics are influenced by sparse or dense cottonwood configurations. They found that compared to a no-vegetation scenario, vegetation reduced flow velocities and contributed to flow steering, resulting in increased bar accretion and erosion of the opposing cutbank. Diehl et al. (2018) used an edited FaSTMECH solver within iRIC (Nelson et al., 2016) that accounted for flexible vegetation behavior during floods to build a model of riparian ecosystem dynamics. The edited hydraulic model uses depth-dependent varied roughness based on changing plant frontal areas as flow depth changes. Frontal area and other geomorphic-effect plant traits were measured to group riparian plants into a suite of morphological guilds (Diehl et al., 2017), develop flow response curves to assess ecosystem response to changes in streamflow, and predict areas of erosion and deposition along the Green River in Utah (Diehl et al., 2018a). Butterfield et al. (2020) used

generalized additive models (GAMs) and linear mixed-effect models (LMEs) to link topographic changes over time to morphological guilds established from Diehl et al. (2018) within different geomorphic settings and hydrological zones along the Colorado River in Grand Canyon. Their study included similar plant species as those found within the riparian corridor of BIBE including but not limited to phragmites, baccharis, willow, and tamarisk. In general, higher sedimentation rates were positively associated with the presence of vegetation, but guild associations with topographic change depended on hydrological zone and geomorphic setting within an eddy-sandbar complex (Butterfield et al., 2020).

Given the numerous methods for calculating vegetation roughness, several studies have performed comparisons within hydraulic modeling analyses (Abu-Aly et al., 2014; Wang et al., 2019; Chaulagain et al., 2022). Abu-Aly et al. (2014) used LiDAR-derived vegetation canopy height data to create a 2D hydraulic model with spatially varied roughness, but the authors did not consider plant flexibility and streamlining. Vegetation was found to have a strong channelization effect, and significant differences existed between the spatially distributed and constant roughness schemes, especially above bankfull discharge (Abu-Aly et al., 2014). Wang et al. (2019) and Chaulagain et al. (2022) both analyzed the influence of riparian vegetation on the San Joaquin River in California using field and flume-based data. Wang et al. (2019) used the one-dimensional Hydrologic Engineering Center-River Analysis System (HEC-RAS) to predict river stages due to dense riparian vegetation and includes giant cane in their study. The authors found that the Whittaker et al. (2015) method which uses detailed frontal area data and includes the reconfiguration of flexible plants provided better results than other methods in the study (Wang et al., 2019). Chaulagain et al. (2022) used a vegetation model within the Sedimentation and River Hydraulics-Two-Dimensional model (SRH-2DV) to compare the influence of

vegetation roughness computation methods on flow depth and velocity. Giant cane was mentioned in the Chaulagain et al. (2022) study but does not appear to be considered in the hydraulic model. The authors compared the Baptist et al. (2007) and Järvelä (2004) methods, which respectively use stem density and leaf area index (LAI) as proxies for frontal area and found that the Järvelä approach was better suited for high-density, leafy vegetation and the Baptist approach for low vegetation density (Chaulagain et al., 2022). Ultimately, vegetation roughness is difficult to incorporate into hydraulic modeling, but these studies provided insight into how the complexities and spatial variation of vegetation complicates floodplain hydraulics.

Other noteworthy studies that investigate channel-vegetation interactions specific to invasive giant cane include Gilbert and Wilcox (2021), Spencer et al. (2013), Stover et al. (2018), and Lama et al. (2021). Gilbert and Wilcox (2021) modeled the spread of giant cane (and sediment) in the Santa Clara River watershed of Southern California and assessed how floods redistribute vegetation. Giant cane rhizomes that are transported downstream during high flows rapidly take root and can establish in a variety of soil conditions (Lambert et al., 2014; Gilbert and Wilcox, 2021). Gilbert and Wilcox (2021) coupled sediment and vegetation models and identified giant cane sources and sinks based on sediment supply, floodplain erosion or deposition, and giant cane recruitment. Their study results identify giant cane sources by modeling sediment and vegetation distributions as the invasive plant propagates downstream. Their results provide critical information for restoration and management actions by allowing practitioners to prioritize giant cane removal areas in the upstream portions of watersheds that would mobilize under certain flow conditions. Considering that giant cane readily reproduces and transports downstream, bank erosion is an important component in understanding how this riparian species interacts with fluvial processes and possibly facilitates channel change (Gilbert

and Wilcox, 2021). While giant cane stands are eroded during large, infrequent floods, it is not known what velocities or shear stresses can be resisted by the stands. It appears that floods remove the plants and undercut the roots, and in some situations only the above-ground vegetation is mobilized (Giessow et al., 2011). To gain insight into giant cane's root architecture and strength, Stover et al. (2018) evaluated differences between root distribution and root tensile strength for giant cane and a native willow plant (*Salix laevigata*) on the Santa Clara River. Their findings indicated that giant cane had significantly more large roots near the surface of the streambank, with fewer roots at depth, increasing the likelihood of bank erosional processes such as undercutting, slumping, and cantilever bank failure. Lama et al. (2021) used field measurements and an unmanned aerial vehicle (UAV) to compare observed and estimated values of bulk drag coefficients of giant cane stands through measurements of leaf area index (LAI). UAV-derived and ground-based values of bulk drag coefficient were comparable, demonstrating the strong capabilities of the UAV approach for evaluating impacts of riparian vegetation.

2.1.2 Previous Rio Grande Research in BIBE

Studies along the Rio Grande in the Big Bend region have analyzed changes in the natural flow regime (Blythe & Schmidt, 2018), mechanisms of channel narrowing (Dean & Schmidt, 2010; Dean et al., 2011), and the geomorphic effects of different types of floods (Dean & Schmidt, 2013; Dean et al., 2016). These studies suggest a shift in the channel morphology of the Rio Grande from a wide multi-thread river to a single-thread channel due to decreased channel capacity, increased sediment aggradation, and a lack of channel "reset" floods (Dean & Schmidt, 2011; Blythe & Schmidt, 2018). The most recent reset flood occurred in 2008, with a magnitude of 1490 m^3/s (Dean & Schmidt, 2013). Post-reset flood analyses indicate channel widening, channel avulsions, bar formation, and vertical floodplain accretion (Dean & Schmidt, 2013). During

tributary-sourced flash floods, abundant sediment trapping occurs by both native and non-native plants, facilitating channel narrowing through vertical accretion on channel bars and the formation of inset floodplains (Dean et al., 2016). Alluvial reaches throughout BIBE allow for more lateral spreading of water and sediment and attenuate floods more readily. Canyon reaches such as Boquillas Canyon are confined by bedrock and densely vegetated banks but contain a mixture of actively reworked (lower geomorphic surfaces) and infrequently inundated (higher geomorphic surfaces) alluvial deposits (Blythe, 2018). These deposits host biologically diverse riparian plant communities and are crucial to providing diverse habitats. However, the spread of invasive giant cane simplified these once diverse regions which led to an extensive treatment and monitoring program. Briggs et al. (2021) used repeat vegetation plot data and statistical analyses to determine the effectiveness of treatments and riparian plant community response. Over 10 years, giant cane cover declined significantly following treatment, allowing native plants (*Salix exigua and Baccharis salicifolia*) to reestablish (Briggs et al., 2021).

2.1.3 Research Questions and Hypotheses

The influence of vegetation on channel hydraulics and morphodynamics is widely variable based on the scale, spatial pattern, and stem density of individual plants and vegetation patches (Follet and Nepf, 2012; Luhar and Nepf, 2013; Manners et al., 2013; Yager and Schmeekle, 2013; Bywater-Reyes et al., 2018). Numerical models and flume studies evaluate vegetation's influence on hydraulics and morphodynamics at smaller spatial scales under specific vegetation, flow, and sediment conditions (e.g. Järvelä, 2002; Ortiz et al., 2013; Manners et al., 2015). River reach and corridor studies capture broader trends of biogeomorphic feedbacks but may lack specific details about the influence of plant architecture, density, or spacing of plants (e.g. Tooth and Nanson, 2000). At the individual plant scale, plant size generally influences flow and

sediment transport, while the density and spacing of plants becomes more important at the patch scale (Luhar and Nepf, 2013; Diehl et al., 2017). At the reach scale, the distribution and abundance of vegetation patches may play a more critical role in influencing hydraulics and morphodynamics. Linking vegetation-morphodynamic relationships from smaller to larger spatial scales captures pertinent small-scale drivers of erosion and deposition as well as more complex biogeomorphic-system interactions at larger scales. These linkages are crucial to understanding the cumulative impacts of vegetation on channel and floodplain form (Bywater-Reyes et al., 2022). Along the Rio Grande in BIBE, vegetation grows as isolated plants (e.g. baccharis) and in patches/stands on the channel banks. To address the complex distribution of vegetation and analyze vegetation's influence on hydraulics at the reach scale, I conducted a multiscale analysis and extrapolated field-based morphological-effect trait data at the plant and plot scales to vegetation mapped at the reach scale in the field. To address research gaps, I pose the following research questions: (1) Do non-native giant cane and native phragmites and baccharis cause different geomorphic responses to flooding? And (2) are water and sediment conveyance improved through the ongoing giant cane management program? I hypothesize that complex interactions between plant frontal area and hydraulic roughness exist such that (H1a) the greater upright frontal area of invasive giant cane creates a higher, nonlinear increase in hydraulic roughness than native vegetation (Figure 2.1a), but; (H1b) At higher flow depths, the greater flexibility of giant cane decreases hydraulic roughness (Figure 2.1b). Based on existing literature, I also hypothesize that (H2) removing giant cane reduces hydraulic roughness, increasing flow velocities and shear stress, and decreasing sediment deposition.

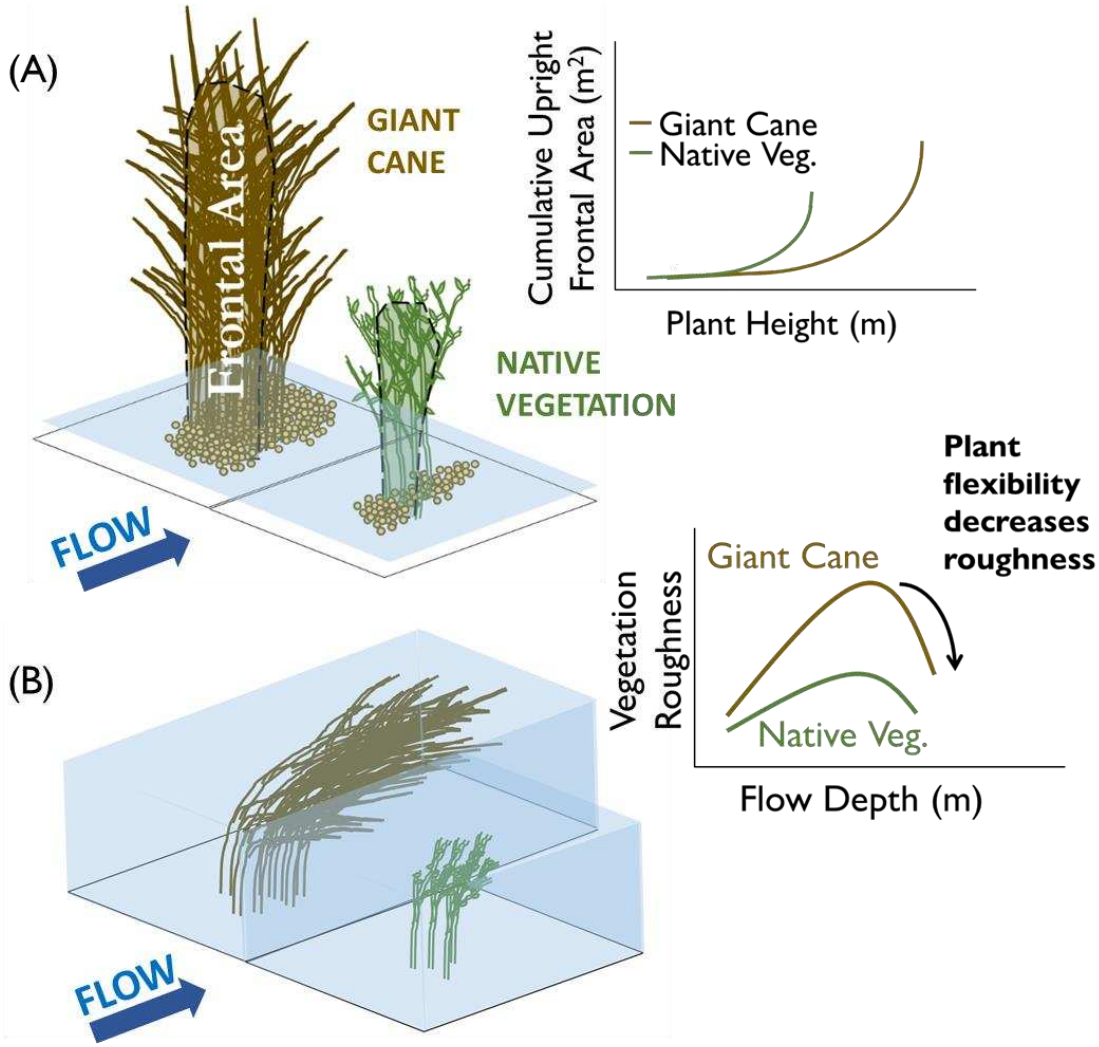

Figure 2.1. Conceptual diagrams illustrate (A) plant/plot height versus cumulative upright frontal area for non-native giant cane and native phragmites and baccharis. The additional drag caused by plants is proportional to frontal area, and the cumulative upright frontal area and plant height is higher for giant cane compared to native phragmites and baccharis. Considering the higher drag from giant cane, (B) vegetation roughness of giant cane is higher. As flexible plants become inundated, frontal area decreases and vegetation roughness also decreases.

2.1.4 Study Area

The Rio Grande serves as the border between U.S. and Mexico and alternates between wide alluvial reaches and confined narrower canyons, including Boquillas Canyon. The river through BIBE is subject to geomorphic changes due primarily to upstream flow regulation from

large dams and diversions which reduce flow magnitude and sediment transport capacity. Vegetation has colonized geomorphic surfaces adjacent to the channel causing sediment deposition and exacerbating channel narrowing by stabilizing stream bank sediments and increasing hydraulic roughness (Jaeger & Wohl, 2011; Dean & Schmidt, 2011, 2013; Scott et al., 2018). To analyze interactions between vegetation and channel hydraulics and morphology, I selected 6 study sites located within Boquillas Canyon at monumented sand bars that have been previously studied by the U.S. Geological Survey (USGS) and National Park Service (NPS). Boquillas Canyon is approximately 50 km long and the U.S. portion is located within BIBE (Figure 2.1). Floodplain and alluvial banks are densely vegetated with nonnative giant cane, native willow (*Salix* spp.), native baccharis (*Baccharis salicifolia*), and native phragmites (*Phragmites australis*), among other species (Dean et al., 2016). Giant cane is a perennial reed grass that tends to form dense monotypic stands and large clumps with continuous, clonal root masses (Bell, 1997). The grass outcompetes native vegetation, and while flooding may be beneficial for riparian ecosystems, giant cane is disturbance-driven and spreads easily downstream. Giant cane has colonized and negatively impacted riparian corridors of Southern California and along the Rio Grande in Texas and Mexico (Lambert et al., 2010). Phragmites is also a tall perennial grass that spreads through seeds and rhizome fragments (Lambert et al., 2010). In BIBE, phragmites is considered native, but it is classified as a noxious weed in six U.S. states and others are reclassifying its status (Lambert et al., 2010). A vegetation control program in BIBE has been developed to eradicate non-native tamarisk and giant cane to improve habitat and increase water and sediment conveyance through the Rio Grande. Beginning in 2003, the National Park Service (NPS) first began efforts to eradicate non-native tamarisk using mechanical and biological control methods (releasing the *Diorhabda* beetle). Tamarisk was

essentially eradicated, initiating more recent efforts focused on the control of non-native giant cane. A combination of fire, herbicide, and biological control methods (releasing the giant cane wasp, *Tetramesa romana*) have helped eradicate much of the giant cane, but large homogenous stands remain, and effects of removal are poorly documented or understood. In some areas where giant cane has been eradicated, bank collapse has resulted in wider and more desirable channel conditions (Briggs et al., 2021).

The Rio Conchos is the largest tributary to the Rio Grande, providing approximately 90% of its streamflow (Dean & Schmidt, 2013; Blythe & Schmidt, 2018) and high suspended-sediment concentrations during high flows (Dean et al., 2015). The second largest tributary is the Pecos River. The Rio Grande upstream of the Rio Conchos is driven by snowmelt, but snowmelt runoff is nearly entirely diverted for agricultural purposes above the confluence with the Rio Conchos (Blythe & Schmidt, 2018). Large dams and diversions on both the upper Rio Grande in New Mexico, and on the Rio Conchos in Mexico have caused reductions in peak flow and flood magnitude, allowing vegetation to colonize on infrequently inundated surfaces. Many of the largest recent floods have been sourced in ephemeral tributaries in the summer and fall. These tributaries provide important flow and sediment contributions to the Rio Grande.

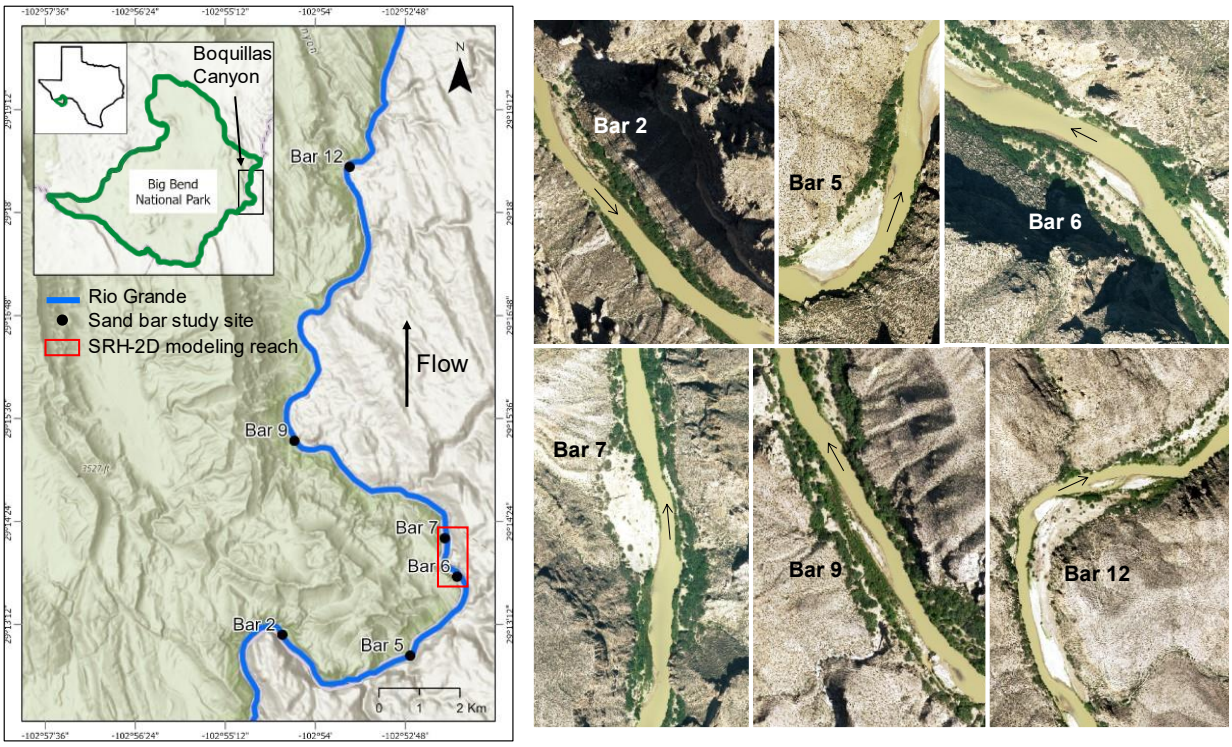

Figure 2.2. Location map of Boquillas Canyon study area along the Rio Grande and Texas-Mexico border. Sand bar locations correspond to monumented study sites. The red box outlines the study reach used within the flood surface-vegetation analysis and hydraulic model.

2.2 Methods

2.2.1 Field Data Collection

To analyze the effects of different plant species on channel hydraulics and morphology, I collected data at six monumented sand bars (Figure 2.2) for native and invasive plant species in October 2021. I focused field data collection efforts on plant morphological-effect traits (Diehl et al., 2017) and gathered essential parameters required for hydraulic modeling. Data were collected based on a multiscale analysis: at the plant, plot, and reach scale. At the plant and plot scale, data were collected to quantify upright and flexible frontal areas, and depth-varied vegetation roughness. At the reach scale, I mapped vegetation patches to link species distribution to geomorphic surfaces. Polygons of vegetation were drawn in the field using 2019 NAIP imagery

and then later edited in ArcGIS Pro. The distribution of vegetation on different geomorphic surfaces is herein referred to as the "reach scale" of analysis.

I used an iPhone 12 to take photographs of individual plants against a solid red background in the downstream direction to quantify upright frontal area (Lightbody and Nepf, 2006; Straatsma et al., 2008; Whittaker et al., 2015; Diehl et al., 2017). Diehl et al. (2017) found that a red background provided the greatest contrast with the foliage and stems for most plants. Photographs were then edited using GNU Image Manipulation Program (GIMP) to identify and separate plant material from the background (Figure 2.3). I created iterative and cumulative vertical upright area curves for each plant type based on the number of plant pixels using the edited plant photographs. Due to the nature of stems of phragmites and giant cane, I considered one "plant" to be one stem, starting at the ground surface; below-ground connections were not examined. Upright frontal area was normalized by the individual plant's canopy area to compare frontal area between species.

I conducted stem counts within varied sized plots (generally plots were 1 m^2) at the ground level and near breast height to quantify upright frontal area of vegetation plots. For plots with plants shorter than breast height, stem counts were performed at approximately half the total average plot height. Counted stems were grouped into five size classes of 0–0.5 cm, 0.5–1 cm, 1–2 cm, 2–4 cm, and greater than 4 cm. Using the stem count data, I calculated the total diameter sum within each plot at each sampled height (Equation 3.1).

$$D = \sum_{i=1}^{5} M_i * \mathrm{N}_i \qquad \text{(Eq. 2.1)}$$

Where M_i is the midpoint of size class *i* and N_i is the number of stems in size class *i*. The midpoints of the size classes used were 0.25, 0.75, 1.5, 3, and 4 cm. The representative total plot height was measured in the field, and at this height, the total average diameter sum was equal to zero. I

interpolated between the two measured heights and the total plot height, and integrated beneath this curve to incrementally calculate the plot's upright frontal area:

$$A_{f_{plot}} = \int_{0.01}^{h_{up}} D \, dh_{inc} \quad \text{(Eq. 2.2)}$$

Where h_{up} is the height of the upright plot, dh_{inc} is the incremental height within a plot. The total upright plot frontal area was held constant at flow depths greater than the plot height. Similar to individual plants, upright frontal area for plots was normalized by plot area to more accurately compare frontal area between species.

Figure 2.3. Examples of edited photos to use within ELA for quantifying upright plant frontal area. Images are of giant cane (left) and baccharis (right).

I measured force-displacement relationships in the field to calculate plant flexural rigidity using force calipers attached to the plant's dominant stem to measure the horizontal distance the plant was displaced. A minimum of three measurements were recorded for each force-displacement, at various heights up the dominant stem, generally a quarter and halfway up the total

plant height. A total of 237 measurements were made on 35 individual plants. Following Usherwood et al. (2017), I calculated flexural rigidity ($N * m^2$):

$$EI = \frac{P^3 \frac{dF}{d\delta}}{48} \quad \text{(Eq. 2.3)}$$

where P is the height of the stem for which the force-displacement measurement was made and $\frac{dF}{d\delta}$ is the relationship between the change in applied force (F), and the displacement (δ). Force-displacement measurements were averaged at each measured height, and then an average was used between all measured heights.

Figure 2.4. Measuring the force-displacement relationship for a baccharis plant to calculate flexural rigidity.

For both woody and herbaceous plants, I collected a 10 cm long sample of the plant stem near the ground surface (Perez-Harguindeguy et al., 2013). Samples were kept moist until

processed in the lab. In the lab, wet samples were weighed and measured to determine stem mass and volume to quantify stem tissue density. I used the Kruskal-Wallis non-parametric analysis of variance (ANOVA) at a 95% confidence level to test for significant differences in stem tissue density, as well as flexural rigidity and frontal area between species for individual plants.

2.2.2 Field Data Analysis

2.2.2.1 Calculation of depth-varied vegetation roughness for flexible plants

Plant reconfiguration is a function of two opposing forces: the hydrodynamic drag that pushes the plant over, and the restoring forces that keep the plant upright (Diehl et al., 2018). I solved for plant reconfiguration and developed relationships between plant/plot height and deflected frontal area using a physically based model following Luhar and Nepf (2011, 2013). The Cauchy number and buoyancy are dimensionless parameters that represent these opposing forces. The Cauchy number is the magnitude of the hydrodynamic drag and the restoring force due to stiffness:

$$Ca = \frac{\rho U^2 A_f h^2}{EI} \quad \text{(Eq. 2.4)}$$

where ρ is the density of water, U is the horizontal velocity, h is the upright plant/plot height that is underwater, EI is the flexural rigidity, and A_f is the upright area of the plant that is underwater (Luhar & Nepf, 2011; Whittaker et al., 2015; Diehl et al., 2018). Initial estimates of velocity were derived from Manning's equation (Equation 3.5) using an initial estimate of slope of 0.004 (approximate channel slope in Boquillas) and a roughness of 0.1. Velocity was computed incrementally at increasing flow depths every centimeter up to 10 meters.

$$U = \frac{1}{n} S^{\frac{1}{2}} H^{\frac{2}{3}} \quad \text{(Eq. 2.5)}$$

At the plot scale, I applied a scaling ratio to accommodate combining plant and plot datasets. The scaling ratio was needed because the Cauchy number equation is derived for individual plants, however I needed to parameterize the Cauchy number for plots. I used a ratio of a plant species' median total upright frontal area for individual plants ($\tilde{A}_{f_{Tot_{plant}}}$) to the total upright frontal area for a specific plot ($A_{f_{Tot_{plot}}}$). There were no flexural rigidity measurements performed on plots, so the median flexural rigidity from individual plants was used for plot scale calculations (Equation 3.6).

$$Ca = \frac{\rho U^2 A_{f_{plot}} h^2}{EI} * \left(\frac{\tilde{A}_{f_{Tot_{plant}}}}{A_{f_{Tot_{plot}}}}\right) \quad \text{(Eq. 2.6)}$$

Next, I calculated the buoyancy parameter for plants using Equation 3.7:

$$B = \frac{(\rho - \rho_v) g A_f b h_{up}^2}{EI} \quad \text{(Eq. 2.7)}$$

where ρ_v is the stem tissue density, g is the gravitational constant, b is the stem diameter, and h_{up} is the upright height of the plant (Diehl et al., 2018). At the plant scale, I used the average stem diameter from stem samples collected at each plant. At the plot scale, the average stem diameter from all stem count measurements for each plant species was used in addition to a scaling ratio similar to the Cauchy parameter:

$$B = \frac{(\rho - \rho_v) g A_{f_{plot}} b h_{up_{plot}}^2}{EI} * \left(\frac{\tilde{A}_{f_{Tot_{plant}}}}{A_{f_{Tot_{plot}}}}\right) \quad \text{(Eq. 2.8)}$$

where $h_{up_{plot}}^2$ is the total upright height of the plot. Following Whittaker et al. (2015) and to reduce error while calculating vegetation roughness, I assumed the buoyancy of plants and plots was negligible.

The Cauchy and buoyancy parameters were used to iteratively calculate deflected height (h_{def}) and effective height (h_e) with increasing depth (Luhar and Nepf, 2011; Luhar and Nepf, 2013; Diehl et al, 2018):

$$\frac{h_{def}}{h} = 1 - \frac{1 - Ca^{-1/4}}{1 + Ca^{-3/5}\left(4 + B^{3/5}\right) + Ca^{-2}(8 + B^2)} \quad \text{(Eq. 2.9)}$$

$$\frac{h_e}{h} = 1 - \frac{1 - 0.9Ca^{-1/3}}{1 + Ca^{-3/2}\left(8 + B^{3/2}\right)} \quad \text{(Eq. 2.10)}$$

These equations are derived from experiments using submerged plants, but I assumed these equations are applicable while our plants are emergent. Using the upright plant/plot frontal areas, Cauchy was incrementally calculated with increasing depth as the plant reconfigures. While the plant is emergent, the water depth was used as the plant height (Whittaker, 2015). I assumed the plant is submerged once h equals the total upright plant height (h_{up}) and used the total upright plant height to calculate Cauchy thereafter.

As a plant reconfigures, the frontal area is reduced, and the plant becomes more streamlined. The deflected height only captures the reduction in frontal area, while effective height considers both mechanisms of plant reconfiguration (Luhar and Nepf, 2011). For this reason, the effective height was used to calculate the effective frontal area and develop plant and plot height-effective frontal area relationships (A_{eff} and $A_{eff_{plot}}$):

$$A_{eff} = \left(\frac{h_e}{h}\right) * A_f \quad \text{(Eq. 2.11)}$$

$$A_{eff_{plot}} = \left(\frac{h_e}{h}\right) * A_{f_{plot}} \quad \text{(Eq. 2.12)}$$

At flow depths greater than the height of the plant/plot, I held the maximum upright plant and plot heights constant. Next, the reduction in bed shear stress due to vegetation (F_τ) was set equal to the vegetation form drag (F_D) to derive the equation for depth-varied vegetation roughness at the plant (n_v) and plot ($n_{v_{plot}}$) scales:

$$n_v = \sqrt{\left(\frac{A_{eff}}{A_c}\right)\frac{C_D H^{\frac{1}{3}}}{2g}} \quad \text{(Eq. 2.13)}$$

$$n_{v_{plot}} = \sqrt{\left(\frac{A_{eff_{plot}}}{A_{plot}}\right)\frac{C_D H^{\frac{1}{3}}}{2g}} \quad \text{(Eq. 2.14)}$$

where A_c is the canopy area of the plant, and A_{plot} is the plot area (e.g. Petryk and Bosmajian, 1975; Fathi-Maghadam and Kouwen, 1997; Järvelä, 2004; Musleh and Cruise, 2006; Manners et al., 2013; Bywater-Reyes et al., 2022; Derivation in Appendix A).

2.2.2.2 Vegetation on flood surfaces

I used ArcGIS Pro to analyze associations between plant species and geomorphic setting. Geomorphic units mapped by Blythe (2018) included the active channel (Osterkamp and Hedman, 1982) and three higher flood surfaces (Figure 2.5). The active channel was delineated by the break in slope between the maximum elevation of channel bars and higher fine-grained deposits, typically marked by a steep bank (Blythe, 2018). Defined in this way the active channel included some surfaces occupied by established woody vegetation. Reach-scale vegetation data mapped in the field in October 2021 were imported into ArcGIS Pro and edited using aerial imagery to refine the delineations of vegetation boundaries (Figure 2.5).

A water surface profile for a low discharge was created by kriging surveyed water's edge points from July 2018. During this month, discharge ranged from 2.8 m^3/s to 67 m^3/s. The water

surface profile was then subtracted from the 2018 DEM to detrend the elevation data. A workflow was built within ModelBuilder in ArcGIS Pro to utilize a series of geoprocessing tools (Figure 2.5). Geoprocessing tools that function with polygon and raster data were used to generate elevation point data where specific vegetation overlapped specific geomorphic units. The workflow was repeated for the different combinations of vegetation and geomorphic units. Using Matlab, I created histograms and fit distributions using the nonparametric kernel-smoothing distribution function to retain the most information from the data while smoothing. For the phragmites in the active channel dataset, the nonparametric smoother did not converge and so the gamma distribution was used instead. Statistical analyses including mean, median, standard deviation, and skewness of the point data were also calculated to evaluate plant distributions across geomorphic surfaces.

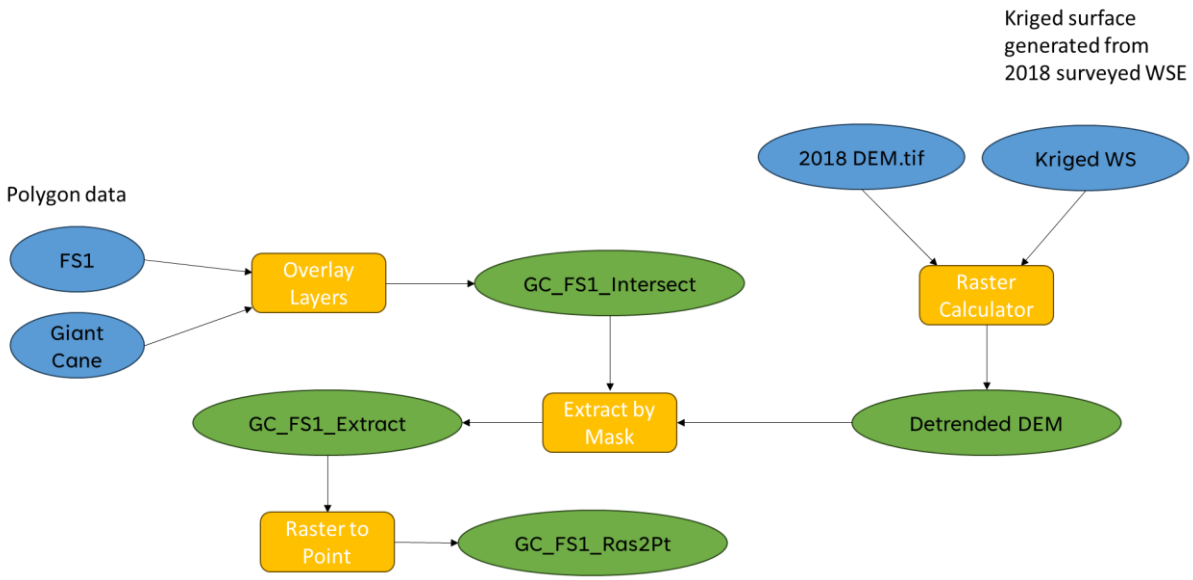

Figure 2.5. ArcGIS PRO model builder workflow to create overlapping geomorphic and vegetation point data.

I also calculated the inundating discharge for specific plant species based on the percent of active channel and flood surfaces inundated (Blythe, 2008) and the median elevation at which

plant species grow. Understanding the inundating discharge helps determine the conditions under which plants survive and allows for better management of riparian zones.

2.2.2.3 Hydraulic Modeling

I used the Sedimentation and River Hydraulics-Two-Dimensional (SRH-2D) model within the Surface-water Modeling System (SMS) version 13.3 software (Aquaveo, LLC, Provo, UT) to simulate hydraulic conditions for the Rio Grande through Boquillas Canyon. SRH-2D is a two-dimensional hydraulic and sediment transport model developed by the U.S. Bureau of Reclamation and uses a hybrid computational mesh using both quadrilateral and triangular elements (Lai, 2008). The SRH-2D model is widely used and accounts for depth-varied roughness of modeled materials. The model requires input parameters including an upstream river discharge boundary condition, a downstream boundary condition of either a constant water surface elevation (WSE) or stage-discharge rating curve, topographic data as the basis for the model grid, and Manning's roughness values from the channel bed and vegetation. Modeling flexible vegetation is complex, and many studies assume vegetation is rigid to avoid calculating pronated frontal areas at various flow depths. In this study, I used depth-varied Manning's roughness values to incorporate the flexible nature of plants as flow depth changes.

To test hypothesis 1, a two-dimensional reach-scale hydraulic model of the Rio Grande was built to evaluate the hydraulic effects of giant cane, phragmites, and baccharis separately. Then, to test hypothesis 2, I removed the giant cane polygons from the model to simulate the effects of giant cane removal (Figure 2.6). Giant cane, baccharis, and phragmites polygon areas made up 29%, 60%, and 11% of the vegetation in the model, respectively. Following a decade-long effort to manage giant cane, recent research has shown significant declines in giant cane cover post-treatment ($p<0.05$), and significant revegetation of native *Salix* spp. and baccharis ($p <0.05$) in

treatment areas within BIBE (Briggs et al., 2021). Therefore, I focus modeling efforts on a comparison of invasive (giant cane) and native (baccharis and phragmites) vegetation using reach-scale modeling scenarios (Table 2.1, Figure 2.6).

Table 2.1. Modeling scenarios outlining roughness and plant configurations, and corresponding inlet discharge.

Model Scenario #	Inlet discharge (m^3/s)
Calibration 1 – Bed roughness, no vegetation	18.5
Calibration 2[A] – Bed and vegetation roughness Realistic vegetation distribution	244[B]
1 – Bed roughness, No vegetation	100, 244, 500, 1000, 1490
2 – Bed and vegetation roughness All vegetation mapped as giant cane	100, 244, 500, 1000, 1490
3 – Bed and vegetation roughness All vegetation mapped as baccharis	100, 244, 500, 1000, 1490
4 – Bed and vegetation roughness All vegetation mapped as phragmites	100, 244, 500, 1000, 1490
5 – Bed and vegetation roughness Realistic vegetation distribution	100, 244, 500, 1000, 1490
6 – Bed and vegetation roughness Giant cane removed from realistic vegetation distribution	100, 244, 500, 1000, 1490

[A] Calibration 2 was performed to validate the calibrated bed roughness values from Calibration 1. First, the 244 m^3/s flow was simulated using only bed roughness. The model underestimated WSE compared to measured values. Next, vegetation roughness was added without the additive bed roughness in the overlapping regions using the realistic vegetation distribution. Once again, the model generally underestimated WSE. Finally, bed roughness was added to the vegetated regions.

[B] The 244 m^3/s flow was obtained from a calibrated FaSTMECH hydraulic model using known WSE (Blythe, 2018).

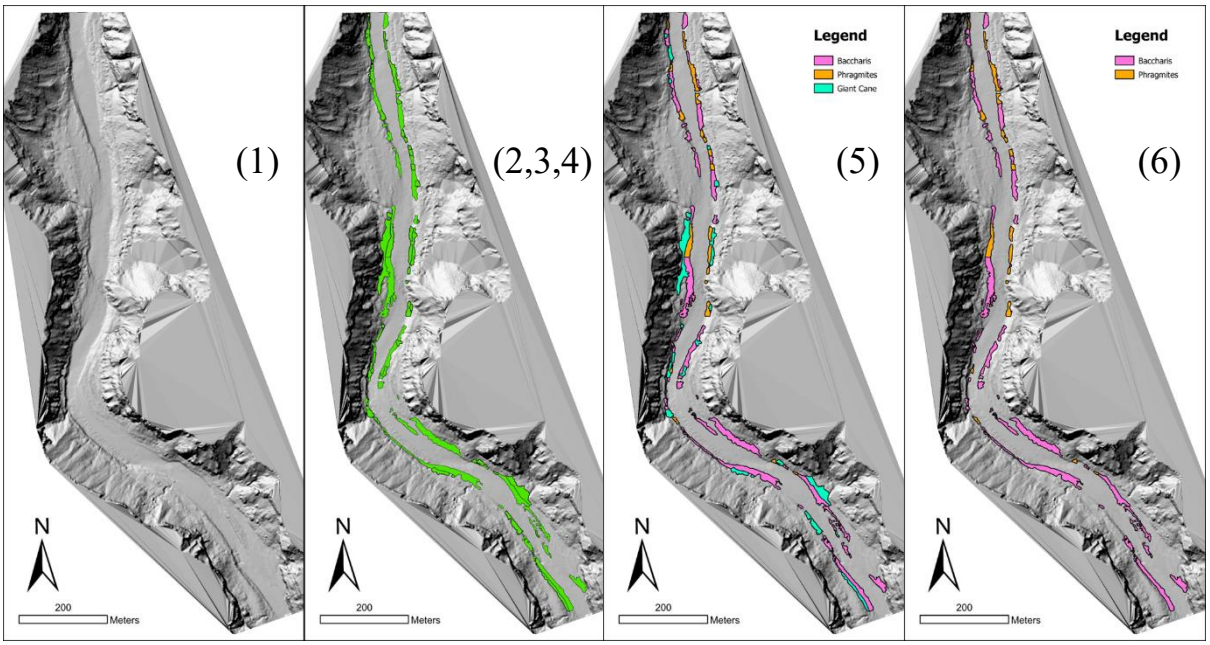

Figure 2.6. Modeling scenarios to quantify the influence of species-specific native and invasive vegetation, and the effect of invasive removal, on hydraulics. A no-vegetation scenario (1) was used to compare against vegetated scenarios (2-6). All vegetation polygons (shown in green) were mapped as giant cane in scenario 2, baccharis for scenario 3, and phragmites for scenario 4. A realistic distribution of giant cane, baccharis, and phragmites is represented in scenario 5. Lastly, giant cane is removed and native baccharis and phragmites remain in scenario 6.

The model mesh was built using the active channel polygon data. High-resolution topographic data collected from field surveying in 2017 was then applied to the mesh. Mesh resolution near the channel was 1 m and increased using cubic spline interpolation to 20 m at the outer model boundaries. Flood surfaces (e.g., FS1 and FS2) mapped from Blythe (2018) were used to determine the range of simulated flood magnitudes in Boquillas Canyon (Figure 2.7). I modeled a series of low and high flows for each FS1 and FS2 (Q_1 = 100 m^3/s, Q_2 = 244 m^3/s, Q_3 = 500 m^3/s, Q_4 = 1000 m^3/s) and the most recent modern "reset" flood (Q_5 = 1490 m^3/s,) to address the stage-dependent influence of native and invasive plants on hydraulics (Figure 2.1). A stage-discharge rating curve defined the downstream boundary condition (Figure 2.7; Blythe, 2018).

Baseline channel bed and floodplain bed roughness varied spatially based on sediment samples collected by Blythe (2018) and updated according to sediment samples collected in

October 2021 and an analysis of channel morphologic change since 2018 from aerial imagery. Bed roughness values were converted from Nikuradse (1950) z_0 to Manning's n using the Strickler Equation (CHOW, 1959):

$$n = Ck_s^{1/6} = C(30z_0)^{1/6} \quad \text{(Eq. 2.15)}$$

Where C was assumed to equal 0.034 for regions composed of predominantly sand (less than 2 mm), or 0.038 for regions coarser than sand (Chow, 1959). The term k_s is the effective roughness height and is correlated to the median grain size (D_{50}) of the bed sediment for fine-grained deposits, or the D_{84} for coarse-grained deposits. To simplify the 2D model and ensure computational performance, bed roughness polygons were grouped into four Manning's roughness values. The upland regions on either side of the channel were assigned a baseline floodplain roughness of 0.1 (Acrement & Schneider, 1989).

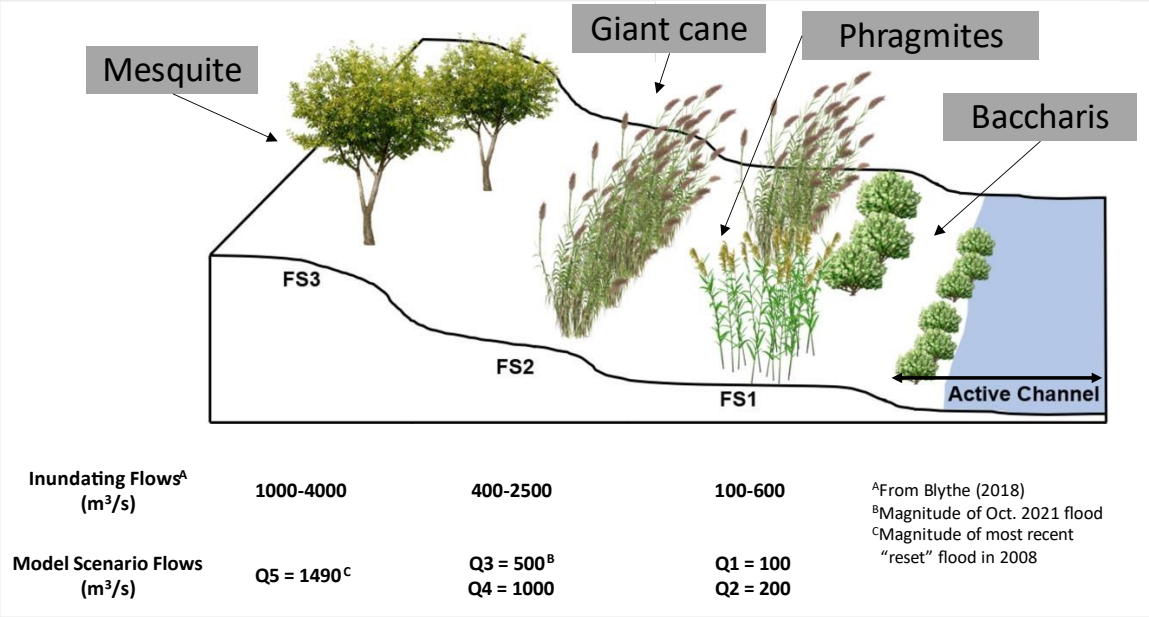

Figure 2.7. Generalized distribution of common riparian vegetation found in the study area on flood surfaces near the channel. Inundating flows for each flood surface, determined from Blythe (2018), were used to design model scenario flows (Q1-Q5).

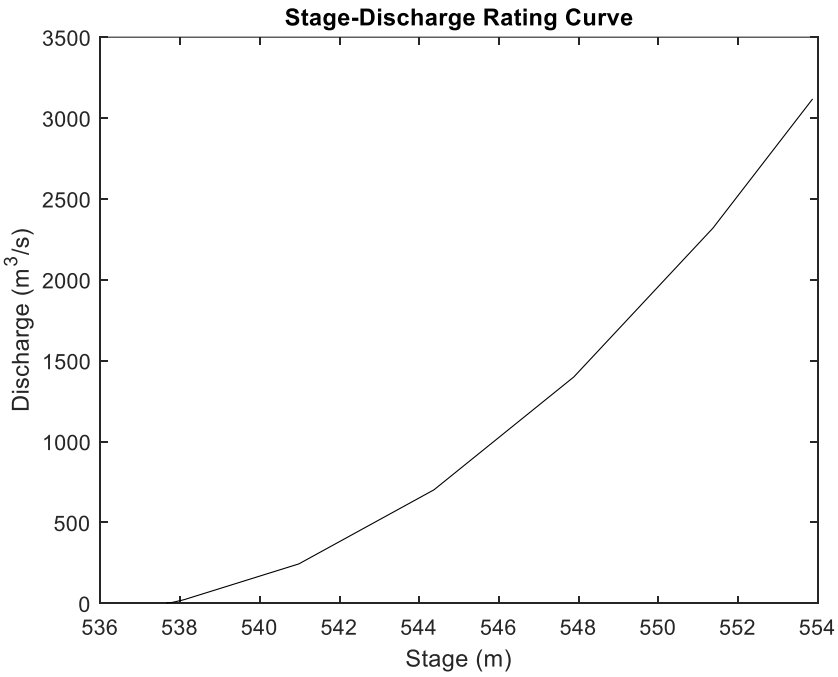

Figure 2.8. Downstream boundary condition stage-discharge rating curve for Reach 1 including bars 6 and 7. The original rating curve was created by Blythe (2018) and was adjusted for this study for topographic agreement between all topographic-related datasets in the hydraulic model analysis.

I calibrated channel roughness to minimize the root mean square error (RMSE) of modeled WSE versus measured WSE at the last modeled time step for a discharge of 18.5 m^3/s. This discharge, along with a water surface elevation profile, were measured at the study reach on January 14th in 2017 (Blythe, 2018), and was assumed to be low enough such that contribution of vegetation roughness was negligible. There was disagreement in the elevations between the DEM that was being used to build the model mesh, and the elevations from the WSE point data that were used to calibrate the model. To compensate for the error, I looked at the elevation difference at the downstream end of the reach and subtracted this difference (0.26 m) from the downstream boundary condition stage-discharge rating curve. This ensured topographic agreement between the mesh topography, rating curve, and water surface elevation measurements used in calibration. Water depth was underestimated using baseline bed roughness

values, so channel roughness was incrementally increased by 10%, 20%, 30%, 40%, and 50% to find optimal roughness values and minimize RMSE (Table 2.2). In the calibration process, increasing the spatially variable channel roughness regions by 40% resulted in an RMSE of 0.107 m (Table 2.2). Although the RMSE for the baseline and 10% increase calibration runs were lower, the number of matching WSE points for these two runs was considered insufficient. Therefore, the calibrated channel roughness values from increasing baseline values by 40% were used in the remainder of the hydraulic modeling analysis (Figure 2.9). Considering that the baseline channel roughness from Blythe (2018) was based on grain size only and not other forms of roughness such as bed forms or channel curvature, it is not surprising that baseline estimates were low and needed to be increased.

In addition to the available low flow data, WSE data were collected at a high flow of approximately 290 m^3/s (Blythe, 2018). Previous hydraulic modeling efforts, however, suggest a calibrated flow of 244 m^3/s matched water surface elevations best with an RMSE of 0.08 m (Blythe, 2018). I used the 244 m^3/s calibrated high flow as a validation flow in this study and performed a simulation using only channel roughness first. The simulated high flow also underestimated the modeled water depth with just channel roughness. Subsequently, I added vegetation roughness to increase modeled water depth, and created a calibrated and validated model that includes bed and vegetation roughness. Vegetation polygon data were mapped to the model mesh using SMS. Scenario 5 vegetation was used because it is the most similar to current vegetation conditions (Table 2.1). Where vegetation overlapped bed roughness, the baseline Manning's n value for the channel was added to the depth-varied Manning's n curve for the specific type of vegetation (Wang et al., 2019). Because the roughness of the upland regions (n=0.1) included vegetation, the bed roughness most prevalent on upper surfaces (n=0.0154) was

added to the vegetation roughness in these few regions. The resulting RMSE between measured and modeled WSE was 9.4 cm, which was deemed acceptable for a finalized calibrated and validated hydraulic model.

Table 2.2. Manning's n values for channel roughness during calibration runs at flow discharges of 18.5 m^3/s and 244 m^3/s. The floodplain roughness for the upland regions was kept constant assuming that flow would not reach these regions during calibration and because data in these regions were lacking. Shaded rows highlight calibrated (and validated) roughness values used in hydraulic modeling analyses.

Calibration run	Inlet discharge (m^3/s)	AC	FS1	FS2	FS3	Upland[a]	RMSE (m)
1 – Baseline	18.5	0.011	0.023	0.027	0.0306	0.1	0.062
2 – +10%	18.5	0.0121	0.0253	0.0297	0.0337	0.1	0.082
3 – +20%	18.5	0.0132	0.0276	0.0324	0.0367	0.1	0.129
4 – +30%	18.5	0.0143	0.0299	0.0351	0.03978	0.1	0.118
5 – +40%	18.5	0.0154	0.0322	0.0378	0.0428	0.1	0.107
6 – +50%	18.5	0.0165	0.0345	0.0405	0.0459	0.1	0.117
+40% – Bed roughness only	244	0.0154	0.0322	0.0378	0.0428	0.1	0.266
+40% – Bed and vegetation roughness	244	0.0154	0.0322	0.0378	0.0428	0.1	0.094

[a]Floodplain roughness of upland region obtained from Chow (1959).

Once the model was calibrated and validated for both low and high flows, I assigned species-specific depth-varied roughness curves to respective mesh cells for different modeling scenarios (Table 2.1, Figure 2.6). A total of 30 simulations were completed for six scenarios across five discharges, not including the runs completed during the calibration and validation process. Simulations were run for two hours at a time step of 0.25 s. For computational efficiency, a coarser resolution mesh was created using a grid spacing of 3 m near the active channel to run simulations for the 1000 m^3/s and 1490 m^3/s discharges.

Model outputs including flow depth and velocity were compared spatially at a cross-section located at Bar 6 through a vegetated region on river right (Figure 2.10), and in plan-view

at the reach scale to analyze plant species effects on hydraulics at the simulated discharges. Furthermore, I stratified the river corridor into three zones to compare model output within each zone: vegetated regions, the active channel, and the floodplain. The active channel boundary in this stratification was narrowed slightly to exclude the vegetated regions growing within the active channel.

Outputs were first converted within SMS into scatter data and then imported in ArcGIS Pro. In ArcGIS Pro, the scatter data were clipped to the respective river corridor zone using the Clip Layer tool. The vegetated regions were removed from the floodplain surfaces to isolate the output to just the floodplain using the Erase option within the Overlay Layers tool. Similar to Abu-Aly et al., (2014), the mean, median, maximum, and standard deviation were calculated for each scenario and flow combination. Formal statistical analyses were not appropriate to analyze hydraulic modeling results because data are unreplicated for a particular flow-scenario combination. Lastly, I created a channel centerline profile in SMS to inspect deviations from measured WSE at the 244 m^3/s discharge and modeled WSE for all model scenarios.

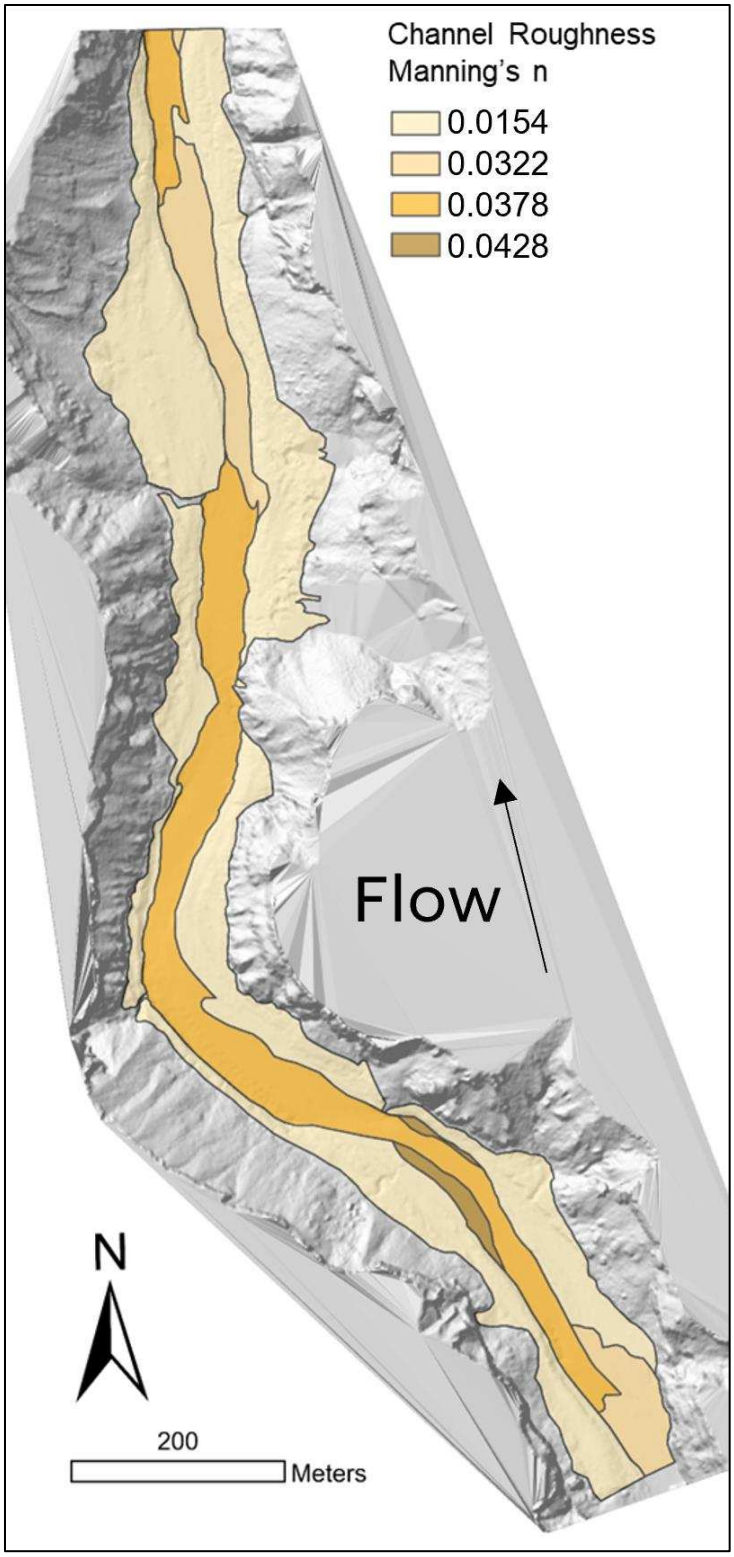

Figure 2.9. Spatially varied calibrated manning's roughness values for the channel. Calibrated values arose from increasing baseline bed roughness values by 40% to minimize RMSE between measured and modeled WSE at 244 m^3/s.

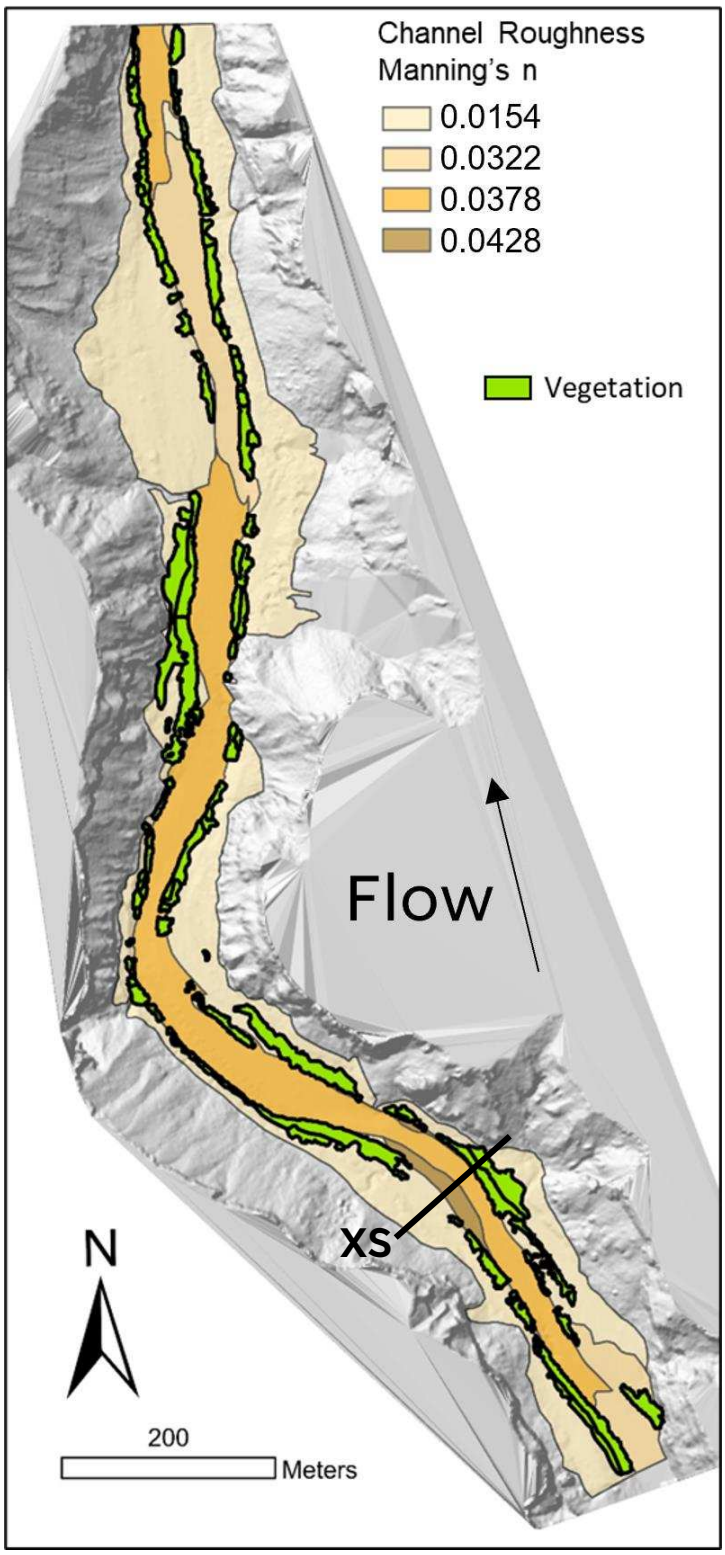

Figure 2.10. Map depicting the cross-section (XS) location (solid black line) used to analyze model results. The cross-section overlaps monumented sand bar 6 on river left and intersects patches of vegetation on river right.

2.3 Results

2.3.1 Plant and plot traits

The average non-normalized upright frontal area profiles are similar for giant cane and phragmites, but baccharis plants have higher magnitude upright frontal areas closer to the ground (Figure 2.11). A maximum upright frontal area occurs at 2 m for baccharis, 4 m for phragmites, and 6 m for giant cane (Figure 2.11). On average, giant cane was the tallest of the three plant species and baccharis the shortest (Figure 2.11; Table 2.3). Although baccharis plants were generally shorter than phragmites and giant cane plants, before normalizing by plant canopy area, most baccharis plants had higher cumulative upright frontal areas (Figure 2.12a). Larger stems were positively associated with higher flexural rigidity (Figure 2.12b). Plant height was the best predictor of upright frontal area for baccharis plants (R^2=0.98). Similarly, average stem diameter was the best predictor of flexural rigidity for baccharis plants (R^2=0.99). Cumulative upright and flexible plant and plot height-frontal area curves from photographed plants and stem counts are shown in Figures 2.13 and 2.14. Baccharis plants had the largest cumulative upright frontal areas (average = 5.3 m^2) before normalizing by canopy area. After normalizing, giant cane plants had the largest cumulative upright frontal areas (Figure 2.13; Table 2.3). Significant differences in normalized upright cumulative frontal area were found between plant species, for both plant and plot scale data ($p<0.01$). Processed photographs of upright plants can be found in Appendix A, Figure A1. Stem count data used to calculate plot frontal area can be found in Appendix A, Table A2.

Cumulative flexible plant frontal areas resulted in similar shaped curves for all plant species, but the frontal area for giant cane plants decreased and then increased again at higher

flow depths (Figure 2.13). The mean maximum flexible plant frontal areas are summarized in Table 2.4.

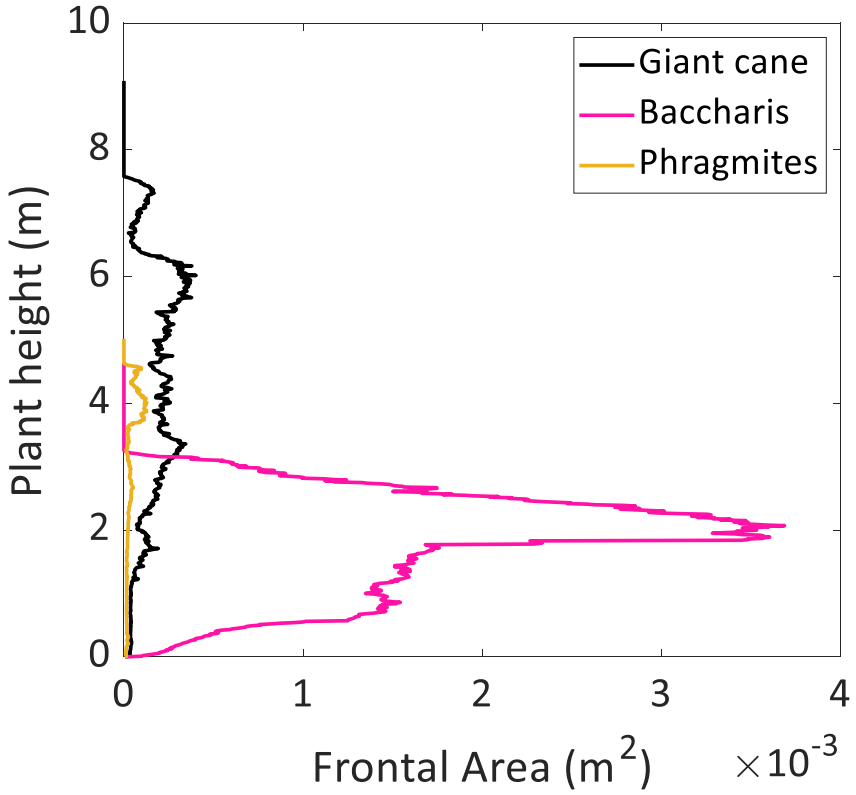

Figure 2.11. Average non-normalized upright frontal area curves for individual plants. These curves are essentially the raw data from the photographs of plants taken with a red background.

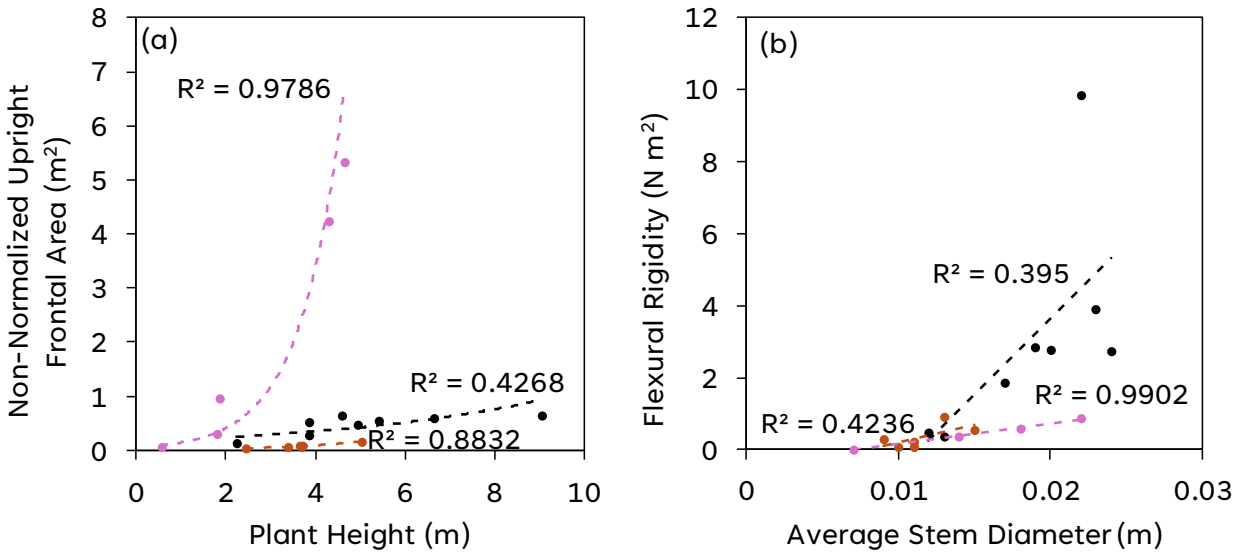

Figure 2.12. Relationships between (a) plant height and non-normalized upright frontal area, and (b) average stem diameter and flexural rigidity. Average stem diameter data are from stem sample collections.

Table 2.3. Summary of morphological-effect plant and plot traits. Individual plant and plot traits are provided in Appendix A, Tables A3 and A4.

	Plant Scale					Plot Scale		
Plant Type	Average Height (m)	Average Normalized Upright Cumulative Frontal Area[a]	Canopy Area (m^2)	Median Flexural Rigidity[b] $(N * m^2)$	Wet Stem Tissue Density[c] (g/cm^3)	Ground Stem Density $(\#stems/m^2)$	Average Ground Stem Diameter (cm)	Average Normalized Upright Cumulative Frontal Area[d]
Giant cane	5.1	1.011	0.47	2.01	0.73	82	1.8	4.024
Baccharis	2.6	0.470	4.1	0.78	0.84	77	0.9	1.320
Phragmites	3.6	0.673	0.24	0.49	0.67	123	0.9	1.884

[a]Sample sizes: Giant cane = 4, baccharis = 6, phragmites = 6. Upright cumulative frontal areas were normalized by plant canopy areas and then averaged for each species.
[b]Sample sizes: Giant cane = 16, baccharis = 24, phragmites = 16. An average flexural rigidity was calculated from all force-displacement measurements for each plant species, and then I calculated the median of those averaged values.
[c]Sample sizes: Giant cane = 8, baccharis = 7, phragmites = 3
[d]Upright cumulative frontal areas were normalized by plot areas and then averaged for each species.

Phragmites had the lowest median flexural rigidity and mean stem tissue density (Table 2.3). Giant cane had the highest median flexural rigidity while the median flexural rigidities of baccharis and phragmites were comparable (Table 2.3). Because one value of Baccharis flexural rigidity was anomalously high I used the median instead of the mean to characterize flexural rigidity for all species. Significant differences in flexural rigidity were found between plant species ($p=0.013$). Average stem tissue density was 0.729 g/m^3 for giant cane, 0.836 g/m^3 for baccharis, and 0.672 g/m^3 for phragmites (Table 2.3). Significant differences in wet stem tissue density ($p<0.01$) were also found between plant species. At the plot scale, giant cane had the largest total average diameter sum which resulted in the highest normalized rigid and flexible frontal areas (Figure 2.13; Table 2.3). The mean maximum flexible plot frontal areas are summarized in Table 2.4.

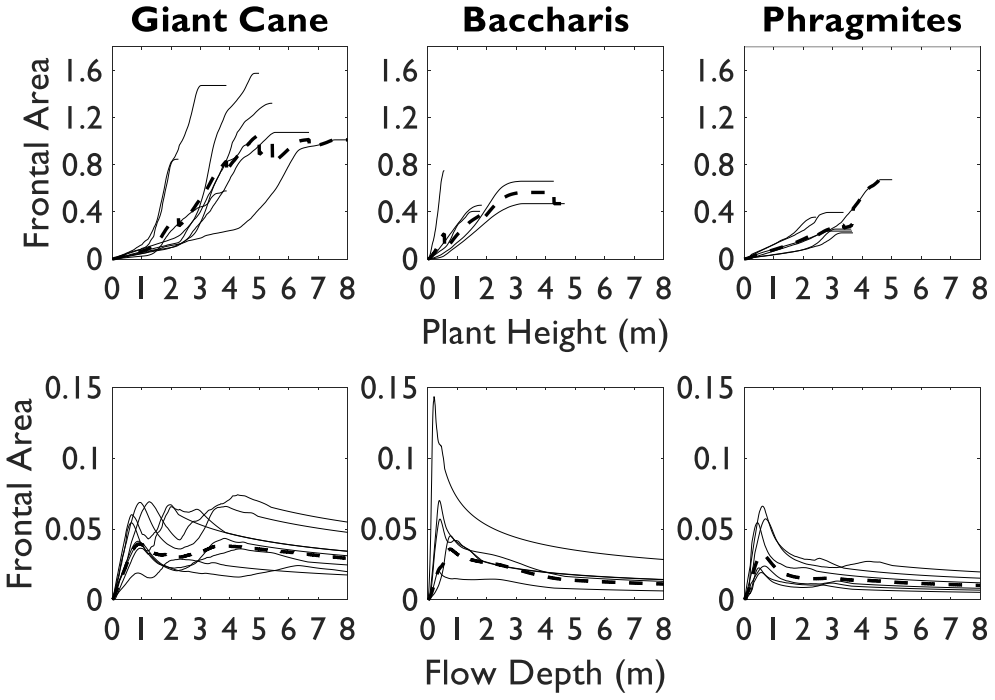

Figure 2.13. Frontal area curves for upright (top) and flexible (bottom) plants. Curves are normalized by plant canopy area. Solid lines represent individual plants and the dashed line represents the mean.

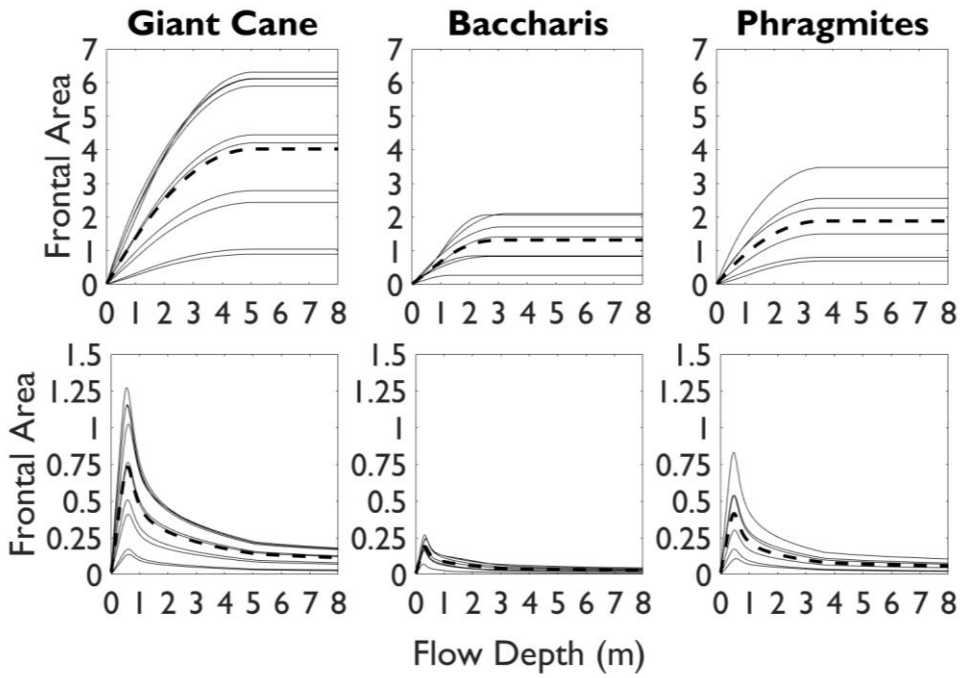

Figure 2.14. Frontal area curves for upright (top) and flexible (bottom) plots. Curves are normalized by plot area. Solid lines represent individual plants and the dashed line represents the mean.

2.3.2 Depth-varied vegetation roughness

Cauchy values increased as flow depth and velocity increased for all plant species (Equations 2.4 and 2.5). At the plant scale, Cauchy value was generally higher for giant cane plants and lowest for baccharis plants (Appendix A, Figure A3). One baccharis plant, however, had a low flexural rigidity (0.579 $N * m^2$) and very high upright frontal area (4.22 m^2), which resulted in very high Cauchy values (Appendix A, Figure A3). Cauchy values at the plot scale were essentially equal for all the giant cane and phragmites plots because the average plant height was used for plot scale calculations for those species (Appendix A, Figure A3). Cauchy values were larger for giant cane and phragmites at the plant scale compared to the plot scale, but the opposite is true for baccharis (Appendix A, Figure A3).

At the plant scale, mean normalized vegetation roughness for flexible plants was initially highest for baccharis at lower flow depths, but was surpassed by giant cane when flow depth

equaled 3.36 m (Figure 2.15). At this depth, vegetation roughness for flexible baccharis and giant cane plants both equaled 0.045. Vegetation roughness peaked faster (at lower flow depths) for upright baccharis plants compared to giant cane and phragmites, but giant cane had overall higher mean roughness (Figure 2.15). At the plot scale, mean vegetation roughness was highest for giant cane and the lowest for baccharis, for both upright and flexible cases (Figure 2.15). Baccharis had similar plot and plant scale roughness curves and comparable peaks (Table 2.4), but peak plot scale roughness was higher for giant cane and phragmites than plant scale roughness (Figure 2.15; Table 2.4). At flow depths greater than the height of the plant/plot, vegetation roughness stays relatively constant due to an assumed constant maximum frontal area after this point.

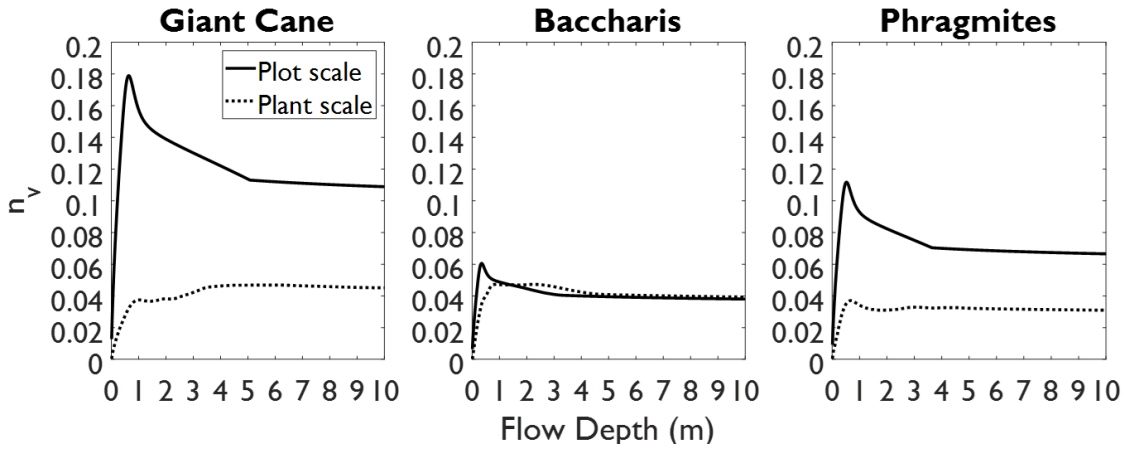

Figure 2.15. Depth-varied vegetation roughness for specific plant species calculated at the individual plant and plot scales.

Table 2.4. Summary of mean maximum flexible plant and plot vegetation roughness and where those maximums occur within the flow column (Figure 13).

Plant Species	Scale of analysis	Maximum	Flow Depth location (m)
Giant Cane	Plant	0.05	6.06
	Plot	0.18	0.64
Baccharis	Plant	0.05	0.89
	Plot	0.06	0.36
Phragmites	Plant	0.04	0.68
	Plot	0.11	0.53

2.3.3 Vegetation on flood surfaces

Within the entire reach, vegetation covers 65% of the mapped channel and floodplain areas (Table 2.5). Giant cane, baccharis, and phragmites make up 29%, 60%, and 11% of the vegetation, respectively (Figure 2.16). No occurrence of baccharis, phragmites, or giant cane were recorded on the topographically higher flood surface 3 (FS3; Figure 2.17). Although the 3 species of interest have overlapping distributions, baccharis is generally found at lower elevations closer to the channel, phragmites is found at moderate elevations and giant cane at higher elevations. Generally, baccharis was found growing on all geomorphic surfaces except FS3 but is most common within the active channel and on FS1 (Table 2.5; Figure 2.17). Baccharis is distributed across all elevations within the active channel (Figure 2.17a) but is more common at lower elevations, approximately 1 m above the 2018 low-water surface elevation (Appendix A, Table A4). Sixteen percent of the active channel area is covered by baccharis, and 20% of FS1 (Table 2.5). Although baccharis covered almost a quarter of FS2, its growth is constrained to lower elevations compared to giant cane (Figure 2.17c). Phragmites demonstrated a similar behavior to baccharis on FS2 (Figure 2.17c). Giant cane is also found on all surfaces except FS3 but was widespread on FS1 (Figure 2.17b). Of all four geomorphic surfaces, giant cane was more abundant on FS1 (Table 2.5). Giant cane and phragmites were essentially not found to grow within the active channel (Table 2.5; Figure 2.17a). The mean elevations at which baccharis, phragmites, and giant cane are found on each geomorphic surface relative to the 2018 water surface profile are summarized in Appendix A, Table A4.

Table 2.5. The percentage of total area each plant species occupies on geomorphic surfaces within the study reach. The sum of these total areas suggests that 65% of the mapped geomorphic

surfaces are covered by vegetation. AC refers to active channel, and FS1, FS2, and FS3 refer to flood surfaces 1, 2 and 3, respectively.

	AC	FS1	FS2	FS3
Giant Cane	1	8	7	0
Baccharis	16	20	6	0
Phragmites	1	5	2	0

A flood with a magnitude of approximately 230 m^3/s would be needed to inundate FS1 to giant cane's median growing elevation (Table 2.6). The discharge needed to inundate FS2 was higher than FS1 for giant cane but was lower for baccharis and phragmites (Table 2.6). The percentage of FS2 inundated for baccharis and phragmites was only 6% and 5%, respectively, possibly where very small portions of FS2 extend to lower elevations closer to the center of the channel. There are likely mapping errors associated with the vegetation-elevation histograms because in general, the magnitude of inundating discharge for FS2 should be higher than FS1 and the active channel.

Table 2.6. Approximate inundating discharges (m^3/s) for specific plant species with respect to geomorphic units. The last row shows the median inundating discharge for each geomorphic surface.

Plant Species	Active channel	Flood surface 1	Flood surface 2
Giant cane	N/A	230	385
Baccharis	18	175	50
Phragmites	N/A	70	30
Geomorphic surface	N/A	240	750

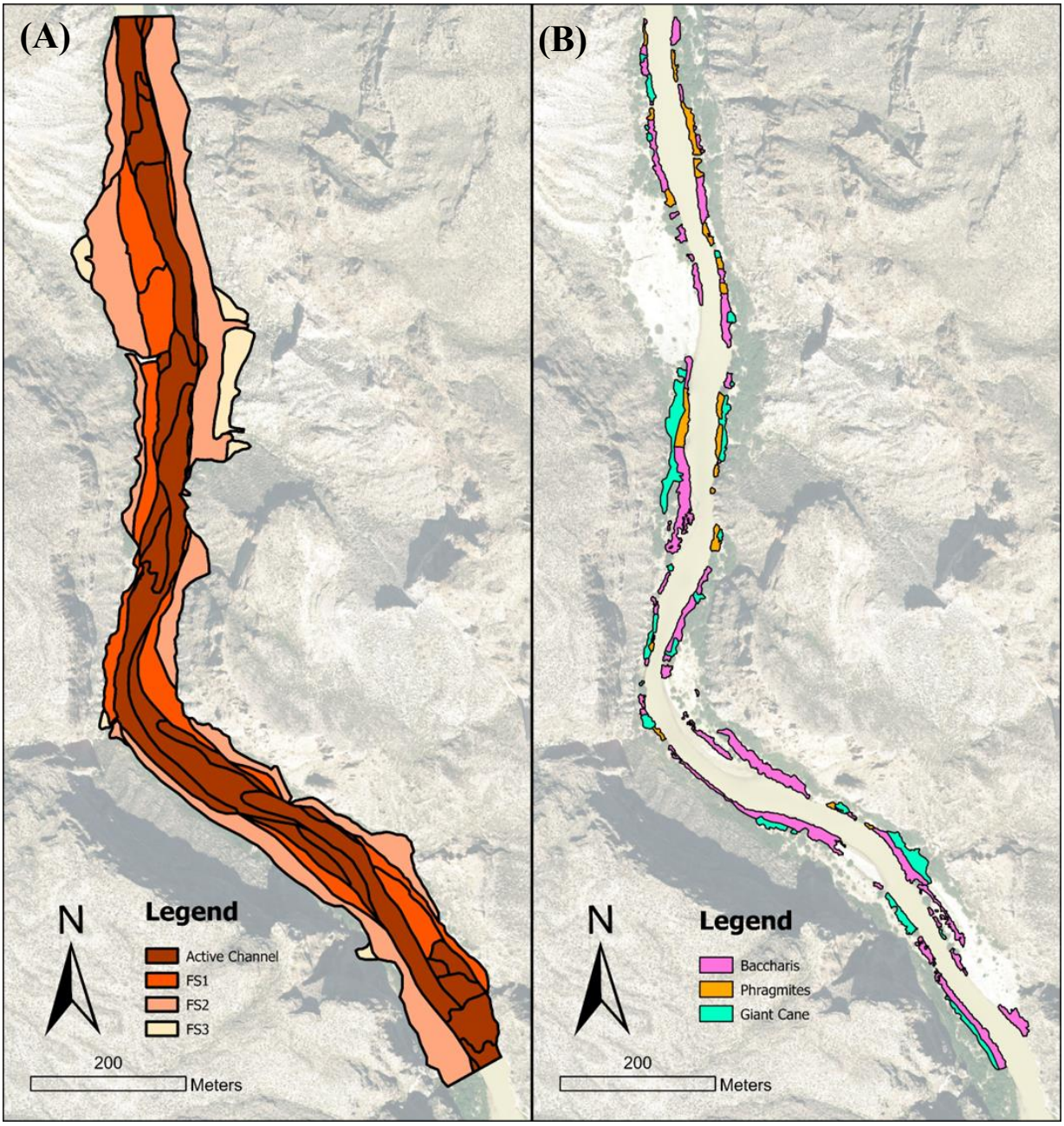

Figure 2.16. Maps of (A) geomorphic units (Blythe, 2018), and (B) vegetation units in the modeled study reach.

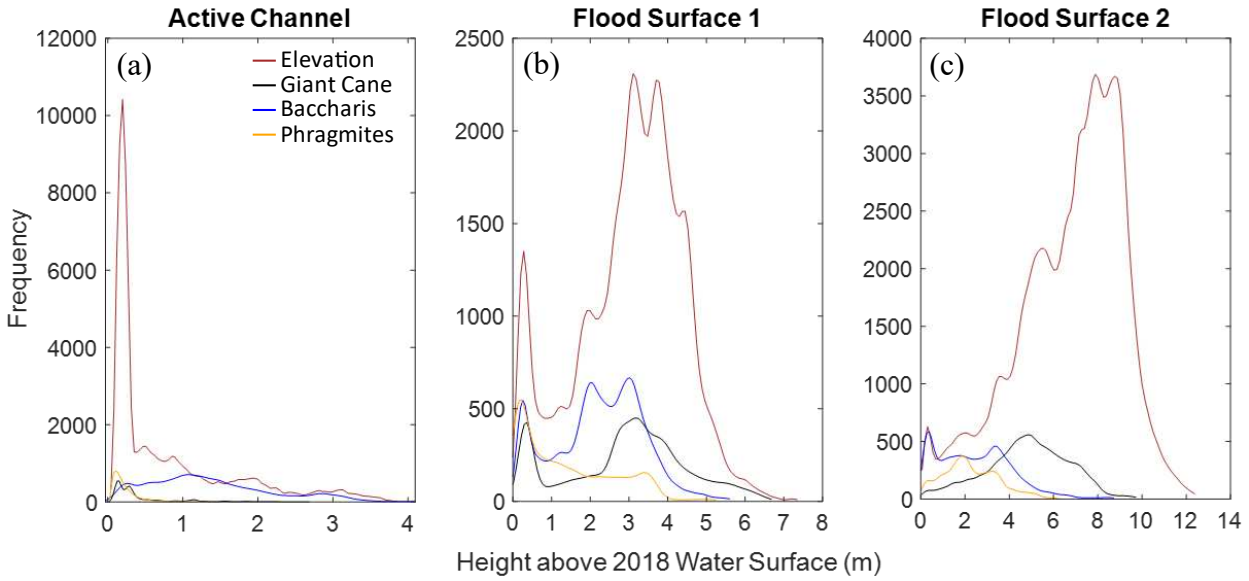

Figure 2.17. Cumulative histograms of detrended elevation for Giant Cane, Baccharis, Phragmites and all surface cover types on the (a) active channel, (b) flood surface 1, and (c) flood surface 2.

2.3.3 Hydraulic Modeling

Results of the hydraulic modeling indicate that, with the addition of vegetation (Scenarios 2-5), mean velocity was reduced in the vegetated areas, active channel, and unvegetated floodplain at all discharges (Figure 2.18). In all vegetated scenarios, vegetation steered flow to the center of the active channel such that high velocity zones narrowed and low velocity zones on channel margins widened (Figure 2.19). Cross-section results also indicate higher velocities occur within the active channel when plants are added (Figure 2.18), and giant cane increased active channel velocities the most compared to baccharis and phragmites (Figure 2.20). On the unvegetated floodplain and in vegetated regions, the giant cane scenario yielded the highest flow depths and lowest velocities compared to all other scenarios for all discharges (Figure 2.18). At lower discharges (100 m^3/s, 200 m^3/s, and 500 m^3/s), velocity was lower on the channel margins with the addition of plants, but at higher discharges (1000 m^3/s and 1490 m^3/s), higher velocities were seen on the river-right portion of the channel (Figure 2.18). When giant cane was removed

from the model (Scenario 6), reach-scale velocities increased (Figures 2.18 and 2.21) and flow depths decreased within the vegetated regions and unvegetated floodplain (Figure 2.18). Cross-section results indicate velocity in formerly vegetated zones increased by as much as an order of magnitude when giant cane was removed (Figure 2.21).

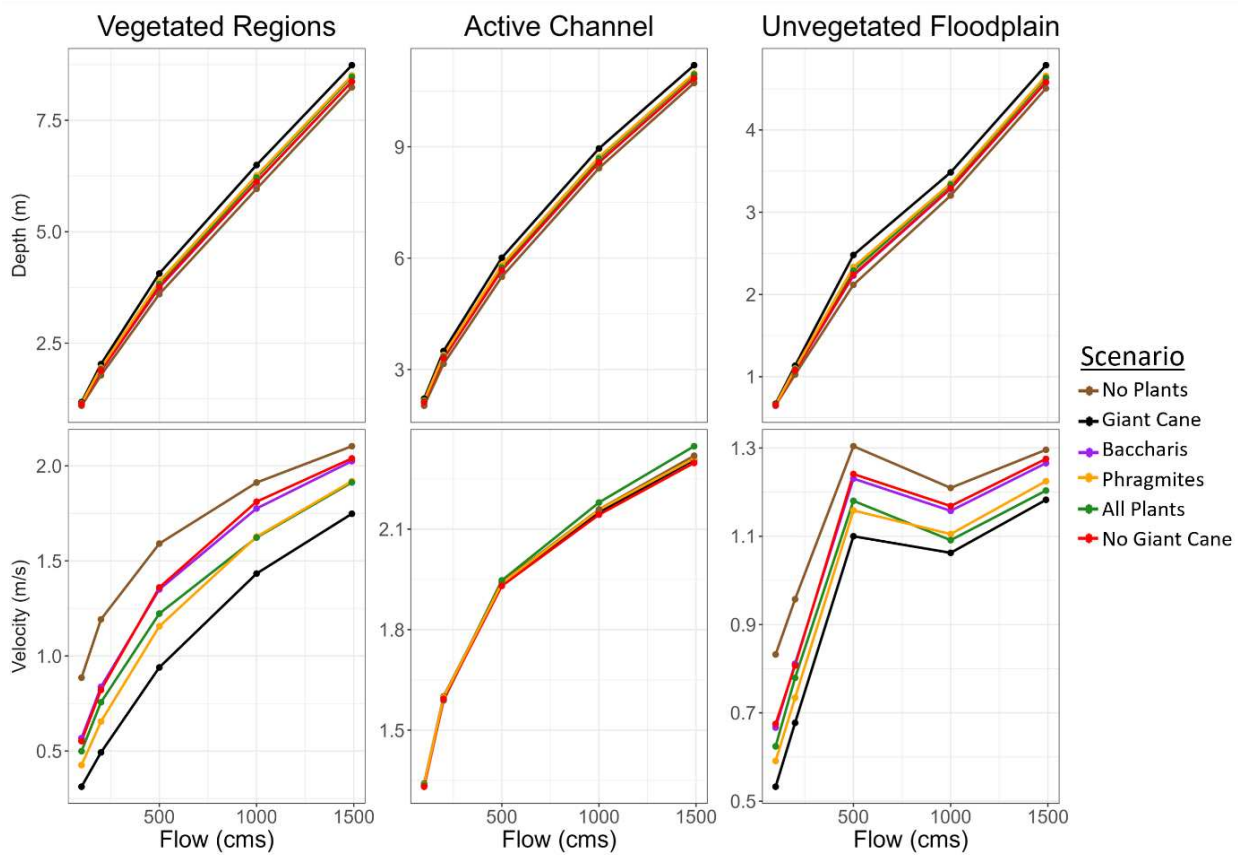

Figure 2.18. Mean values for flow depth and velocity within (left) vegetated regions, (middle) the active channel, and (right) the unvegetated floodplain. These data along with median, standard deviation, minimum, and maximum are included in Appendix A, Tables A5-A7.

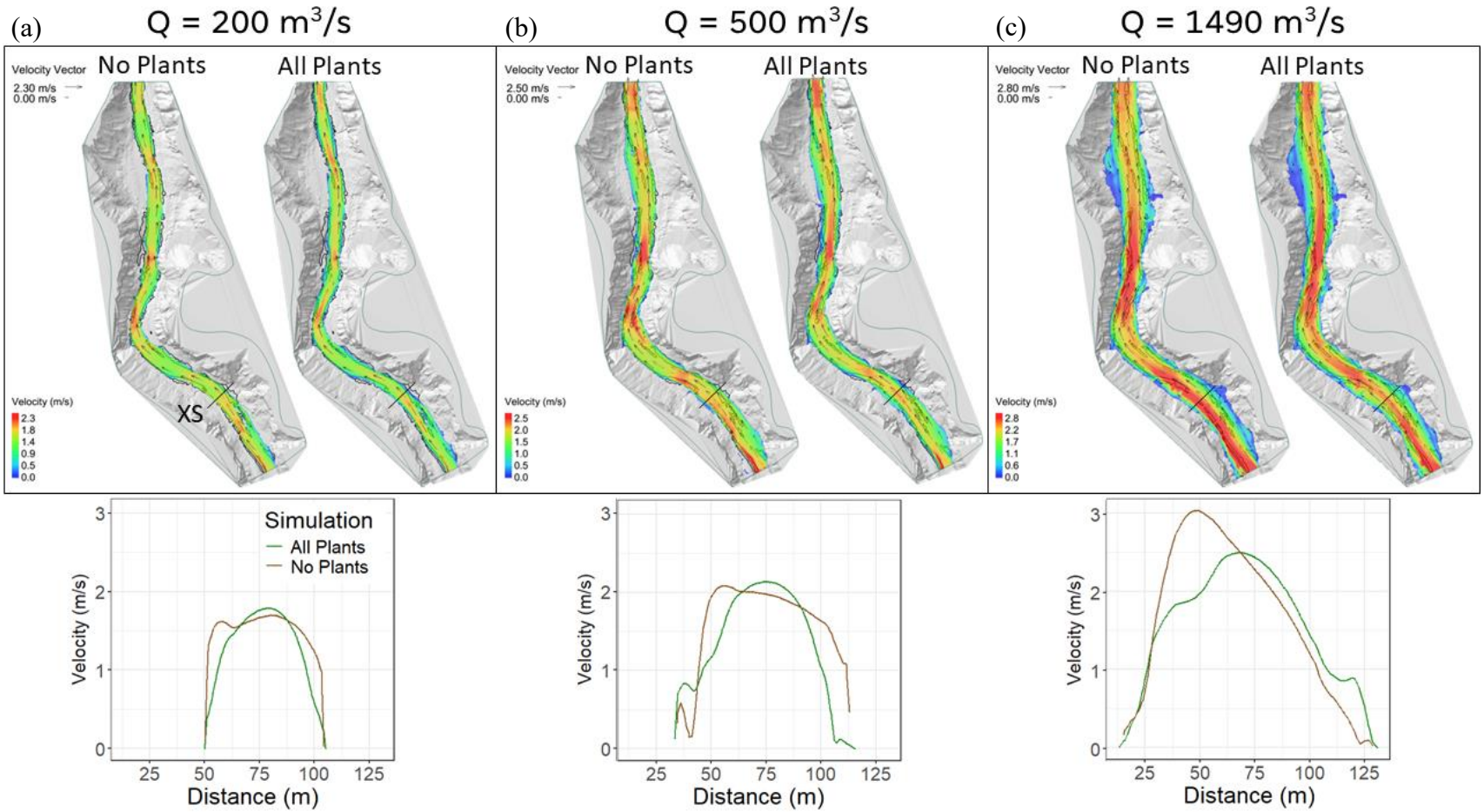

Figure 2.19. A comparison of the influence of vegetation (Scenario 5) to the no-vegetation scenario (Scenario 1) at the reach scale and at a cross section at Bar 6 for (a) 200 m^3/s, (b) 500 m^3/s, and (c) 1490 m^3/s.

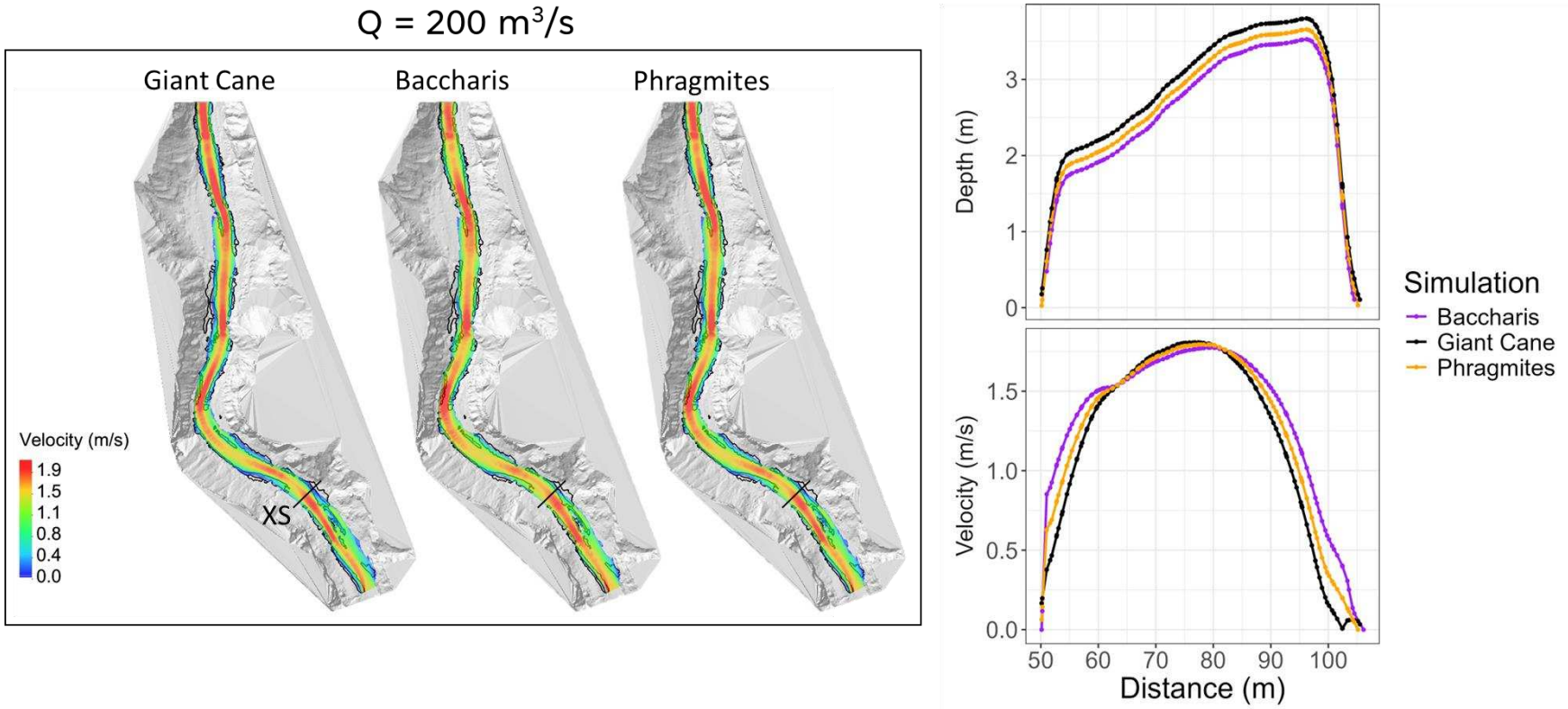

Figure 2.20. Reach-scale velocity results for scenarios 2-4 at a simulated discharge of 200 m^3/s. Cross-section results include both depth and velocity for each scenario.

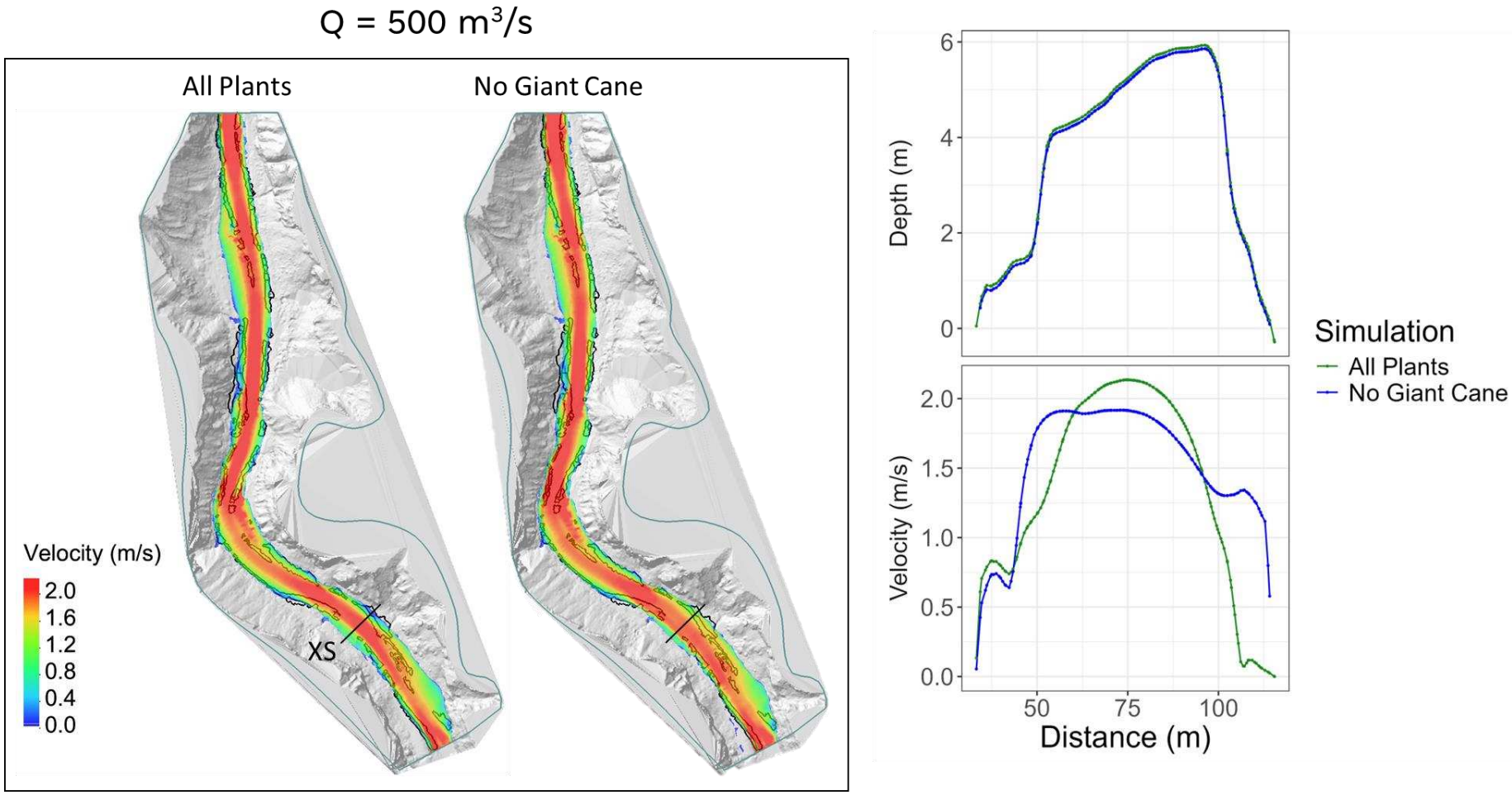

Figure 2.21. Reach-scale effects of giant cane removal on velocity. Cross-section results include both depth and velocity for each scenario.

Replacing all existing vegetation with giant cane (Scenario 2) led to approximately 30 cm of WSE increase within the modeled reach (Figure 2.21). In contrast, when giant cane polygons were removed from the model without replacement (Scenario 6), the WSE decreased by around 10 cm (Figure 2.21).

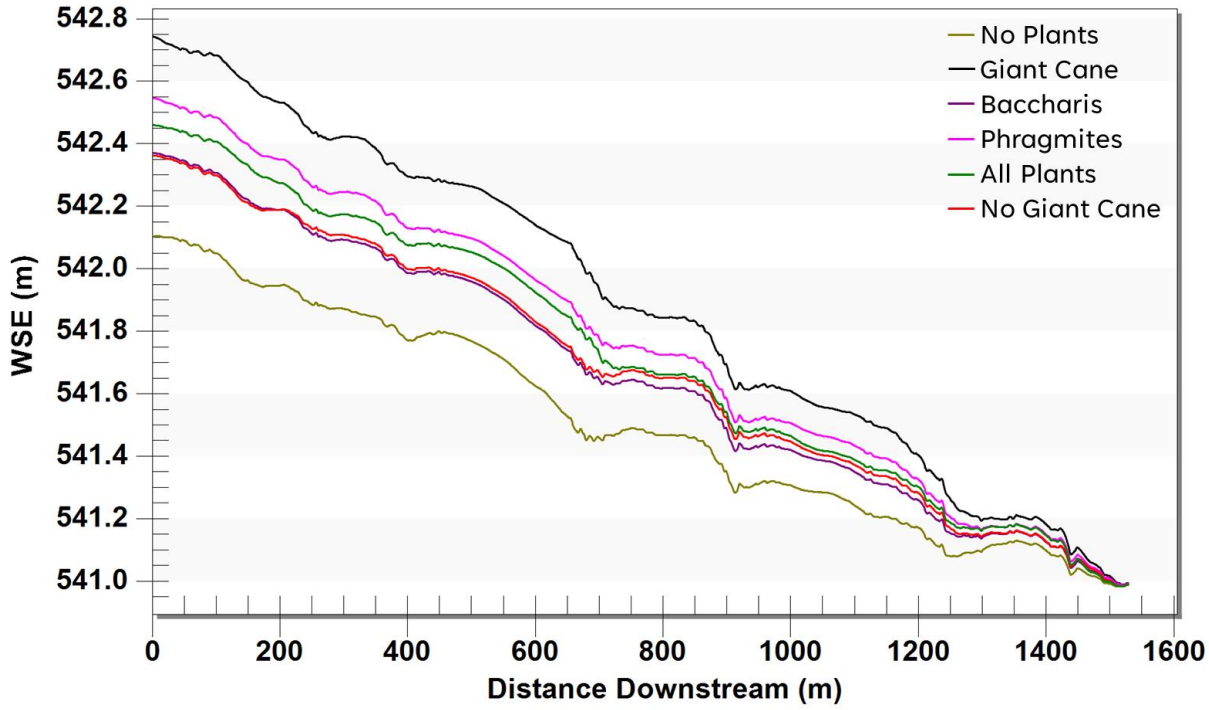

Figure 2.22. Centerline WSEs for different modeling scenarios. WSE converges at the downstream boundary of the modeled reach due to the stage-discharge rating curve boundary condition.

2.4 Discussion

2.4.1 Plant and plot scale data

My results suggest scaling up from the plant, plot, and reach scales was essential for accurately calculating vegetation roughness and for reach-scale hydraulic modeling. Moving from the plant to the plot scale, larger increases in roughness were observed in giant cane and phragmites compared to baccharis due to the dense packing of the grasses. The spreading

architecture of baccharis produces less flow resistance than the more vertical, tightly packed patches of giant cane and phragmites (Figure 2.11) (Lightbody and Nepf, 2006; Stone et al., 2013). For individual plants, the plant architecture is reflected in the flexible frontal area. Unexpectedly, giant cane and phragmites plants resulted in more complex frontal area-flow depth relationships, showing increasing and decreasing fluctuations in flexible frontal area (Figure 2.13). Giant cane and phragmites have unbranched leafless stalks near the ground but more complex architectures higher up, where leaves and branches are present (Figure 2.11). The flexible frontal area curves suggest giant cane and phragmites likely bend over where frontal area decreases (around 1-3 m flow depth for giant cane and 1-2 m flow depth for phragmites), but when flow inundates the leaves in the upper portion of the plant, frontal area increases again (Figure 2.13). The shorter, more strongly branching architecture of baccharis (Appendix A, Figure A1; Figure 2.11) may result in more consistent decreases in flexible frontal area with increasing flow depth (Figure 2.13). Unraveling the intricacies of frontal area, as presented here, is critical to understanding how vegetation deforms under different flow conditions, modifies flow and sediment transport, and influences channel morphology.

The hypothesis that giant cane will have larger normalized frontal areas at the plant and plot scale (H1a) is supported by my findings. Hypothesis 1b, however, was partially supported. Roughness decreased at higher flow depths due to the flexible nature of modeled plants. Although giant cane and phragmites are grasses and baccharis is a woody plant, giant cane had the highest flexural rigidity (Table 2.3). Giant cane is often mistaken for bamboo (Giessow et al., 2011), and field observations suggest that giant cane is in fact more rigid than woody baccharis. This finding is especially important because flexural rigidity strongly influences the Cauchy

number (Equation 2.4 and 2.6), which affects the effective height (Equation 2.8), effective frontal area (Equations 2.9 and 2.10) and vegetation roughness (Equations 2.11 and 2.12) calculations.

Frontal area and flexural rigidity were comparable to values reported in the literature (Table 2.7). The median non-normalized frontal area for phragmites and baccharis in this study were comparable to the frontal area for phragmites and within the range between seedling and mature *Salix exigua* in Diehl et al. (2017) (Table 2.7). For giant cane, frontal areas between this study and Speck (2003) were also comparable. The calculated flexural rigidities of baccharis are comparable to mesic shrubs measured by Diehl et al. (2017) but are generally lower than *Salix* specimens measured by Whittaker et al. (2015) and willow specimens measured by Stone et al. (2013). Giant cane was found to be more flexible in this study compared to Speck and Spatz (2003) (Table 2.6). The size and age of the plant species, spacing and density of plants, and methods used to measure plant traits will ultimately factor into differences between studies.

Table 2.7. Non-normalized median frontal area and flexural rigidity comparisons for upright individual plants between this study and others.

Reference	Frontal Area (m^2)			Flexural Rigidity ($N * m^2$)		
	Giant Cane	Baccharis	Phragmites	Giant Cane	Baccharis	Phragmites
This study	0.52	0.96	0.07	2.76	0.58	0.24
Diehl et al. (2017)[a]	--	0.021-0.024	0.04	--	0.039-1.95	0.23
Stone et al. (2013)[b]	--	3.8	--	--	3.2	--
Whittaker et al. (2015)	--	0.592[c]	--	--	113[d]	--
Freeman et al. (1998)	--	0.039[e]	--	--	0.74[f]	--
Speck (2003)	0.21[g]	--	--	--	--	--
Speck and Spatz (2003)	--	--	--	1.36[h]	--	--

Wang et al. (2019)	--	--	--	0.67[i]	--	--

[a]Frontal area and flexural rigidity for baccharis compared to *Salix exigua, ranging from seedling to mature*.
[b]Frontal area and flexural rigidity for baccharis compared to *Salix spp.*.
[c]Frontal area compared to the average of 11 samples of foliated *Salix alba*.
[d]Flexural rigidity compared to the average of 13 samples of *Salix alba*.
[e]Frontal area compared to *Baccharis glutinosa*.
[f]Approximated upright total projected surface area of a typical giant cane plant used in wind experiments.
[g]Calculated using the modulus of stiffness and stem diameter of 0.0126 m.
[h]Calculated using the average Young's modulus of elasticity in the Y-direction and an average stem diameter of 2.5 cm.
[i]Calculated using the modulus of stiffness and stem diameter of 2.5 cm.

I expected vegetation roughness to be higher when based on applying the photograph method to induvial plants than when based on direct measurement of stems in plots because plant leaves are included in the calculation of frontal area from the photograph method. Stem counts exclude leaves, which should result in lower roughness (Järvelä, 2002). However, normalized plot scale frontal area for giant cane and phragmites was much larger than normalized frontal area at the individual plant scale, most likely due to the occurrence of densely packed stands with overlapping plant canopies. Tightly spaced stems within uniform stands of giant cane and phragmites lead to slower, more uniform flow with minimal variability in sedimentation depth within patches (Perignon et al., 2013), and to redirection of flow around dense vegetation patches (Manners et al., 2013). The plot and plant scale roughness curves for baccharis are essentially the same, however, suggesting that plants are relatively widely spaced, perhaps as a result of spreading plant architecture and shade intolerance.

The vegetation roughness curves calculated in this study are comparable to those of others who have calculated roughness for flexible plants from empirical, flume, and field-based approaches (Figure 2.20). The approaches by Freeman et al. (2002) and Whittaker et al. (2015)

explicitly consider plant bending in response to flow, but the Järvelä et al. (2004) approach incorporates flexibility into a Vogel exponent (Shields et al., 2017). Regardless of how plant flexibility was considered, a consistent pattern of how roughness increases with increasing flow depth is generally lacking (Figure 2.23). The variability in the results for relatively shallow flows likely arises from complexities in plant architecture, differences in experimental methods and spatial scales, and assumptions behind plant emergence versus submergence. It is evident, however, that once plants are fully submerged (flow depth equals plant height), roughness stays relatively constant (Figure 2.23). The roughness values from this study are within an order of magnitude of those of the other studies, but plant reconfiguration occurs at shallower depths in this study (Figure 2.23). The average roughness curve for baccharis suggested that the plant bends over relatively quickly, just before a quarter of the plant's height (Figure 2.23). During a flood I encountered while collecting field data in 2021, however, I observed baccharis to bend over at higher flow depths. There could be some error associated with the calculations for baccharis because the equations I used were derived for small single bladed grasses, not woody shrubs. Through a sensitivity analysis, I determined that increasing flexural rigidity strongly increased the peak roughness and weakly shifted the curve to the right. Nonetheless, these changes in roughness make sense: more rigid plants (higher flexural rigidity) increase roughness and do not pronate as easily, and thus bend at higher flow depths. Increasing frontal area also increases the magnitude of roughness. Although phragmites was the least rigid, the high plot scale frontal area outweighed flexural rigidity and contributed to high roughness. Additional sensitivity analyses would help to fully understand the effects of frontal area and flexural rigidity on vegetation roughness at both plant and plot scales.

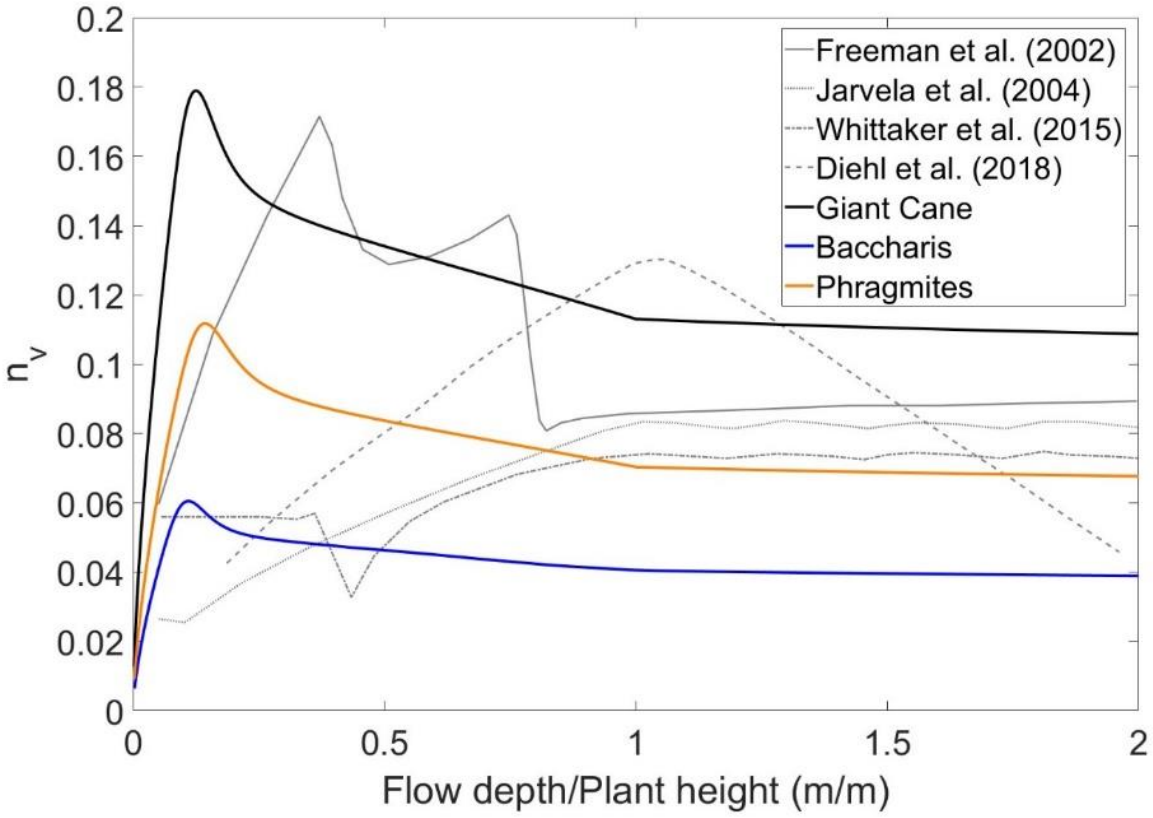

Figure 2.23. A comparison of the vegetation roughness curves calculated for flexible plants in this study and others.

2.4.2 Hydraulic modeling

The three studied plant species have different geomorphic responses to flooding based on the observed hydraulics. At the reach scale, the overall higher roughness of giant cane resulted in lower mean velocities and higher mean flow depths, suggesting increased sediment deposition. Giant cane stands function similarly to levees, concentrating flows within the active channel areas and over time, deepening of the channel. Eventually, this may lead to a transformation of the system from a braided unstable channel form to a laterally stable single thread channel form (Giessow et al., 2011). Subsequently, the hydraulic modeling analysis supports the findings from others that invasive plants contribute to channel narrowing more so than native plants (Fei et al., 2014; Martinez et al., 2016; van Oorschot et al., 2017). A shift in the vegetation community from

the natural distribution of plants (Scenario 5) to all giant cane (Scenario 2) indicates strong vegetation feedbacks and negative ecosystem responses, such as vegetation-enhanced deposition and reduced channel braiding (Bywater-Reyes et al., 2022). Furthermore, the analysis supports hypothesis 2 and suggests that removing giant cane increases velocities on the floodplain and likely increases erosion, which could reverse the trend of channel narrowing. Another consideration is the transport-limited, sediment-laden nature of the Rio Grande. Due to severe upstream flow regulation, tributary-sourced floods are capable of depositing abundant fine-grained sediment (Dean & Schmidt, 2010; Dean et al., 2016). Although reach-scale velocities increased when giant cane was removed (Figure 2.7), in the absence of relatively frequent, large magnitude erosive floods, the geomorphic effects of giant cane removal efforts may go unnoticed.

There was a consistent trend of a wider distribution of lower velocities on the channel margins and more concentrated higher velocities in the main portion of the active channel throughout all scenarios with vegetation (Scenarios 2-6). These results suggest that vegetation steers flow to the channel center, shifts the high-velocity zone, and has implications for sediment transport and channel morphology. Bywater-Reyes et al. (2018) found similar flow steering effects from vegetation on a point bar with an increasing effect with discharge, plant density, and plant size. The trend of lower velocities on channel margins due to vegetation was prevalent for lower discharges (100 m^3/s, 200 m^3/s, and 500 m^3/s), but at higher discharges, velocities increased on the channel margins for scenarios with vegetation than without (Figure 2.17c). At higher discharges, plants are assumed to be fully pronated such that their effect on hydraulics is drowned out as stage increases. This was corroborated with a quantified decrease in vegetation roughness (Figure 2.13) and could explain the increase in velocities at higher discharges. On the

other hand, velocities could be influenced by the confined nature of the canyon (Legleiter et al., 2007). The bulk channel morphology at the reach scale was more important in influencing velocities at higher discharges than roughness elements in Legleiter et al., (2007), and a similar effect could be at play in Boquillas Canyon.

Wang et al. (2019) compared vegetation roughness calculation methods using a HEC-RAS 1D hydraulic model and found the Whittaker et al. (2015) approach used here more accurately predicted roughness values and river stage than all other roughness methods. Furthermore, I incorporated direct field-based measurements of upright frontal area for individual plants, as opposed to using indirect estimates of frontal area from LAI. LAI can be measured directly (Lama et al., 2021), but could be most useful if only remotely sensed data are available. Wang et al. (2019) observed similar reach-scale velocities to this study at a flow of approximately 200 m^3/s in a 1D spatially varied hydraulic model. In Chaulagain et al. (2022), vegetation roughness also varied horizontally and vertically based on methods that incorporate LAI (Järvelä, 2004) and stem density (Baptist et al., 2007). Comparable to this study, the stem density approach (Baptist et al., 2007) yielded higher roughness values than the LAI approach (Järvelä, 2004). The Manning's roughness of riparian willows (assumed to be similar to baccharis) in Chaulagain et al. (2022) were generally larger than the roughness of baccharis in this study. More specifically, roughness of riparian willows ranged from 0.031 to 0.23 across all computed methods (Chaulagain et al., 2022).

2.4.3 Management Implications

Plants with larger frontal area, more rigid stems, and/or more complex architecture enhance deposition, floodplain aggradation, and simplification of channel morphology (Bywater-Reyes et al., 2022). Invasive giant cane had the largest normalized frontal areas and the highest

rigidity, which created high hydraulic roughness and slowed flow velocities. These findings suggest giant cane decreases conveyance, and likely increases sediment deposition and channel narrowing along the Rio Grande in Big Bend National Park. Additionally, giant cane is found growing on numerous geomorphic surfaces and so has expanded to cover large areas within the riparian zone (Figure 2.17). Positive feedbacks have been identified between reduced stream flows, thick bank vegetation, and reductions in channel capacity (Dean & Schmidt, 2011), presumably due to invasive plants including giant cane along the Rio Grande. Infrequent and large magnitude reset floods have been found to temporarily reverse channel narrowing (Dean & Schmidt, 2011), but riparian vegetation may limit the effectiveness of reset floods (Tal et al., 2004; Dean & Schmidt, 2011). As a result, natural resource managers have spent almost a decade treating invasive vegetation to limit channel narrowing and increase sediment and water conveyance. Hydraulic modeling results indicate a channel filled entirely with giant cane (Scenario 2) decreased water conveyance, but areas where giant cane was removed resulted in higher floodplain velocities and marginal improvements to water conveyance (Figure 2.21). Generally, these findings link to the two disequilibrium cases presented in the Green New Balance of Bywater-Reyes et al., 2022 where vegetation community shifts influence ecosystem responses, presumably either by vegetation-enhanced deposition (Scenario 2) or vegetation-enhanced scour (Scenario 6). When invasive vegetation is treated, plant influences are diminished and the effects of transport capacity and sediment supply increase (Bywater-Reyes et al., 2022). But how effective is giant cane removal if sediment remains trapped on higher surfaces where giant cane primarily grows (Table 2.5; Figure 2.17) due to a lack of high magnitude floods? Vegetation-elevation histogram analyses indicated floods of 230 m^3/s and 385 m^3/s would be needed to inundate giant cane to its median growing elevation on FS1 and FS2,

respectively. Based on a flood frequency analysis, these inundating discharges recur approximately every 1.5 and 2.5 years, suggesting that giant cane grows at lower elevations where moderately frequent floods are capable of flushing sediment in giant cane treated areas on FS1 and FS2 (Figure 2.17). Management should consider treating giant cane on these lower surfaces, specifically where bank slumping and collapse may occur to facilitate bank erosion (Stover et al., 2018) to maximize their efforts. Furthermore, how effectively would the 1.5- or 2.5-year floods scour giant cane? Similar to invasive tamarisk, giant cane's high frontal area and stem density implies it is also resistant to scour. Kui et al. (2018) found that depending on the morphology and density of the invasive plant, flows aimed at scouring or dislodging riparian plants may be impractical. Additionally, the rhizomatous root structure of giant cane suggests it has added strength and propagates easily. Gilbert and Wilcox (2021) found that giant cane rhizomes are easily transported by flood flows and deposited downstream. Higher magnitude flows could help to erode sediment after giant cane has been removed, but if rhizomes are still present, could also lead to more giant cane downstream. Management questions remain in linking the rate of species-specific vegetation expansion with geomorphic change and providing clear guidelines to invasive species management along the Rio Grande.

Vegetation roughness from native baccharis was less than giant cane or phragmites (Figure 2.15), but baccharis was commonly found growing in the active channel (Figure 2.17). The low flexural rigidity of baccharis suggests that it is flexible enough to bend over instead of break during floods, which limits its resistance, results in lower hydraulic roughness, and improves its chances for survival in high velocity environments. But, if decreasing channel narrowing is a goal of natural resource managers and baccharis is prolific in the active channel, should the management attention be shifted to baccharis? Vegetation-elevation histogram findings suggest

baccharis that grows within all geomorphic surfaces (except FS3) that are inundated more frequently than the approximate two-year recurrence flood of 250 m^3/s (Table 2.5). Furthermore, floods in the lower Rio Grande are depositional, and although baccharis may not be as hydraulically rough as giant cane or phragmites, it is more likely to trap sediment based on its geomorphic setting and thus contribute to reduced channel capacity. Interestingly, baccharis made up 60% of the vegetation in the hydraulic model, and a channel where giant cane is removed resorted back to a baccharis-filled channel (Figures 2.15, 2.17). Baccharis may contribute more than giant cane to channel narrowing because of its ability to colonize low sand bars, but giant cane may contribute more to raising flood stage and reducing channel migration because of its higher roughness and ability to survive higher on the floodplain. Questions may also be raised regarding native phragmites due to its high vegetation roughness and low discharge (70 m^3/s) to inundate FS1. These findings stress the importance of evaluating the geomorphic influence of all riparian plants, not just non-native invasive species, to help inform and prioritize vegetation management efforts.

2.4.4 Limitations and Future Work

The buoyancy of the plant species in this analysis was poorly constrained because it was difficult to determine the volume of a plant. Methods that rely on stem diameter estimates are problematic because of the complex variation of stem diameter and number within and between plants. A sensitivity analysis based on values seen in the literature revealed changing buoyancy from 2 to 200 greatly impacted the vegetation roughness at both the plant and plot scales, for all plant species. It is recommended that future work include buoyancy in vegetation roughness calculations using additional field data, including cutting and weighing entire plants in the field as well as measurements of wet tissue density of stems, leaves and entire branches.

Additional field data should also involve taking photographs of plots to compare frontal area results with those obtained from stem counts. Also, flexural rigidity was measured at different heights of the plant stem, but an average was used to calculate buoyancy and Cauchy values. To more accurately estimate how Cauchy and buoyancy change with increasing flow depth and velocities, flexural rigidities at respective plant heights should be used.

I analyzed three riparian plant species found ubiquitously within BIBE, but many other plant species are also commonly found in the riparian corridor including mesquite (*Prosopis glandulosa*), retama (*Parkinsonia aculeata*), huisache (*Acacia farnesiana*), and burro bush (*Hymenoclea monogyra*). While I quantified vegetation roughness and hydraulically modeled three plant species, the analysis was limited, and further research could expand the analysis to include additional plant species. Moreover, patches of plants mapped in the field in 2021 included mixed native and invasive plant stands but it is not yet fully understood how complex patches of flexible plants interact (Aberle and Järvelä, 2013). A broader approach that includes more field data on all species present would provide a more comprehensive understanding of vegetation-channel interactions. Furthermore, there is room to expand this research by linking the hydraulic modeling simulations with the vegetation-elevation histogram analysis to better understand inundating flows and their relationship to vegetation roughness. A series of lower discharges could be run to inundate specific species at depths near their vegetation roughness peaks and evaluate what discharges align with the highest roughness. This information would be useful to natural resource managers to evaluate what discharges result in increased sediment deposition due to high vegetation roughness. Additionally, simulations could be performed where giant cane is removed and subsequently baccharis is added in regions where it can grow, determined by the vegetation-elevation histograms.

In general, model performance could be improved by limiting the influence of the stage-discharge rating curve downstream boundary condition. The stage-discharge rating curve holds the WSE constant at the downstream boundary for all vegetation scenarios, but this is not realistic given the difference in WSE at the upstream end between scenarios. Ideally, the modeling work I performed would be used as a baseline, and different stage-discharge rating curves would be created for each scenario based on the differences in WSE at the upstream end. Alternatively, the modeled reach could be duplicated such that the length of the reach would be approximately 3 km instead of 1.5 km, and the influence of the downstream boundary condition would be negligible. For this study, reach-scale analyses were performed on the entire reach, but analyses could also be focused on the upper half of the reach to lessen the influence of the downstream boundary condition.

Total bed shear stresses are computed in SRH-2D by the Manning's equation using a friction coefficient (Lai, 2008). The model does not distinguish between bed shear stress and vegetation shear stress and thus model output is a summation of the friction throughout the water column. I hypothesized that shear stresses would increase suggesting less sediment deposition when giant cane was removed (H2). Additional work is needed to partition shear stress in a sediment transport model to analyze shear stress results between vegetation scenarios. Vegetation reduces bed shear stress due to decreased velocities from increases in hydraulic resistance (Griffin et al., 2005; Bennett et al., 2008; Manners et al., 2013). Some studies have analyzed bed shear stress in vegetated areas and found that horseshoe vortices can locally increase turbulence and bed shear stress (e.g. Yager and Schmeeckle, 2013; Flora et al., 2021). Discrepancies in the literature highlight the need for additional research to analyze the complexities between vegetation and hydraulics. In this study, higher bed shear stresses were seen in the vegetated

regions due to a higher friction coefficient. The high friction coefficient overwhelmed the velocity term in the bed shear stress calculation because although velocities were reduced where vegetation was located on the channel margins, the reduction in local velocity was not enough. Thresholds may exist at which the friction coefficient outweighs the velocity term, which could provide insight into drivers of sediment deposition and erosion.

To better understand channel and riparian ecosystem changes, detailed topographic and vegetation studies have occurred along the Rio Grande over the past decade. In Boquillas Canyon (Figure 2.2), monumented study bars have been established where spatial and temporal data exist for local topography, riparian vegetation, and hydrologic conditions. These data provide an opportunity to link modeling results to potential morphologic and sediment conveyance change over time and expand our understanding of the hydraulic effects of IRV colonization and growth, as well as the effects of removal.

2.5 Conclusions

This study quantified morphodynamic-effect traits at the plant and plot scale and modeled their effect at the reach scale on channel hydraulics over a 1.5 km reach of the Rio Grande. The high frontal area of giant cane, based on field measurements, resulted in the highest plant and plot scale vegetation roughness of the studied plant species. If the analysis was performed solely based on individual plant data, the dense growing habit of the two grasses would not have been effectively captured. Plot scale data also allowed for a reach scale analysis to better understand the hydraulic effects of specific plant species and giant cane removal.

The hydraulic model revealed that a channel filled with giant cane increased reach-averaged WSE's by approximately 30 cm at an approximately bankfull flow and slowed reach-averaged velocity. These results suggest giant cane hinders channel conveyance, allows for more sediment deposition, and contributes to channel narrowing. Removing giant cane from the model reduced reach-averaged WSE by 10 cm and increased reach-averaged velocity by 9%, a trend that likely increases conveyance and erosion and helps reverse channel narrowing. The distribution of riparian plants was mapped to geomorphic surfaces and indicates that giant cane was more commonly found at higher elevations compared to baccharis and phragmites. This raised the question as to how giant cane's geomorphic position influences treatment efforts and whether the effect of native species' geomorphic position outweighs their lower vegetation roughness. Baccharis grows abundantly within the active channel, is inundated frequently, and could be an important contributor to decreased channel capacity and channel narrowing. Phragmites had a similar morphology to giant cane, plot scale vegetation roughness, and is found predominantly on the lowest flood surface. Natural resource managers are tasked with making difficult decisions related to treating invasive plants. This study provides insight into the complexities of species-specific vegetation dynamics and geomorphic influences to help guide the future management of riparian corridors.

References

Aberle, J., & Järvelä, J. (2013). Flow resistance of emergent rigid and flexible floodplain vegetation. Journal of Hydraulic Research, 51(1), 33–45. https://doi.org/10.1080/00221686.2012.754795

Abu-Aly, T. R., Pasternack, G. B., Wyrick, J. R., Barker, R., Massa, D., & Johnson, T. (2014). Effects of LiDAR-derived, spatially distributed vegetation roughness on two-dimensional hydraulics in a gravel-cobble river at flows of 0.2 to 20 times bankfull. Geomorphology (Amsterdam, Netherlands), 206, 468–482. https://doi.org/10.1016/j.geomorph.2013.10.017

Acrement, G. J., & Schneider, V. R. (1989). Guide for Selecting Manning ' s Roughness Coefficients for Natural Channels and Flood Plains United States Geological Survey Water-supply Paper 2339. Area, 2339, 39. http://www.fhwa.dot.gov/BRIDGE/wsp2339.pdf

Baptist, M. J., Babovic, V., Rodríguez Uthurburu, J., Keijzer, M., Uittenbogaard, R. E., Mynett, A., & Verwey, A. (2007). On inducing equations for vegetation resistance. Journal of Hydraulic Research, 45(4), 435–450. https://doi.org/10.1080/00221686.2007.9521778

Bell, G.P. (1997). Ecology and management of Arundo donax,and approaches to riparian habitat restoration in southern Califor- nia. Plant Invasions: Studies from North America and Europe (ed. by JH Brock, MWade, P Pysek & D Green), pp. 103–113. Backhuys, Leiden, The Netherlands.

Bennett SJ, Wu W, Alonso CV, Wang SSY. 2008. Modeling fluvial response to in-stream woody vegetation: implications for stream corridor restoration. *Earth Surface Processes and Landforms* 33(6): 890–909. DOI: 10.1002/esp.1581

Blythe, T.L., 2018b. Running the cañons of the Rio Grande: Part 2 Boquillas Canyon, Texas and

Coahuila. M.S. Thesis MS Thesis. Utah State University, Logan, UT.

Blythe, T. L., & Schmidt, J. C. (2018). Estimating the Natural Flow Regime of Rivers With Long-Standing Development: The Northern Branch of the Rio Grande. *Water Resources Research*, *54*(2), 1212–1236. https://doi.org/10.1002/2017WR021919

Briggs, M. K., Poulos, H. M., Renfrow, J., Ochoa-Espinoza, J., Larson, D., Manning, P., Sirotnak, J., & Crawford, K. (2021). Choked out: Battling invasive giant cane along the Rio Grande/Bravo Borderlands. River Research and Applications, 37(10), 1471–1479. https://doi.org/10.1002/rra.3858

Butterfield, B. J., Grams, P. E., Durning, L. E., Hazel, J., Palmquist, E. C., Ralston, B. E., & Sankey, J. B. (2020). Associations between riparian plant morphological guilds and fluvial sediment dynamics along the regulated Colorado River in Grand Canyon. *River Research and Applications*, *36*(3), 410–421. https://doi.org/10.1002/rra.3589

Bywater-Reyes, S., Wilcox, A. C., & Diehl, R. M. (2017). Multiscale influence of woody riparian vegetation on fluvial topography quantified with ground-based and airborne lidar. *Journal of Geophysical Research: Earth Surface*, *122*(6), 1218–1235. https://doi.org/10.1002/2016JF004058

Bywater-Reyes, S., Diehl, R. M., & Wilcox, A. C. (2018). The influence of a vegetated bar on channel-bend flow dynamics. *Earth Surf. Dynam*, *6*, 487–503. https://doi.org/10.5194/esurf-6-487-2018

Bywater-Reyes, S., Diehl, R. M., Wilcox, A. C., Stella, J. C., & Kui, L. (2022). A Green New Balance: Interactions among riparian vegetation plant traits and morphodynamics in alluvial rivers. *Earth Surface Processes and Landforms*, 47(10), 2410–2436.

https://doi.org/10.1002/esp.5385

Cadol, D., Rathburn, S. L., & Cooper, D. J. (2011). *Aerial Photographic Analysis of Channel Narrowing and Vegetation Expansion in Canyon de Chelly National Monument, Arizona, USA, 1935-2004*. 1935–2004. https://doi.org/10.1002/rra.1399

Chaulagain, S., Stone, M. C., Dombroski, D., Gillihan, T., Chen, L., & Zhang, S. (2022). An investigation into remote sensing techniques and field observations to model hydraulic roughness from riparian vegetation. River Research and Applications, 38(10), 1730–1745. https://doi.org/10.1002/rra.4053

Chow, V. T. (1959). Open channel hydraulics, McGraw-Hill, New York.

Dean, D. J., & Schmidt, J. C. (2010). The role of feedback mechanisms in historic channel changes of the lower Rio Grande in the Big Bend region. *Geomorphology*. https://doi.org/10.1016/j.geomorph.2010.03.009

Diehl, R. M., Merritt, D. M., Wilcox, A. C., & Scott, M. L. (2017). Applying functional traits to processes in riparian ecosystems. *BioScience*, *67*(8), 729–743. https://doi.org/10.1093/biosci/bix080

Diehl, R. M., Wilcox, A. C., Merritt, D. M., Perkins, D. W., & Scott, J. A. (2018a). Development of an eco-geomorphic modeling framework to evaluate riparian ecosystem response to flow-regime changes. *Ecological Engineering*, *123*, 112–126. https://doi.org/10.1016/j.ecoleng.2018.08.024

Diehl, R. M., Wilcox, A. C., Merritt, D. M., Perkins, D. W., & Scott, J. A. (2018b). Supplement To: Development of an eco-geomorphic modeling framework to evaluate riparian

ecosystem response to flow-regime changes. *Ecological Engineering*.

Easlon, HM, Bloom AJ. 2014. Easy Leaf Area: Automated Digital Image Analysis for Rapid and Accurate Measurement of Leaf Area. Applications in Plant Sciences 2: 1400033.

Eckermann, T. K., Hunt, D. S., & Kinoshita, A. M. (2022). Impacts of Vegetation Removal on Urban Mediterranean Stream Hydrology and Hydraulics. *Hydrology*, *9*(10). https://doi.org/10.3390/hydrology9100170

Fathi-Maghadam, M. & Kouwen, N. (1997) Nonrigid, nonsubmerged, vege- tative roughness on floodplains. Journal of Hydraulic Engineering, 123(1), 51–57. Available from: https://doi.org/10.1061/(ASCE) 0733-9429(1997)123:1(51)

Fei, S., Phillips, J., & Shouse, M. (2014). Biogeomorphic Impacts of Invasive Species. Annual Review of Ecology, Evolution, and Systematics, 45(1), 69–87. https://doi.org/10.1146/annurev-ecolsys-120213-091928

Friedman, J. M., & Lee, V. J. (2002). Extreme floods, channel change, and riparian forests along ephemeral streams. *Ecological Monographs*, *72*(3), 409–425. https://doi.org/10.1890/0012-9615(2002)072[0409:EFCCAR]2.0.CO;2

Giessow, J., Casanova, J., Leclerc, R., MacArthur, R., Fleming, G., & Giessow, J. (2011). Arundo donax Distribution and Impact Report. http://bios.dfg.ca.gov/

Gilbert, J. T., & Wilcox, A. C. (2021). An Framework Coupling Sediment Modeling With Invasive Riparian Vegetation Dynamics. *Journal of Geophysical Research: Earth Surface*, *126*(6). https://doi.org/10.1029/2021JF006071

González, E., Sher, A. A., Anderson, R. M., Bay, R. F., Bean, D. W., Bissonnete, G. J., …

Shafroth, P. B. (2017). Vegetation response to invasive Tamarix control in southwestern U.S. rivers: A collaborative study including 416 sites. *Ecological Applications*, *27*(6), 1789–1804. https://doi.org/10.1002/eap.1566

González, E., Sher, A. A., Anderson, R. M., Bay, R. F., Bean, D. W., Bissonnete, G. J., … Tabacchi, E. (2017). Secondary invasions of noxious weeds associated with control of invasive Tamarix are frequent, idiosyncratic and persistent. *Biological Conservation*, *213*(June), 106–114. https://doi.org/10.1016/j.biocon.2017.06.043

Graf, W. L. (1978). Fluvial adjustments to the spread of tamarisk in the Colorado Plateau region. *Bulletin of the Geological Society of America*. https://doi.org/10.1130/0016-7606(1978)89<1491:FATTSO>2.0.CO;2

Griffin, Kean, J. W., Vincent, K. R., Smith, J. D., & Friedman, J. M. (2005). Modeling effects of bank friction and woody bank vegetation on channel flow and boundary shear stress in the Rio Puerco, New Mexico. Journal of Geophysical Research, 110(F4), F04023–n/a. https://doi.org/10.1029/2005JF000322

Harms, R. S., & Hiebert, R. D. (2006). Vegetation response following invasive tamarisk (Tamarix spp.) removal and implications for riparian restoration. *Restoration Ecology*, *14*(3), 461–472. https://doi.org/10.1111/j.1526-100X.2006.00154.x

Jaeger, K. L., & Wohl, E. (2011). Channel response in a semiarid stream to removal of tamarisk and Russian olive. *Water Resources Research*, *47*(2). https://doi.org/10.1029/2009WR008741

Järvelä, J. (2002). Flow resistance of flexible and stiff vegetation: A flume study with natural plants. Journal of Hydrology, 269(1–2), 44–54. https://doi.org/10.1016/S0022-

1694(02)00193-2

Järvelä, J. (2004) Determination of flow resistance caused by non- submerged woody vegetation. International Journal of River Basin Management, 2(1), 37–41. Available from: https://doi.org/10.1080/ 15715124.2004.9635222

Keller, D. L., Laub, B. G., Birdsey, P., & Dean, D. J. (2014). Effects of flooding and tamarisk removal on habitat for sensitive fish species in the San Rafael River, Utah: Implications for fish habitat enhancement and future restoration efforts. *Environmental Management*, *54*(3), 465–478. https://doi.org/10.1007/s00267-014-0318-7

Lai, Y.G., 2008. SRH-2D Version 2: Theory and User's Manual. U.S. Department of the Interior, Bureau of Reclamation, Technical Service Center, Denver, CO.

Lama, G. F. C., Crimaldi, M., Pasquino, V., Padulano, R., & Chirico, G. B. (2021). Bulk Drag Predictions of Riparian Arundo donax Stands through UAV-Acquired Multispectral Images. Water (Basel), 13(10), 1333-. https://doi.org/10.3390/w13101333

Lambert, A. M., Dudley, T. L., & Robbins, J. (2014). Nutrient enrichment and soil conditions drive productivity in the large-statured inva-sive grass Arundo donax. Aquatic Botany, 112, 16–22. https://doi.org/10.1016/j.aquabot.2013.07.004

Legleiter, C. J., Phelps, T. L., & Wohl, E. E. (2007). Geostatistical analysis of the effects of stage and roughness on reach-scale spatial patterns of velocity and turbulence intensity. *Geomorphology*, *83*(3–4), 322–345. https://doi.org/10.1016/j.geomorph.2006.02.022

Lightbody, A. F., & Nepf, H. M. (2006). Prediction of near-field shear dispersion in an emergent canopy with heterogeneous morphology. Environmental Fluid Mechanics (Dordrecht,

Netherlands : 2001), 6(5), 477–488. https://doi.org/10.1007/s10652-006-9002-7

Lightbody, A. F., Kui, L., Stella, J. C., Skorko, K. W., Bywater-Reyes, S., & Wilcox, A. C. (2019). Riparian vegetation and sediment supply regulate the morphodynamic response of an experimental stream to floods. *Frontiers in Environmental Science*, *7*(APR), 1–14. https://doi.org/10.3389/fenvs.2019.00040

Luhar, M., & Nepf, H. M. (2011). Flow-induced reconfiguration of buoyant and flexible aquatic vegetation. *Limnology and Oceanography*, *56*(6), 2003–2017. https://doi.org/10.4319/lo.2011.56.6.2003

Luhar, M., & Nepf, H. M. (2013). From the blade scale to the reach scale: A characterization of aquatic vegetative drag. *Advances in Water Resources*, *51*, 305–316. https://doi.org/10.1016/j.advwatres.2012.02.002

Manners, R. B., Schmidt, J. C., & Scott, M. L. (2014). Mechanisms of vegetation-induced channel narrowing of an unregulated canyon river: Results from a natural field-scale experiment. *Geomorphology*. https://doi.org/10.1016/j.geomorph.2013.12.033

Manners, R., Schmidt, J., & Wheaton, J. M. (2013). Multiscalar model for the determination of spatially explicit riparian vegetation roughness. *Journal of Geophysical Research: Earth Surface*, *118*(1), 65–83. https://doi.org/10.1029/2011JF002188

van Oorschot, M., Kleinhans, M. G., Geerling, G. W., Egger, G., Leuven, R. S. E. W., & Middelkoop, H. (2017). Modeling invasive alien plant species in river systems: Interaction with native ecosystem engineers and effects on hydro-morphodynamic processes. *Water Resources Research*, *53*(8), 6945–6969. https://doi.org/10.1002/2017WR020854

Mcshane, R. R., Auerbach, D. A., Friedman, J. M., Auble, G. T., Shafroth, P. B., Merigliano, M. F., … Poff, N. L. (2015). Distribution of invasive and native riparian woody plants across the western USA in relation to climate, river flow, floodplain geometry and patterns of introduction. *Ecography*, *38*(12), 1254–1265. https://doi.org/10.1111/ecog.01285

Musleh, F.A. & Cruise, J.F. (2006) Functional relationships of resistance in wide flood plains with rigid unsubmerged vegetation. Journal of Hydraulic Engineering, 132(2), 163–171. Available from: https://doi. org/10.1061/(ASCE)0733-9429(2006)132:2(163)

Nelson, J. M., Shimizu, Y., Abe, T., Asahi, K., Gamou, M., Inoue, T., … Watanabe, Y. (2016). The international river interface cooperative: Public domain flow and morphodynamics software for education and applications. *Advances in Water Resources*. https://doi.org/10.1016/j.advwatres.2015.09.017

Nikuradse, J., (1950). Laws of flow in rough pipes (1933, translation) (Nat. Advis. Comm. On Aeronautics, Tech. Mem., No. 1292). Washington, DC.

Ortiz, A. C., Ashton, A., & Nepf, H. (2013). Mean and turbulent velocity fields near rigid and flexible plants and the implications for deposition. *Journal of Geophysical Research: Earth Surface*, *118*(4), 2585–2599. https://doi.org/10.1002/2013JF002858

Pérez-Harguindeguy N, et al. 2013. New Handbook for standardized measurment of plant functional traits worldwide. Australian Journal of Botany 23:167–234.

Perignon, M. C., Tucker, G. E., Griffin, E. R., & Friedman, J. M. (2013). Effects of riparian vegetation on topographic change during a large flood event, Rio Puerco, New Mexico, USA. *Journal of Geophysical Research: Earth Surface*, *118*(3), 1193–1209. https://doi.org/10.1002/jgrf.20073

Petryk, S., and Bosmajian G., III. (1995). ‘‘Analysis of flow through vegetation.’’ J. Hydr. Div., ASCE, 101(7), 871–884.

Pollen-Bankhead, N., Simon, A., Jaeger, K., & Wohl, E. (2009). Destabilization of streambanks by removal of invasive species in Canyon de Chelly National Monument, Arizona. *Geomorphology*. https://doi.org/10.1016/j.geomorph.2008.07.004

Scott, M. L., Reynolds, L. V., Shafroth, P. B., & Spence, J. R. (2018). The role of a non-native tree in riparian vegetation expansion and channel narrowing along a dryland river. *Ecohydrology*, *11*(7), 1–17. https://doi.org/10.1002/eco.1988

Shafroth, Patrick B, Merritt, David M., Briggs, Mark K., Beauchamp, Vanessa B., Lair, Kenneth D., Scott, Michael L., Sher, A. (2013). Riparian Restoration in the Context of Tamarisk Control. In *Tamarix: A Case Study of Ecological Change in the American West* (pp. 404–425).

Shafroth, Patrick B.Brown, Curtis A., Merritt, D. M. (2010). *Saltcedar and Russian Olive Control Demonstration Act Science Assessment*.

Shafroth, P. B., Cleverly, J. R., Dudley, T. L., Taylor, J. P., Van Riper, C., Weeks, E. P., & Stuart, J. N. (2005). Control of Tamarix in the western United States: Implications for water salvage, wildlife use, and riparian restoration. *Environmental Management*, *35*(3), 231–246. https://doi.org/10.1007/s00267-004-0099-5

Sogge, M. K., Sferra, S. J., & Paxton, E. H. (2008). Tamarix as habitat for birds: Implications for riparian restoration in the Southwestern United States. *Restoration Ecology*, *16*(1), 146–154. https://doi.org/10.1111/j.1526-100X.2008.00357.x

Stone, M. C., Chen, L., McKay, S. K., Goreham, J., Acharya, K., Fischenich, C., & Sonte, A. B. (2013). Bending of submerged woody riparian vegetation as a function of hydraulic flow conditions. River Research and Applications, 29, 195–205. https://doi.org/10.1002/rra

Stover, J., Keller, E., Dudley, T., & Langendoen, E. (2018). Fluvial geomorphology, root distribution, and tensile strength of the invasive giant reed, Arundo donax and its role on stream bank stability in the Santa Clara River, Southern California. Geosciences (Basel), 8(8), 304-. https://doi.org/10.3390/geosciences8080304

Stromberg, J. C., Lite, S. J., Marler, R., Paradzick, C., Shafroth, P. B., Shorrock, D., … White, M. S. (2007). Altered stream-flow regimes and invasive plant species: The Tamarix case. *Global Ecology and Biogeography*, *16*(3), 381–393. https://doi.org/10.1111/j.1466-8238.2007.00297.x

Tooth, S., and G. C. Nanson (2000), The role of vegetation in the formation of anabranching channels in an ephemeral river, Northern plains, arid central Australia, Hydrol. Processes, 3117, 3099–3117.

Usherwood, J. R., Ennos, A. R., & Ball, D. J. (1997). Mechanical and anatomical adaptations in terrestrial and aquatic buttercups to their respective environments. In Journal of Experimental Botany (Vol. 48, Issue 312). https://academic.oup.com/jxb/article/48/7/1469/521810

Valente, J. J., McCune, K. B., Tamulonis, R. A., Neipert, E. S., & Fischer, R. A. (2019). Removal pattern mitigates negative, short-term effects of stepwise Russian olive eradication on breeding birds. *Ecosphere*. https://doi.org/10.1002/ecs2.2756

van Oorschot, M., Kleinhans, M. G., Geerling, G. W., Egger, G., Leuven, R. S. E. W., &

Middelkoop, H. (2017). Modeling invasive alien plant species in river systems: Interaction with native ecosystem engineers and effects on hydro-morphodynamic processes. *Water Resources Research*, *53*(8), 6945–6969. https://doi.org/10.1002/2017WR020854

Vargas-Luna, A., Crosato, A., & Uijttewaal, W. S. J. (2015). Effects of vegetation on flow and sediment transport: Comparative analyses and validation of predicting models. *Earth Surface Processes and Landforms*, *40*(2), 157–176. https://doi.org/10.1002/esp.3633

Vincent, Friedman, J. M., & Griffin, E. R. (2009). Erosional Consequence of Saltcedar Control. *Environmental Management* (New York), 44(2), 218–227. https://doi.org/10.1007/s00267-009-9314-8

Wang, J., Zhang, Z., & Asce, M. (2019). Evaluating Riparian Vegetation Roughness Computation Methods Integrated within HEC-RAS. https://doi.org/10.1061/(ASCE)

Whittaker, P., Wilson, C. A. M. E., & Aberle, J. (2015). An improved Cauchy number approach for predicting the drag and reconfiguration of flexible vegetation. Advances in Water Resources, 83, 28–35. https://doi.org/10.1016/j.advwatres.2015.05.005

Wieting, C., Friedman, J. M., & Rathburn, S. (2023). River channel response to invasive plant treatment across the American Southwest. *Earth Surface Processes and Landforms*, *48*(3), 569–581. https://doi.org/10.1002/esp.5503

Zhang, X., & Nepf, H. (2020). Flow-induced reconfiguration of aquatic plants, including the impact of leaf sheltering. *Limnology and Oceanography*, *65*(11), 2697–2712. https://doi.org/10.1002/lno.11542

CHAPTER 3: RIVER CHANNEL RESPONSE TO INVASIVE PLANT TREATMENT ACROSS THE AMERICAN SOUTHWEST[2]

3.1 Introduction

Invasive non-native riparian plants have altered riparian ecosystems worldwide (Griffin et al., 1989; Richardson et al., 2007; Marlin et al., 2017; Grenfell and Dube, 2022), and are often targeted for costly chemical, mechanical, and biological treatment (Zavaleta, 2000). In the Southwestern US (SW), invasive non-native plant species such as tamarisk (*Tamarix* spp.), Russian olive (*Elaeagnus angustifolia*), and giant cane (*Arundo donax*) are prolific within riparian corridors (McShane et al., 2015; Nagler et al., 2011). Artificially introduced to the SW beginning in the 19th century for river bank stabilization (Graf, 1978), invasive riparian vegetation (IRV) has spread extensively, modified wildlife habitats (Herrera & Dudley, 2003), increased fire risks, and contributed to altered stream channel morphologies (Bywater-Reyes, Wilcox, & Diehl, 2017; Diehl et al., 2017; Scott et al., 2018). Invasive plant species can be more drought tolerant than native vegetation, and may generate greater hydraulic roughness and resistance to bank failure, promoting sediment deposition, bank stabilization and channel narrowing (Pollen-Bankhead et al., 2009). River regulation and drought over the past several decades have amplified the expansion of IRV and associated channel narrowing and simplification on rivers across the SW, including the Green River (Dean & Schmidt, 2013), the Escalante River (Scott et al., 2018), Chinle Creek (Cadol et al., 2011), the Rio Puerco (Vincent et

[2]Chapter published as Wieting, C., Friedman, J. M., & Rathburn, S. (2023). River channel response to invasive plant treatment across the American Southwest. *Earth Surface Processes and Landforms*, *48*(3), 569–581. https://doi.org/10.1002/esp.5503

al., 2009), and the San Rafael River (Keller et al., 2014). IRV has been targeted for treatment in the SW as a part of environmental restoration efforts since the 1960s (Shafroth et al., 2005; González et al., 2015), with treatment efforts increasing exponentially since 1990 (Bernhardt et al., 2005). Goals of river restoration practices which remove IRV generally focus on improving wildlife habitat, or promoting native riparian plant species, (Shafroth et al., 2013; Shafroth et al., 2005). IRV treatment may also be carried out to increase river flow, but this approach may not be feasible (Hart et al., 2005). Treatment of the dominant invasive vegetation can decrease hydraulic roughness and bank stability, at least temporarily, and can lead to channel widening and increased rate of channel migration (Vincent et al., 2009; Jaeger & Wohl, 2011; Keller et al., 2014). It is unknown, however, whether this is a frequent and widespread response. IRV exerts fundamental controls on river morphodynamics through mechanical and hydraulic processes acting at the streambank (Bertoldi et al., 2014; Martínez-Fernández et al., 2018). Treatment of woody plants promotes erosion by reducing root reinforcement of banks and reducing roughness, which increases flow velocity and shear stress (Griffin et al., 2005; Pollen-Bankhead et al., 2009). Where vegetation treatment is followed by flooding, large increases in channel area and migration rate may result (Vincent et al., 2009). A more mobile channel may be seen as a return to the condition prior to arrival of IRV, and may benefit native disturbance-dependent species (Sher et al., 2002; González et al., 2018). On the other hand, increased sediment fluxes from IRV treatment may fill reservoirs, and increased channel migration rates may put inhabited or cultural areas at risk (Jaeger and Wohl, 2011) or remove valued patches of existing vegetation.

While IRV treatment within river corridors has continued to increase along with overall channel restoration efforts, the post-IRV treatment monitoring has not kept pace (Rubin et al., 2017). Restoration goals and post-eradication of IRV monitoring efforts overwhelmingly focus

on vegetation (González et al., 2017a; González et al., 2017b; Harms & Hiebert, 2006) or wildlife (Sogge et al., 2008; Valente et al., 2019) response; however, hydrological and geomorphic processes are key drivers of aquatic habitat and vegetation dynamics in riparian ecosystems (Stromberg et al., 2007). At the Escalante River, Scott et al. (2018) found that the shade-tolerant invasive shrub Russian olive grew in native Fremont cottonwood (*Populus fremontii*) understories, and modified channel morphology by trapping sediment and forming levees. Russian olive control efforts along the Escalante River have occurred for approximately ten years, but channel morphologic response to treatments is still not well understood. After Russian olive treatment along Chinle Creek in Canyon de Chelly National Monument, Arizona, Pollen-Bankhead et al. (2009) and Jaeger and Wohl (2011) found that channel widening occurred. IRV treatment may introduce significant sediment contributions to Chinle Creek, but large floods would be needed to shift channel morphology from the present meandering condition back to pre-invasion braided form. Along the Rio Puerco and San Rafael River, channel movement, channel area, and sediment supply all increased where treatment of tamarisk was followed by flooding (Vincent et al., 2009; Keller et al., 2014). These isolated studies show that treatment can lead to increased channel width and mobility in some cases, but there have been no regional studies investigating the likelihood of these channel morphologic responses or the factors promoting or resisting it.

This study focuses on three dominant introduced floodplain plant species found in the SW: tamarisk, Russian olive, and giant cane. Diverse methods to treat these species exist, including: biological, mechanical, chemical, grazing, burning, flooding, and integrated control methods (Shafroth et al., 2010). Tamarisk and Russian olive are commonly targeted using chemical, mechanical, or biological methods (Zavaleta, 2000). The tamarisk beetle (*Diorhabda* spp.) was

released in 2001 to control tamarisk and has increased plant mortality by defoliation (Pattison et al., 2011). Giant cane spreads downstream by rhizome dispersal (Gilbert & Wilcox, 2021), and plants resprout easily after mechanical cutting (Briggs et al., 2021). Therefore, commonly used treatment methods for giant cane include application of herbicide alone, as well as integrated methods of mechanical cutting or prescribed fire with follow-up herbicide application (Briggs et al., 2021).

I focus this analysis on mechanical and chemical methods of IRV treatment. Mechanical treatment includes the use of heavy machinery to remove the entire plant (whole-plant, WP), or hand/chain saws to cut the plant to its stump (CS). The CS method is commonly used to treat IRV because it can be more cost-efficient than WP (Shafroth et al., 2010). Helicopter herbicide application (HH) was included in this analysis as a chemical method to treat IRV, considering its use over large spatial extents. Biocontrol sites were not examined because the dispersal of treatment organisms makes the identification of paired treatment and untreated control sites difficult.

I tested the hypothesis that IRV treatment increases streambank erosion and channel mobility. Because response varies strongly across rivers, I investigated a number of different rivers (15 study sites on 13 rivers across 6 states). I paired each treated site with a nearby untreated site along the same river to distinguish the effect of IRV treatment from those of other local factors. I quantified channel change at a broad spatial scale using aerial imagery collected before and after IRV treatment to meet the following objectives: (i) quantify the response of river channels to IRV treatment, and (ii) determine the influence of flood magnitude on the response to IRV treatment.

3.2 Methods

3.2.1 Study Region and Reaches

The 15 study sites are located along 13 rivers across six states in the SW region: California, Arizona, Colorado, Texas, New Mexico, Utah, and (Figure 3.1). All the rivers I selected are alluvial, with predominantly sand-sized sediment comprising channel beds. Each site included a treated reach and a nearby untreated reach (Table 2.1). IRV treatment data were compiled from published literature (González et al., 2017a; Barz et al., 2009; Harms & Hiebert, 2006; Hart et al., 2005), databases of restoration organizations (RiversEdge West, the Escalante River Watershed Partnership), and through personal communication. Study reaches were located based on the following criteria: IRV abundance was strongly reduced in a clearly documented reach length large enough to affect channel dimensions (> 1 km); a nearby comparable untreated reach was present; and high-resolution, repeat aerial imagery was available. To avoid pseudo replication I chose not to inflate sample size by sampling multiple nearby sites on the same river. Untreated reaches were selected to be similar in length to treated reaches, and, where possible, were located upstream of treated reaches (Figure 3.2) to avoid transport of sediment eroded from IRV treatment into the untreated reach. Treatment was not always complete throughout the treated reach; for example, at 2 sites (Rio Grande NM, Colorado River CO), treatment occurred on only one side of the channel. At one site (Escalante River), the untreated reach contained a small amount of treatment.

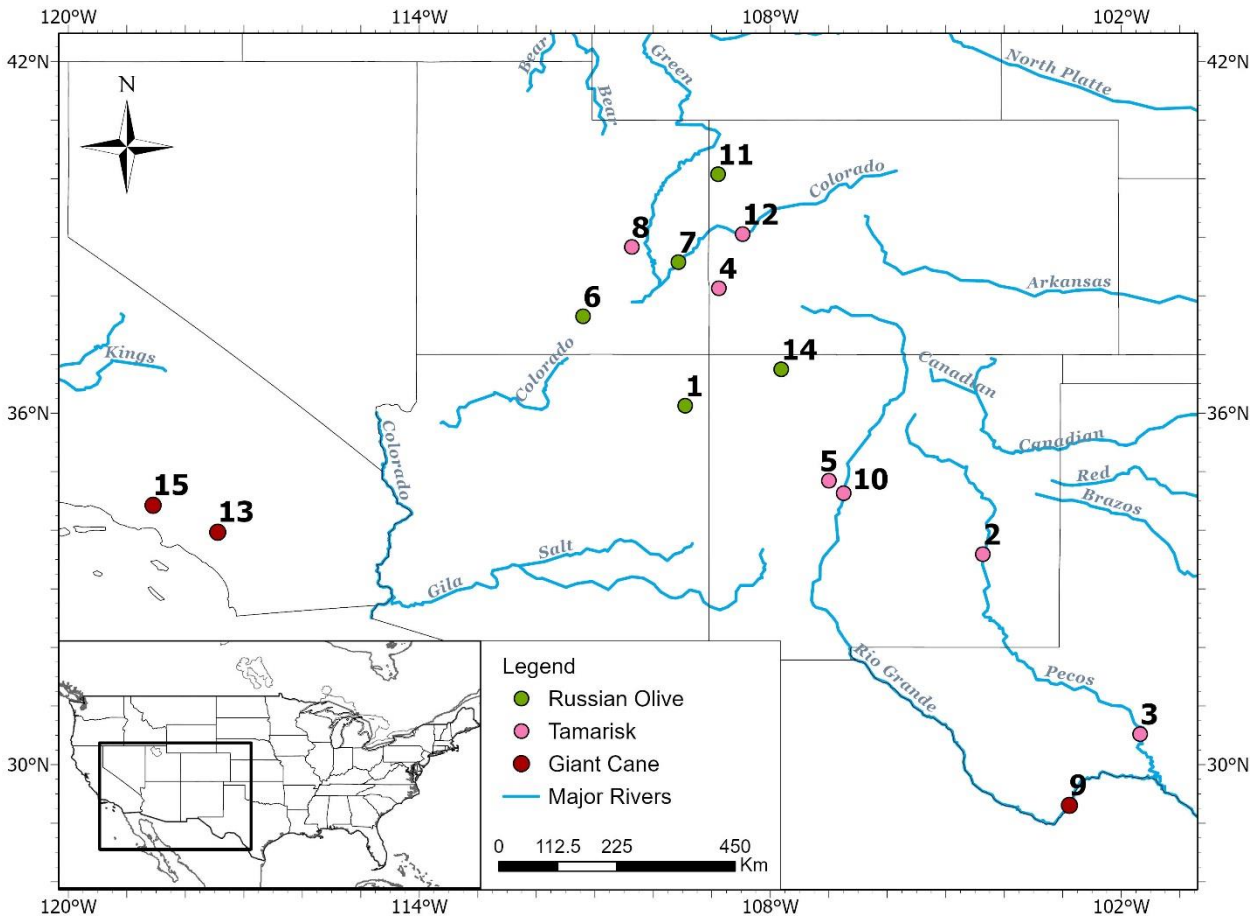

Figure 3.1. Study sites within the SW showing dominant IRV type at each site. Study site numbers correspond to the information provided in Table 2.1. The Lake Mead and Lake Powell reservoirs are not shown. River lines are sourced from the "USA major rivers" shapefile from ESRI.

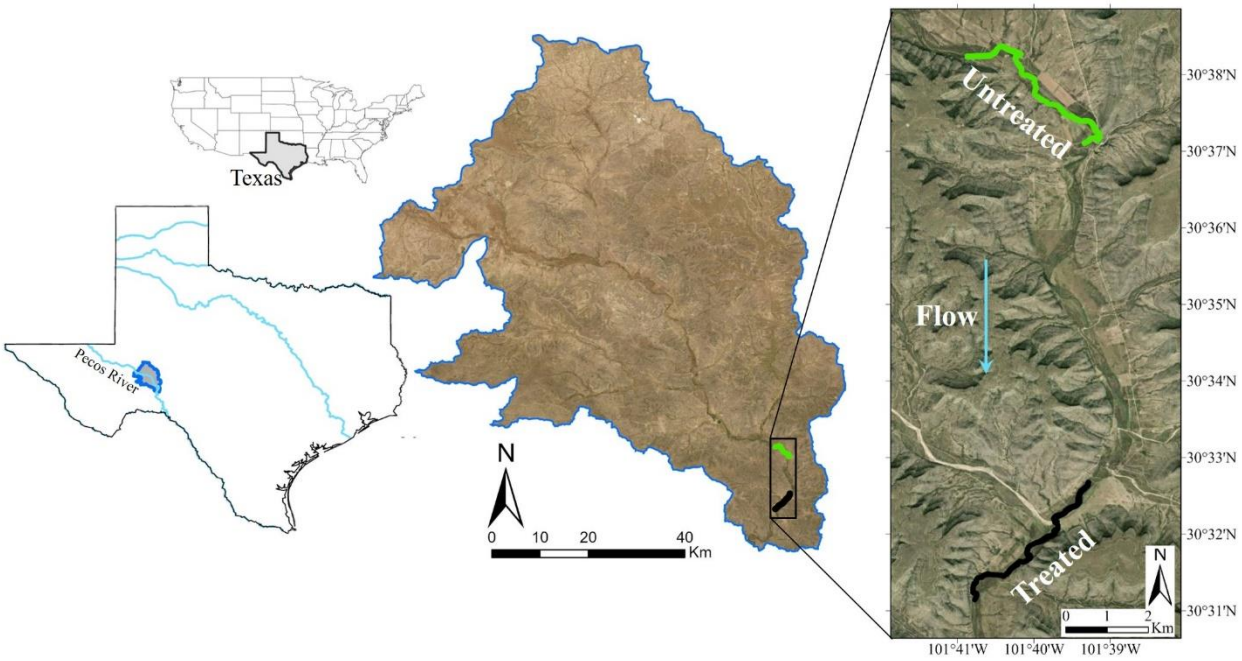

Figure 3.2. Example of untreated (green) and treated (black) reach locations along the Pecos River in Texas.

Table 3.1. Characteristics of study sites where IRV was treated along >1 km reach of river (RO = Russian olive, TAM = Tamarisk, GC: Giant cane, WP = Whole-plant, CS = Cut-stump, HH = Helicopter herbicide).

Site Number (Figure 2.1)	Site Name	Primary IRV Type	Primary Treatment Method	Treatment Timing	Channel Morphology	Channel Slope	Streamflow
1	Chinle Creek† AZ	RO, TAM	WP, CS	2005-2006	Single	0.0035	Ephemeral
2	Pecos River NM	TAM, RO	HH	2010	Single	0.0014	Perennial
3	Pecos River TX	TAM, RO	HH	1999-2004	Single	0.0011	Perennial
4	Dolores River CO	TAM	CS	2009	Single	0.0022	Ephemeral
5	Rio Puerco NM	TAM, RO	HH	2003	Single	0.0014	Ephemeral
6	Escalante River UT	RO	CS	2000-2020	Single	0.0032	Perennial
7	Mill Creek UT	RO	WP, CS	2006-2011	Single	0.0046	Perennial
8	San Rafael River UT	TAM, RO	WP	2008	Single	0.0009	Perennial
9	Rio Grande TX	GC	FC, CS	2012-2015	Single	0.0007	Perennial
10	Rio Grande NM	TAM, RO	FC, CS	2008	Single	0.0003	Perennial
11	White River CO	RO	CS	2011-2015	Single	0.0012	Perennial
12	Colorado River CO	TAM	CS	2015	Single	0.0020	Perennial
13	Santa Ana River CA	GC	WP	2008	Multithread	0.0034	Perennial
14	San Juan River NM	RO	CS	2013	Single	0.0019	Perennial
15	Santa Clara River CA	GC	CS	2018-current	Multithread	0.0039	Perennial

† There are four sites along Chinle Creek. This table displays information combining data from all four sites.

Table 3.2. Peak stream discharge information obtained from USGS stream gaging stations near study sites. Unit stream power was calculated using the peak discharge, the channel slope (Table 2.1), and the pre-treated average channel width.

Site Name	Nearest USGS Stream gage Station #	Year of Peak Discharge	Peak Discharge (m^3/s) †	Unit Stream Power, Treated (W/m^2)	Unit Stream Power, Untreated (W/m^2)	Ratio of Peak Discharge to Q2‡
Chinle Creek AZ	09379025	2006	137	850.34	1211	NA§
Pecos River NM	08386000	2013	186	65.57	41.96	2.23
Pecos River TX	08447000	2000	58	23.07	22.02	13.46
Dolores River CO	09168730	2017	103	143.98	142.68	2.01
Rio Puerco NM	08353000	2013	255	249.77	404.29	14.96
Escalante River UT	09337500	2019	72	196.86	161.45	1.95
Mill Creek UT	09185100	2010	33	225.32	228.83	8.06
San Rafael River UT	09328500	2011	69	51.58	44.55	2.16
Rio Grande TX	08375300	2018	433	79.79	72.30	1.53
Rio Grande NM	08331160	2010	159	5.52	3.24	1.43
White River CO	09306500	2011	146	41.56	41.62	2.10
Colorado River CO	09106150	2019	657	133.02	129.92	1.36
Santa Ana River CA	11066460	2010	1390	1095.19	974.77	6.55
San Juan River NM	09355500	2019	144	52.70	66.33	2.54
Santa Clara River CA	11109000	2019	212	203.23	80	3.21

† Peak discharge refers to the largest flood between the timing of pre- and post-treatment aerial imagery.

‡ Q2 refers to the two-year recurrence interval flood, calculated using the Weibull method for flood frequency estimates from peak stream flow data at the nearest USGS gaging station.

§ Ratio was not calculated due to insufficient stream gaging data.

3.2.2 Aerial imagery collection

Treated and untreated reaches were compared before and after treatment using repeat aerial imagery to assess long-term (~11 year average, Table 3.3) channel change due to treatment on a regional scale across the SW. Imagery was obtained through the USGS Earth Explorer and consisted of high-resolution orthoimagery (HRO), imagery from the National Agriculture Imagery Program (NAIP), and multispectral aerial imagery (MAI). Imagery collected nearest to the year prior to treatment efforts was used to delineate a pre-treated channel, and the most recent imagery that was available for a location was used to delineate the post-treated channel (Table 3.3). Imagery resolution ranged from 0.2 m to 1 m (Table 3.3). Although all imagery obtained was georeferenced, georeferencing errors due to image warping (Fryer & Brown, 1986), issues with georeferenced control points (Hughes et al., 2006; Mount et al., 2003), or image quality may cause uncertainty in channel measurements (Donovan et al., 2019).

Table 3.3. Aerial imagery information used in the analysis of change metrics including imagery source, spatial resolution, and the year the imagery was collected (HRO = High-resolution Orthoimagery, NAPP = National Aerial Photography Program, NAIP = National Agriculture Imagery Program, MAI = Multispectral Aerial Imagery).

Site Name	***Imagery Year***		***Aerial Imagery Spatial Resolution and Source***	
	Pre-treated	***Post-treated***	***Pre-treated***	***Post-treated***
Chinle Creek AZ	2005	2019	HRO – 1 m	NAIP – 1 m
Pecos River NM	2009	2020	NAIP – 1 m	NAIP – 0.6 m
Pecos River TX	1996	2019	NAPP – 1 m	NAIP – 0.6 m
Dolores River CO	2009	2019	NAIP – 1 m	NAIP – 0.6 m
Rio Puerco NM	2005	2020	HRO – 1 m	NAIP – 0.6 m
Escalante River UT	2009	2018	NAIP – 1 m	NAIP – 0.6 m
Mill Creek UT	2006	2018	NAIP – 1 m	NAIP – 0.6 m
San Rafael River UT	2006	2018	NAIP – 1 m	NAIP – 1m
Rio Grande TX	2012	2019	MAI – 0.2 m†	NAIP – 0.6 m
Rio Grande NM	2006	2020	HRO – 1 m	NAIP – 0.6 m
White River CO	2009	2019	NAIP – 1 m	NAIP – 0.6 m
Santa Ana River CA	2008	2020	HRO – 0.5 ft	NAIP – 1 m
Colorado River CO	2013	2020	NAIP – 1 m	NAIP – 0.6 m
San Juan River NM	2011	2020	NAIP – 1 m	NAIP – 0.6 m
Santa Clara River CA	2018	2020	NAIP – 0.6 m	NAIP – 0.6 m

† Obtained from Bedford et al. (2020).

3.2.3 Change metrics

I imported aerial imagery into a geographic information system (ArcGIS Pro, version 2.6.0) to digitize stream channel boundaries at the active-channel shelf level (Osterkamp & Hedman, 1982), a surface indicated by the lowest occurrence of established perennial vegetation. The active channel shelf level, which is generally lower than the bankfull level (Osterkamp & Hedman, 1982) has proved to be useful for channel delineation in the western United States (Miller & Friedman, 2009; Schook et al., 2017) because it responds quickly (within a few years) to changes in flow and because the lower limit of perennial vegetation is easily observed in aerial

imagery. Examples of active channel shelf delineation at the untreated and treated reaches of the Pecos River NM site can be found in Figure B1 in Appendix B.

Because channel change in response to IRV treatment involves multiple fluvial processes, I evaluated four different metrics of channel response: floodplain destruction, floodplain formation, change in channel width (width difference), and centerline migration. Reaches varied in length, and so all calculations of change were normalized by reach length and expressed in units of meters of change in channel or floodplain width or centerline location. Using ArcGIS Pro, active-channel polygons were delineated for pre- and post-treatment channel reaches (Figure 3.3). Channel area ($A_{channel}$) values were calculated from channel polygons for pre- and post-treated channels (Table 3.4). Channel centerlines were generated to examine migration using the polygon to centerline tool in ArcGIS Pro, with occasional manual adjustments to correct for in-channel features such as mid-channel bars and vegetated islands. If multiple channels were present, the dominant channel branch was chosen for the channel centerline. Centerline length ($L_{channel}$) was noted for pre- and post-treated channel polygons, and average channel width ($w_{channel}$) was calculated from channel area divided by channel length ($w_{channel} = A_{channel}/L_{channel}$; Cadol et al., 2011). The $w_{channel}$ variable allowed for normalization of channel area and comparison across the various sizes of rivers included in the study. Channel narrowing or widening following treatment was determined from the difference between post- to pre-treated channel width ($w_{post} - w_{pre}$). To quantify floodplain destruction and formation in treated and untreated reaches, pre- and post-treated active-channel polygons were overlain using the symmetrical difference overlay tool within ArcGIS Pro (Figure 3.3), which differentiates polygon areas that represent conversion from floodplain to channel and channel to floodplain. Following Miller and Friedman (2009), floodplain destruction is defined as conversion of

floodplain to channel, and floodplain formation is defined as conversion of channel to floodplain. In order to compare rivers of various sizes within this study, converted areas were normalized by pre-treated channel centerline lengths, and floodplain destruction and formation were reported as average widths. Once pre- and post-treated centerlines were generated for a treated reach, the feature to polygon tool in ArcGIS Pro was used to create a polygon between the centerlines ($A_{migration}$). Again, to normalize this measurement, the polygon area was divided by the length of the centerline for $A_{migration}$ ($w_{migration} = A_{migration}/L_{migration;}$ Table 3.4).

Uncertainty in channel delineations arose from the presence of dense or overhanging vegetation, seasonal differences of imagery showing differing vegetation canopies, shadows along the river bank, user inconsistency, and the scale and resolution of the image during delineation (Donovan et al., 2019). The consistent methodology used for delineating channels errs on the conservative side of quantifying channel and floodplain change, such that results represent a minimum of change. Manual channel delineation was used to analyze channel change opposed to existing automated methods because automated methods are generally less accurate, use water classification as an input, and vary by which algorithm is used (Donovan et al., 2019; Pavelsky & Smith, 2008; Rowland et al., 2016).

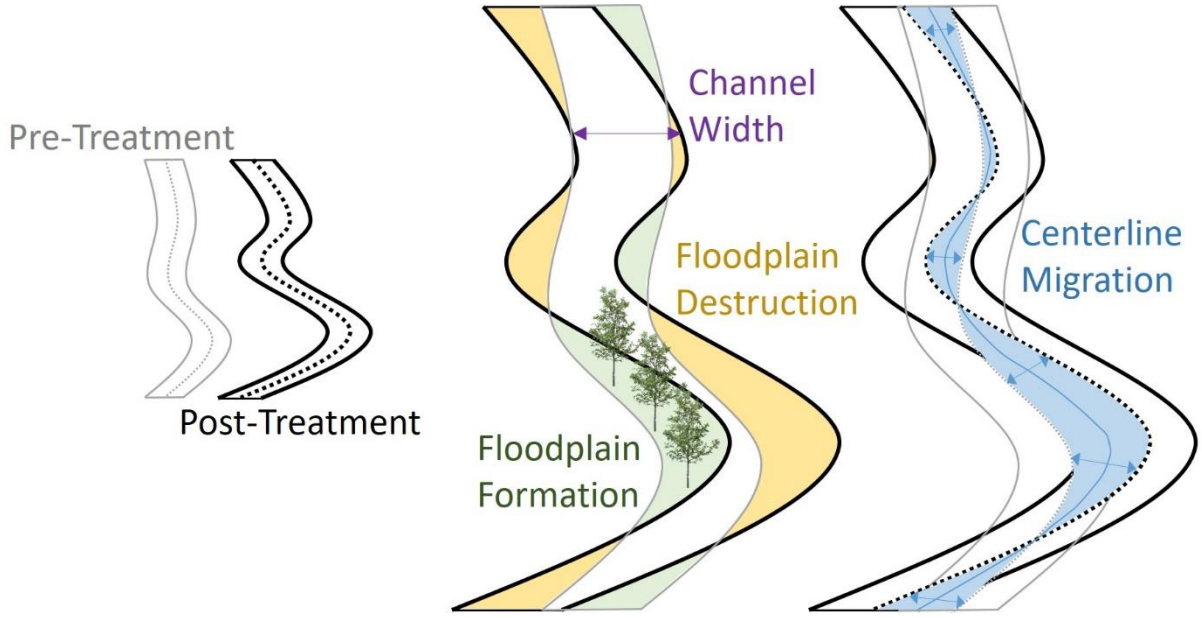

Figure 3.3. Conceptual diagram of change metrics measured and calculated using ArcGIS Pro. Yellow and green polygons are generated using the symmetrical-difference tool in ArcGIS Pro by overlaying pre- and post-treated polygons to quantify floodplain destruction and floodplain formation in treated and untreated reaches. Blue polygons are generated using the feature-to-polygon tool in ArcGIS Pro and sum the area between the pre- and post-treatment channel centerlines to quantify centerline migration. Channel width is measured by dividing channel area by channel length.

Table 3.4. Summary of change metrics and calculation methods using ArcGIS Pro. Each of the metrics was calculated using pre- and post-treated imagery in the treated and untreated reaches. To calculate the four change metrics, channel area, length, and width were first calculated from the delineated channel polygon. The units of all metrics are meters of change in channel or floodplain width or centerline location.

Channel Metric	***Index Calculation***	***Process to create metric***
Floodplain destruction	$\frac{Floodplain\ to\ Channel\ Conversion}{Pre-treated\ Channel\ Centerline\ Length}$	Overlay pre- and post-treatment channel polygons, calculate sum of area converted from floodplain to channel and divide by centerline length.
Floodplain formation	$\frac{Channel\ to\ Floodplain\ Conversion}{Pre-treated\ Channel\ Centerline\ Length}$	Overlay pre- and post-treatment channel polygons, calculate sum of areas converted from channel to floodplain and divide by centerline length.
Width difference	$\left(\frac{Channel\ Area}{Channel\ Length}\right)_{post} - \left(\frac{Channel\ Area}{Channel\ Length}\right)_{pre}$	Subtract pre-treatment average channel width (channel area divided by length) from post-treatment average channel width.
Centerline migration	$w_{migration} = \frac{A_{migration}}{L_{migration}}$	Create a polygon between pre- and post-treatment centerlines, then create a centerline of this polygon. Divide the polygon area by length of centerline.

3.2.4 Statistical and hydrologic analyses

In a paired design (n = 15 treated/untreated pairs), I analyzed the effect of IRV treatment on floodplain destruction, floodplain formation, width difference, and channel centerline migration using the Wilcoxon signed rank test (Wilcoxon). This test was selected instead of the traditional paired t-test because the effects data were not normally distributed (Rey & Neuhauser, 2014). The significance threshold for Wilcoxon tests was set at p=0.05.

To explore river channel change with respect to flood disturbance (objective ii), I estimated the highest instantaneous unit stream power for each site between the dates of the pre- and post-treated imagery. I used the peak flood under the assumption that the most geomorphic change is associated with this large flood (Tooth, 2013). I acquired instantaneous annual peak streamflow data from the USGS for the stream gaging station that best represented each treatment site (Table 3.2). I found the highest flow peak in the years between the pre- and post-treated imagery (Tables 3.2 and 3.3). Four simple linear regressions were run on each change metric using log of unit stream power as the predictor variable (Table 3.6). Regression models used all treated and untreated data combined.

Unit stream power was calculated to evaluate the energy available for geomorphic change across sites (Merritt & Wohl, 2003):

$$\omega = \gamma Q s / \mathrm{w}_{\mathrm{pre}} \quad \text{(Eq. 3.1)}$$

where ω is the unit stream power (W/m^2), γ is the unit weight of water (9800 N/m^3), Q is peak discharge (m^3/s), s is the channel slope (m/m) approximated using USGS topographic maps within ArcGIS Pro, and w_{pre} is the pre-treatment channel width (m).

3.3 Results

Treatment of IRV significantly increased floodplain destruction ($p < 0.001$) and channel width difference ($p = 0.003$), but not floodplain formation ($p = 0.934$) or centerline migration ($p = 0.059$) (Table 3.5). Treated reaches had higher floodplain destruction than untreated reaches at 14 of 15 sites (Figure 3.4A), and the median ratio of floodplain destruction at treated vs. untreated reaches was 1.90 (Figures 3.4 and 3.5); in other words, IRV treatment nearly doubled

floodplain destruction. Similarly, treated reaches widened more (or narrowed less) than untreated reaches at 12 of 15 sites, and the median difference of channel width change treated to untreated reaches was 5.43 (Figures 3.4C and 3.5). In contrast, the median ratio of floodplain formation for treated to untreated reaches was 1.08, indicating no overall effect of IRV treatment on this metric. The median ratio of migration was 1.69 and ranged from 0.12 (Rio Grande NM site) to 21.81 (Rio Puerco site) (Figure 3.5). I did not detect consistent differences among treatment methods, in part because of the small sample size. Linear models indicate significant relationships between stream power and floodplain destruction (p=0.048) and width difference (p=0.013, Table 3.6).

Table 3.5. Comparison of untreated and treated reaches using the Wilcoxon Signed Rank Test. A low test statistic, W, indicates a strong effect of the change metric variable.

Change Metric	***n***	***Test Statistic, W***	***p value***
Floodplain destruction	15	2	<0.001*
Floodplain formation	15	58	0.934
Width difference	15	10	0.003*
Centerline migration	14†	47	0.059

† The centerline for the untreated reach at the Santa Clara site was not mappable due to a multithreaded channel system, so the Santa Clara site was not considered in this statistical test.

*Significant differences at the 0.05 level.

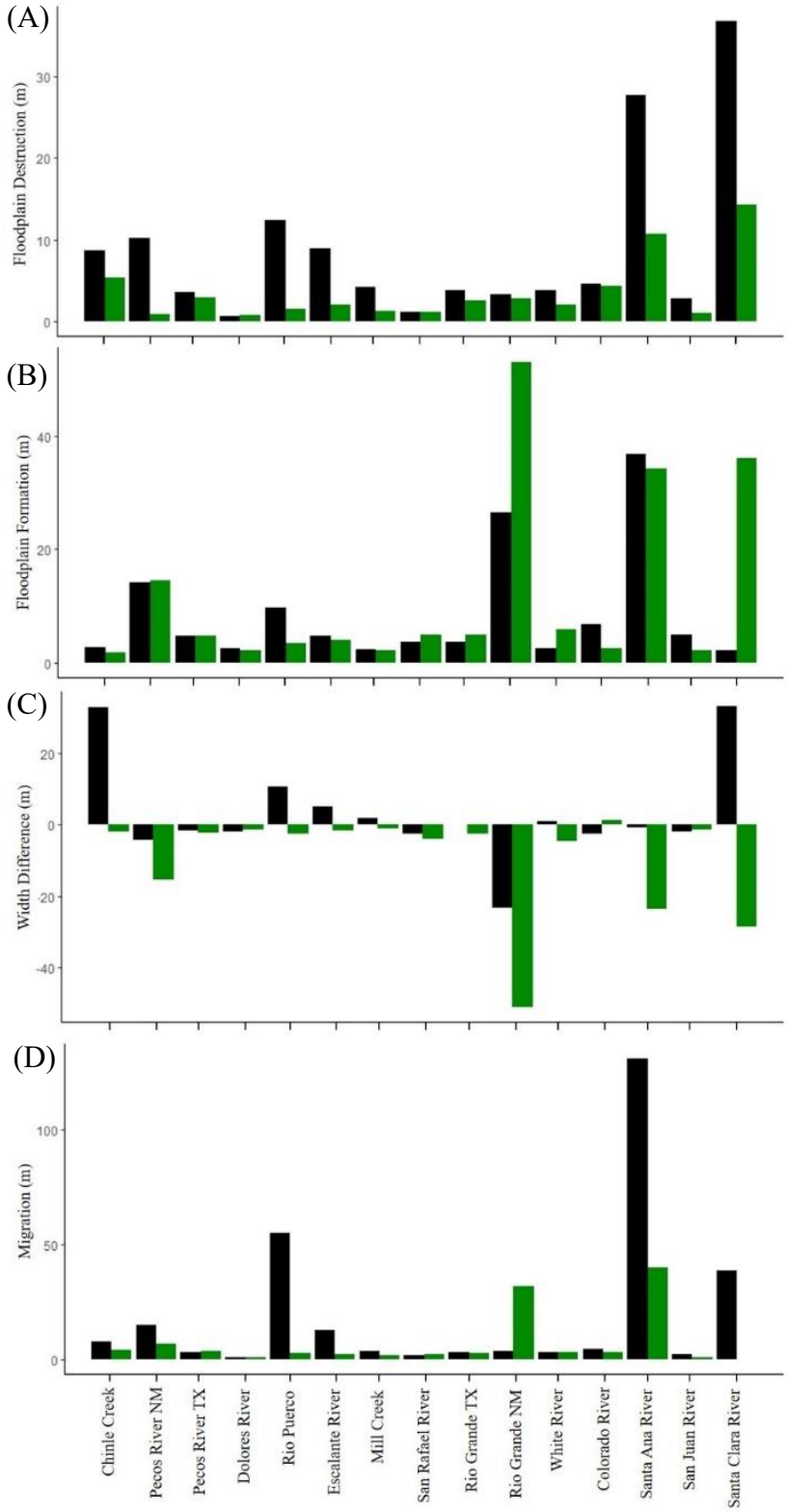

Figure 3.4. Floodplain destruction (A), floodplain formation (B), width difference (C), and migration (D) for treated (black) and untreated (green) reaches by study site.

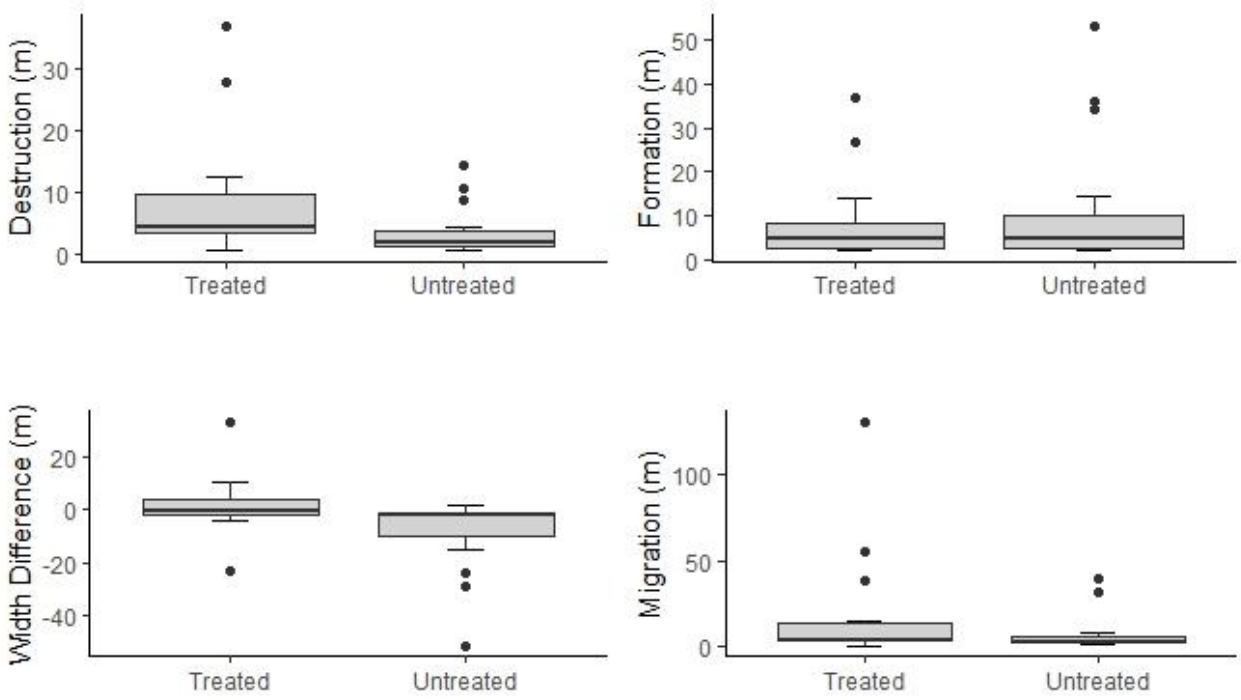

Figure 3.5. Boxplots showing the effect of treatment through floodplain destruction, formation, width difference, and migration change metrics. Boxes represent the interquartile range (IQR) between the first and third quartiles, thick horizontal line represents the median, horizontal lines represent minimum and maximum values, and individual points represent extreme values that are greater than 1.5*IQR.

Table 3.6. Linear model results for change metrics using stream power as the predictor variable. Stream power and change metrics were log transformed to meet model assumptions.

	Predictor variable: Stream power		
Change Metric	***Estimate***	***Std. Error***	***p value***
Floodplain destruction	0.272	0.132	0.048*
Floodplain formation	-0.187	0.129	0.153
Width difference	0.107	0.040	0.013*
Centerline migration	0.206	0.165	0.224

*Significant differences at the 0.05 level.

3.4 Discussion

This study quantified river channel response to IRV treatment at the decadal scale using change metrics of floodplain destruction, floodplain formation, channel width difference, and channel migration. I found a strong effect of IRV treatment on floodplain destruction reflecting the well-known observation that reducing the vegetation promotes bank erosion (Millar, 2000; Griffin et al., 2005; Pollen-Bankhead et al., 2009; Vincent et al., 2009). The observed increase in floodplain destruction at 14 of the 15 sites following IRV treatment occurred in spite of considerable variation among rivers in slope, flow and vegetation. Treatment of IRV almost doubled the amount of floodplain destruction, with a median ratio of 1.90 for treated to untreated reaches (Figure 3.5). This result supports the hypothesis that IRV treatment increases channel dynamism, partially reversing the trend of decreased width and migration rate associated with the earlier establishment of the IRV (e.g. Cadol et al., 2011; Dean & Schmidt, 2011; Manners et al., 2014; Scott et al., 2018).

On the other hand, the effect of IRV treatment on floodplain formation was complex and flow dependent, resulting in no significant relation. Because width and centerline migration integrate floodplain formation and floodplain destruction, the effect of IRV treatment on these metrics was less consistent than that on floodplain destruction. These results support the argument that resolving observations of channel change into separate estimates of floodplain destruction and formation provides insight into the underlying fluvial processes (Miller & Friedman, 2009; Dean et al., 2011; González et al., 2018).

Floodplain formation did not differ significantly between treated and untreated reaches ($p = 0.934$, Table 3.5), and the median ratio for treated to untreated reaches was close to 1.0 (Figures 3.4 and 3.5). The relationship between stream power and formation was not statistically

significant (Table 3.6). The processes driving formation appear to vary depending on stream flow and site-specific conditions. Formation can result from decreased stream flows and subsequent channel narrowing, or conversely, increased stream flows and changes in channel configuration through lateral migration. At sites where stream powers were low, vegetation became established in the channel resulting in large floodplain formation and decreased width (Figure 3.4). Treatment of IRV slowed this process. For example, in the absence of large floods, the Rio Grande NM site experienced widespread channel narrowing and floodplain formation in the untreated reach and a smaller amount of floodplain formation in the treated reach (Figure 3.4). Other studies have shown increased floodplain formation due to establishment of vegetation in the channel at low flows (Miller and Friedman, 2009; Dean et al., 2011), often in association with IRV expansion (Manners et al., 2014; Scott et al., 2018), and many rivers across the SW are following a similar trajectory to the Rio Grande NM site. In contrast, large flows promoted channel migration including floodplain formation, and this process was promoted by IRV treatment (Figure 3.4). For example, after treatment of giant cane in 2008, the highest peak flood on the Santa Ana River was recorded in 2010. The average channel width between pre- and post-treatment of the Santa Ana River only changed by 0.8 meters; however, the channel migrated an average of 113 meters (Figure 3.4). Increased floodplain destruction, formation, and meander cutoffs occurred in the treated reach, while banks remained stabilized by bank vegetation in the untreated reach. Over time, vegetation expansion and the lack of large-magnitude floods narrowed the channel in the untreated reach from approximately 47 meters to 24 meters, highlighting the importance of biogeomorphic feedbacks in channel response (Dean & Topping, 2019).

Because changes in channel width integrate floodplain formation and floodplain destruction, the effect of IRV treatment on width was not as strong as the effect on floodplain destruction. IRV treatment led to significantly wider channels ($p=0.003$), but this effect was not as strong or consistent as the effect on floodplain destruction. There was an overall weak positive effect of stream power on width difference for treated and untreated reaches (Table 3.6). Higher stream powers are generally correlated with increases in channel width (Schumm & Lichty, 1963), but the presence of vegetation in the untreated reaches limits channel widening by increasing bank stability. Moreover, pre-treated minus post-treated channel width differences were mostly negative in the untreated reaches, suggesting that processes such as vegetation establishment on in-channel deposits, and the hydrological and mechanical effects of plants are contributing to increased bank stability and channel narrowing.

More centerline migration appeared to occur in the treated reaches compared to untreated (median ratio of 1.69, Figure 3.4), but this effect was not statistically significant (Table 3.5). Increasing channel migration following IRV treatment was expected because when vegetation is treated, the additional strength provided by roots decreases, leaving banks unstable and prone to erosion (Pollen-Bankhead et al., 2009; Vincent et al., 2009). On the other hand, narrowing of many channels in the absence of high flows resulted in centerline migration without much floodplain destruction, especially in untreated channels.

The power of the largest flow in the study period was correlated with both floodplain destruction and channel width (Table 3.6), illustrating the central influence of flooding on bank erosion. Therefore, the increased erosion resulting from IRV treatment is likely to be greater where the power of subsequent flows is also high. The importance of the largest flow is consistent with other studies showing the dominance of infrequent floods in semiarid and arid

regions, where interannual variation in peak flows is high, and the geomorphic effects of large floods are relatively long-lived (Wolman and Gerson, 1978; Miller and Friedman, 2009; Merigliano et al., 2013).

The threshold for river channel change could differ for sites where giant cane is treated. Compared to tamarisk and Russian olive, giant cane has a lower root tensile strength, but a denser root system at shallower depths, influencing the type of bank failure that may occur (Stover et al., 2018). More specifically, during moderate to high flows, banks occupied by giant cane can fail by undercutting and slumping (Stover et al., 2018). Therefore, more change through lateral instability may be expected where channels are lined with giant cane, depending on the height of the streambank, bank sediment composition, and other local factors. I did not observe this effect in our dataset, most likely due to small sample size.

IRV treatment projects that use techniques such as the WP method target both the aboveground and belowground plant biomass, and cause a high level of disturbance (Shafroth et al., 2010). I suspect that in comparing treatment methods, increased channel change will result from more disruptive treatment methods (Jaeger & Wohl, 2011). However, the data in this study were not sufficient to test the relationships between IRV type, treatment method, and river channel response. Additional information on site-specific conditions at study sites and study reach replicates are needed to further evaluate these relationships. Furthermore, this study correlated change metrics to peak unit stream power, which overlooks other components of the flow regime, antecedent channel conditions, and geologic floodplain constraint, all of which may have a strong influence on channel change.

3.5 Management Implications

This study shows that IRV treatment causes a large and consistent increase in erosion across a broad range of rivers. In river restoration, increased erosion following IRV treatment is a benefit in some cases (Pollen-Bankhead et al., 2009) and a cost in others (Barz et al., 2009; Vincent et al., 2009; Jaeger & Wohl, 2011; Gilbert & Wilcox, 2021); therefore, IRV treatment projects would benefit from a geomorphic restoration goal that answers the question, "How much of an increase in channel activity is desired?". Setting this goal is based on consideration of desired process changes, downstream threats, and susceptibility of the system to change (Figure 3.6). Desired process changes may be explicit; for example, land managers may desire a return to a more dynamic channel that characterized the system prior to arrival of the IRV. In addition, desired process changes are often implicit in the list of species the practitioner is interested in promoting or impeding. For example, many native plant species (e.g. willow) are dependent upon physical disturbance and channel change. On the other hand, some invasive species (e.g. tamarisk) are also favored by channel change, while others are not (e.g. Russian olive; Katz and Shafroth, 2003). Downstream threats include the existence of people, infrastructure, or populations of vegetation in need of protection from disturbance on the floodplain downstream of the IRV treatment site. Susceptibility to geomorphic change is a function of hydrologic regime and channel characteristics. Hydrologic characteristics suggesting high susceptibility to geomorphic change include historic occurrence of large floods, stream gage records of high peak flows and lack of flow regulation. Channel characteristics suggesting high susceptibility to geomorphic change include steep gradient, absence of particles coarser than gravel in the channel boundary, lack of channel confinement, and a history of arroyo activity or major channel change in the watershed.

If the geomorphic restoration goal is to maximize channel dynamism, consider removing IRV immediately before the flood season, combining treatment with water releases where possible, or not revegetating, and consider using whole-plant treatment methods that have a high likelihood of removing the target plant and involve considerable sediment disturbance (Figure 3.6). I expect more floodplain destruction to occur in treated reaches where floods quickly follow treatment. Sites with longer lag times between treatment and a large flood will likely experience spontaneous streambank revegetation, which limits channel and floodplain response. Revegetation raises the stream power threshold needed to achieve change, as banks are once again stabilized by root systems increasing bank strength. On the other hand, if the geomorphic restoration goal is to minimize channel dynamism, plant new vegetation soon after IRV treatment, minimize soil disturbance by favoring less invasive control methods such as CS, protect non-target vegetation, concentrate treatment in the uplands leaving vegetation intact adjacent to the channel, and carry out treatment in stages to help reduce erosion susceptibility (Vincent et al., 2009).

Treatment of a dominant species over a large area can be expected to have major fluvial geomorphic consequences. Therefore, large-scale IRV treatment programs should be evaluated for possible effects of erosion on public safety. For example, tamarisk was introduced to the southwest to control erosion, and its spread has coincided with a decrease in erosion. Widespread herbicide application to remove tamarisk will also affect non-target vegetation, potentially resulting in rejuvenation of arroyos and widespread erosion. Biological control by the tamarisk beetle (*Diorhabda* species) involves an even larger potential area, although it is better targeted to tamarisk and causes patchy mortality. The loss of above and belowground biomass that results from the tamarisk beetle (Bean and Dudley, 2018) could influence physical processes associated

with hydraulics and sediment transport, affecting channel morphology. Therefore, there is a need for coarse-scale monitoring of the fluvial geomorphic effects of spread of the tamarisk beetle, possibly using repeat LiDAR in undammed basins with a history of arroyo erosion (Vincent et al., 2009).

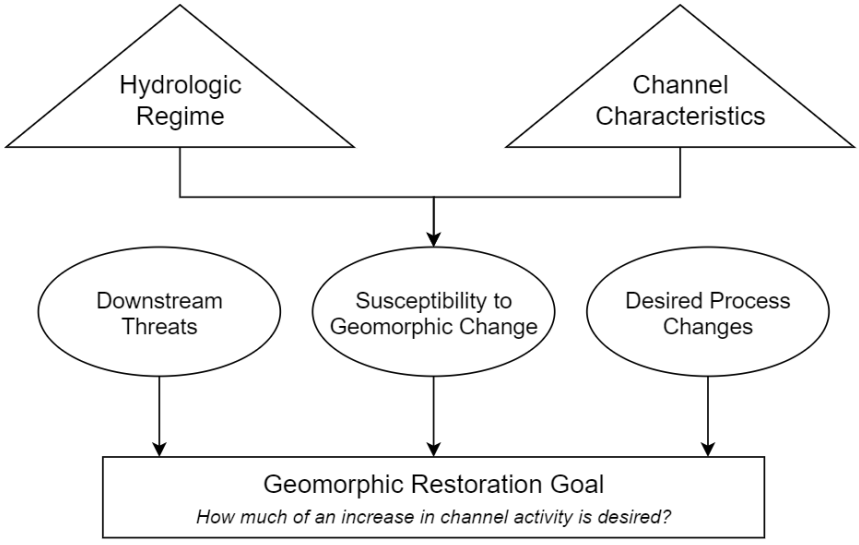

Figure 3.6. Determining a geomorphic restoration goal: How much of an increase in channel activity is desired when IRV is removed? This determination is based on consideration of desired process changes, downstream threats, and susceptibility of the system to change. Susceptibility to change is a function of the hydrologic regime and channel characteristics. For example, if threats and susceptibility to geomorphic change are both high and there is not an interest in promoting the occurrence of disturbance-dependent native vegetation, then the practitioner may choose to minimize any increase in channel activity resulting from IRV treatment using techniques described in the text.

Refining our understanding of the geomorphic effects of IRV treatment requires more data on decadal-scale geomorphic response. Long-term monitoring of channel geometry as illustrated in this study is inexpensive and would help to provide the needed information. In addition, practitioners should consider designating an untreated reach to evaluate treatment geomorphic effectiveness, as long as this does not pose an unacceptable reinvasion risk. Lastly, I

recommend increased availability of treatment data to promote analysis of channel and floodplain response to treatment.

3.6 Conclusions

I investigated channel morphologic change associated with IRV treatment at 15 sites along 13 rivers across the American Southwest using repeat aerial imagery over ~10 years. I paired treated and untreated channel reaches and found that 14 of the 15 sites analyzed showed higher floodplain destruction at the treated reaches compared to untreated reaches. IRV treatment increased the rate of floodplain destruction by almost a factor of 2. Floodplain destruction also increased with the stream power of the largest flow during the study period. Resolving observation of channel change into separate measures of floodplain destruction and formation provided more information on underlying process than measurements of channel width and centerline migration rate. I suggest a management framework to assist restoration practitioners in determining how much of an increase in channel activity is desired when IRV is removed based on consideration of desired process changes, downstream threats, and susceptibility of the system to change.

References

Barz, D., Watson, R. P., Kanney, J. F., Roberts, J. D., & Groeneveld, D. P. (2009). Cost/benefit considerations for recent saltcedar control, middle pecos river, New Mexico. *Environmental Management*, *43*(2), 282–298. https://doi.org/10.1007/s00267-008-9156-9

Bedford, A. F., Durning, L. E., Dean, D. J., & Sankey, J. B. (2020). Rio Grande 2012 Vegetation and Water Classification Data in the Big Bend Region. https://doi.org/https://doi.org/10.5066/P9MW5KZB

Bernhardt, E. S., Palmer, M. A., Allan, J. D., Alexander, G., Barnas, K., Brooks, S., … Sudduth, O. (2005). Synthesizing U.S. river restoration efforts. *Science*, *308*(5722), 636–637. https://doi.org/10.1126/science.1109769

Bertoldi W., Siviglia A., Tettamanti S., et al. (2014) Modeling vegetation controls on fluvial morphological trajectories. Geophysical Research Letters 41: 7167–7175.

Briggs, M. K., Poulos, H. M., Renfrow, J., Ochoa-Espinoza, J., Larson, D., Manning, P., … Crawford, K. (2021). *Choked out: Battling invasive giant cane along the Rio Grande/ Bravo Borderlands*. https://doi.org/10.1002/rra.3858

Bywater-Reyes, S., Wilcox, A. C., & Diehl, R. M. (2017). Multiscale influence of woody riparian vegetation on fluvial topography quantified with ground-based and airborne lidar. *Journal of Geophysical Research: Earth Surface*, *122*(6), 1218–1235. https://doi.org/10.1002/2016JF004058

Cadol, D., Rathburn, S. L., & Cooper, D. J. (2011). *Aerial Photographic Analysis of Channel Narrowing and Vegetation Expansion in Canyon de Chelly National Monument, Arizona,*

USA, 1935-2004. 1935–2004. https://doi.org/10.1002/rra.1399

Dean, D. J., Scott, M. L., Shafroth, P. B., & Schmidt, J. C. (2011). Stratigraphic, sedimentologic, and dendrogeomorphic analyses of rapid floodplain formation along the Rio Grande in Big Bend National Park, Texas. *Bulletin of the Geological Society of America*, *123*(9–10), 1908–1925. https://doi.org/10.1130/B30379.1

Dean, David J., & Schmidt, J. C. (2011). The role of feedback mechanisms in historic channel changes of the lower Rio Grande in the Big Bend region. *Geomorphology*. https://doi.org/10.1016/j.geomorph.2010.03.009

Dean, David J., & Schmidt, J. C. (2013). The geomorphic effectiveness of a large flood on the Rio Grande in the Big Bend region: Insights on geomorphic controls and post-flood geomorphic response. *Geomorphology*, *201*, 183–198. https://doi.org/10.1016/j.geomorph.2013.06.020

Diehl, R. M., Wilcox, A. C., Stella, J. C., Kui, L., Sklar, L. S., & Lightbody, A. (2017). Fluvial sediment supply and pioneer woody seedlings as a control on bar-surface topography. *Earth Surface Processes and Landforms*, *42*(5), 724–734. https://doi.org/10.1002/esp.4017

Donovan, M., Belmont, P., Notebaert, B., Coombs, T., Larson, P., & Souffront, M. (2019, June 1). Accounting for uncertainty in remotely-sensed measurements of river planform change. *Earth-Science Reviews*, Vol. 193, pp. 220–236. https://doi.org/10.1016/j.earscirev.2019.04.009

Eckermann, T. K., Hunt, D. S., & Kinoshita, A. M. (2022). Impacts of Vegetation Removal on Urban Mediterranean Stream Hydrology and Hydraulics. Hydrology, 9(10). https://doi.org/10.3390/hydrology9100170

Fryer, J. G., & Brown, D. C. (1986). Lens distortion for close-range photogrammetry. *Photogrammetric Engineering & Remote Sensing*, *52*(1), 51–58.

Gilbert, J. T., & Wilcox, A. C. (2021). An Framework Coupling Sediment Modeling With Invasive Riparian Vegetation Dynamics. *Journal of Geophysical Research: Earth Surface*, *126*(6). https://doi.org/10.1029/2021JF006071

González, E., Sher, A. A., Tabacchi, E., Masip, A., & Poulin, M. (2015). Restoration of riparian vegetation: a global review of implementation and evaluation approaches in the international, peer-reviewed literature. Journal of Environmental Management, 158, 85-94.

González, E., Sher, A. A., Anderson, R. M., Bay, R. F., Bean, D. W., Bissonnete, G. J., … Shafroth, P. B. (2017a). Vegetation response to invasive Tamarix control in southwestern U.S. rivers: A collaborative study including 416 sites. *Ecological Applications*, *27*(6), 1789–1804. https://doi.org/10.1002/eap.1566

González, E., Sher, A. A., Anderson, R. M., Bay, R. F., Bean, D. W., Bissonnete, G. J., … Tabacchi, E. (2017b). Secondary invasions of noxious weeds associated with control of invasive Tamarix are frequent, idiosyncratic and persistent. *Biological Conservation*, *213*(June), 106–114. https://doi.org/10.1016/j.biocon.2017.06.043

González, E., Martínez-Fernández, V., Shafroth, P. B., Sher, A. A., Henry, A. L., Garófano-Gómez, V., & Corenblit, D. (2018). Regeneration of Salicaceae riparian forests in the Northern Hemisphere: A new framework and management tool. Journal of environmental management, 218, 374-387.

Graf, W. L. (1978). Fluvial adjustments to the spread of tamarisk in the Colorado Plateau region. *Bulletin of the Geological Society of America*. https://doi.org/10.1130/0016-

7606(1978)89<1491:FATTSO>2.0.CO;2

Grenfell MC, Dube TI. 2022. Spectral classification, mapping and physical habitat implications of a riparian invasion by Tamarix ramosissima Ledeb. in the Touws River, Klein Karoo, South Africa. African Journal of Aquatic Science, DOI: 10.2989/16085914.2021.2001308.

Griffin GF, Smith DS, Morton SR, Allan GE, Masters KA, Preece N. (1989) Status and implications of the invasion of tamarisk (Tamarix aphylla) on the Finke River, Northern Territory, Australia. *Journal of Environmental Management* 29, 297–315.

Griffin, E. R., Kean, J. W., Vincent, K. R., Smith, J. D., & Friedman, J. M. (2005). Modeling effects of bank friction and woody bank vegetation on channel flow and boundary shear stress in the Rio Puerco, New Mexico. *Journal of Geophysical Research: Earth Surface*, *110*(4), 1–15. https://doi.org/10.1029/2005JF000322

Harms, R. S., & Hiebert, R. D. (2006). Vegetation response following invasive tamarisk (Tamarix spp.) treatment and implications for riparian restoration. *Restoration Ecology*, *14*(3), 461–472. https://doi.org/10.1111/j.1526-100X.2006.00154.x

Hart, C. R., White, L. D., McDonald, A., & Sheng, Z. (2005). Saltcedar control and water salvage on the Pecos river, Texas, 1999-2003. *Journal of Environmental Management*, *75*(4 SPEC. ISS.), 399–409. https://doi.org/10.1016/j.jenvman.2004.11.023

Herrera, A. M., & Dudley, T. L. (2003). Reduction of riparian arthropod abundance and diversity as a consequence of giant reed (Arundo donax) invasion. *Biological Invasions*, *5*(3), 167–177. https://doi.org/10.1023/A:1026190115521

Hughes, M. L., McDowell, P. F., & Marcus, W. A. (2006). Accuracy assessment of georectified

aerial photographs: Implications for measuring lateral channel movement in a GIS. *Geomorphology*, *74*(1–4), 1–16. https://doi.org/10.1016/j.geomorph.2005.07.001

Jaeger, K. L., & Wohl, E. (2011). Channel response in a semiarid stream to treatment of tamarisk and Russian olive. *Water Resources Research*, *47*(2). https://doi.org/10.1029/2009WR008741

Katz, G. L., & Shafroth, P. B. (2003). Biology, ecology and management of *Elaeagnus angustifolia* L. (Russian olive) in western North America. *Wetlands* 23(4), 763-777. https://doi.org/10.1672/0277-5212(2003)023[0763:BEAMOE]2.0.CO;2

Keller, D. L., Laub, B. G., Birdsey, P., & Dean, D. J. (2014). Effects of flooding and tamarisk treatment on habitat for sensitive fish species in the San Rafael River, Utah: Implications for fish habitat enhancement and future restoration efforts. *Environmental Management*, *54*(3), 465–478. https://doi.org/10.1007/s00267-014-0318-7

Manners, R. B., Schmidt, J. C., & Scott, M. L. (2014). Mechanisms of vegetation-induced channel narrowing of an unregulated canyon river: Results from a natural field-scale experiment. *Geomorphology*. https://doi.org/10.1016/j.geomorph.2013.12.033

Marlin, D., Newete, S. W., Mayonde, S. G., Smit, E. R., & Byrne, M. J. (2017). Invasive Tamarix (Tamaricaceae) in South Africa: current research and the potential for biological control. *Biological Invasions*, *19*(10), 2971–2992. https://doi.org/10.1007/s10530-017-1501-6

Martínez-Fernández V, van Oorschot M, de Smit J, et al. (2018) Modelling feedbacks between geomorphological and riparian vegetation responses under climate change in a Mediterranean context. *Earth Surface Processes and Landforms* 43(9): 1825–1835.

Mcshane, R. R., Auerbach, D. A., Friedman, J. M., Auble, G. T., Shafroth, P. B., Merigliano, M. F., … Poff, N. L. (2015). Distribution of invasive and native riparian woody plants across the western USA in relation to climate, river flow, floodplain geometry and patterns of introduction. *Ecography*, *38*(12), 1254–1265. https://doi.org/10.1111/ecog.01285

Merigliano M. F., J. M. Friedman, and M. L. Scott. 2013. Tree-ring records of variation in flow and channel geometry. Pages 145–164 in J. F. Shroder, D. R. Butler, and C. R. Hupp, editors. Treatise on Geomorphology, Volume 12, Ecogeomorphology. Academic Press, San Diego, California.

Merritt, D. M., & Wohl, E. E. (2003). Downstream hydraulic geometry and channel adjustment during a flood along an ephemeral, arid-region drainage. *Geomorphology*, *52*(3–4), 165–180. https://doi.org/10.1016/S0169-555X(02)00241-6

Millar, R. G. (2000). Influence of bank vegetation on alluvial channel patterns. *Water Resources Research*, *36*(4), 1109–1118. https://doi.org/10.1029/1999WR900346

Miller, J. R., & Friedman, J. M. (2009). Influence of flow variability on floodplain formation and destruction, Little Missouri River, North Dakota. *Bulletin of the Geological Society of America*, *121*(5–6), 752–759. https://doi.org/10.1130/B26355.1

Mount, N. J., Louis, J., Teeuw, R. M., Zukowskyj, P. M., & Stott, T. (2003). Estimation of error in bankfull width comparisons from temporally sequenced raw and corrected aerial photographs. *Geomorphology*, *56*(1–2), 65–77. https://doi.org/10.1016/S0169-555X(03)00046-1

Nagler, P. L., Glenn, E. P., Jarnevich, C. S., & Shafroth, P. B. (2011). Distribution and Abundance of Saltcedar and Russian Olive in the Western United States. *Critical Reviews in*

Plant Sciences, *30*(6), 508–523. https://doi.org/10.1080/07352689.2011.615689

Osterkamp, W. R., & Hedman, E. R. (1982). Perennial- streamflow characteristics related to channel geometry and sediment in Missouri River basin. *US Geological Survey Professional Paper*, *1242*.

Pattison, R. R., D'Antonio, C. M., Dudley, T. L., Allander, K. K., & Rice, B. (2011). Early impacts of biological control on canopy cover and water use of the invasive saltcedar tree (Tamarix spp.) in western Nevada, USA. *Oecologia*, *165*(3), 605–616. https://doi.org/10.1007/s00442-010-1859-y

Pavelsky, T. M., & Smith, L. C. (2008). *RivWidth : A Software Tool for the Calculation of River Width from Raster-based Imagery*. *5*(1), 1–4.

Pollen-Bankhead, N., Simon, A., Jaeger, K., & Wohl, E. (2009). Destabilization of streambanks by treatment of invasive species in Canyon de Chelly National Monument, Arizona. *Geomorphology*. https://doi.org/10.1016/j.geomorph.2008.07.004

Rey, D., Neuhäuser, M. (2011). Wilcoxon-Signed-Rank Test. In: Lovric, M. (eds) International Encyclopedia of Statistical Science. Springer, Berlin, Heidelberg. https://doi.org/10.1007/978-3-642-04898-2_616

Richardson, D. M., Holmes, P. M., Esler, K. J., Galatowitsch, S. M., Stromberg, J. C., Kirkman, S. P., ... & Hobbs, R. J. (2007). Riparian vegetation: degradation, alien plant invasions, and restoration prospects. Diversity and distributions, 13(1), 126-139.

Rowland, J. C., Shelef, E., Pope, P. A., Muss, J., Gangodagamage, C., Brumby, S. P., & Wilson, C. J. (2016). A morphology independent methodology for quantifying planview river

change and characteristics from remotely sensed imagery. *Remote Sensing of Environment*, *184*, 212–228. https://doi.org/10.1016/J.RSE.2016.07.005

Rubin, Z., Kondolf, G. M., & Rios-Touma, B. (2017). Evaluating stream restoration projects: What do I learn from monitoring? *Water (Switzerland)*, Vol. 9. https://doi.org/10.3390/w9030174

Schook, D. M., Rathburn, S. L., Friedman, J. M., & Wolf, J. M. (2017). A 184-year record of river meander migration from tree rings, aerial imagery, and cross sections. *Geomorphology*, *293*, 227–239. https://doi.org/10.1016/j.geomorph.2017.06.001

Schumm, S., & Lichty, R. (1963). Channel widening and flood-plain construction along Cimarron River in southwestern Kansas. *Geological Survey Professional Paper*, *352-D*(D), 71–88.

Scott, M. L., Reynolds, L. V., Shafroth, P. B., & Spence, J. R. (2018). The role of a non-native tree in riparian vegetation expansion and channel narrowing along a dryland river. *Ecohydrology*, *11*(7), 1–17. https://doi.org/10.1002/eco.1988

Shafroth, Patrick B, Merritt, David M., Briggs, Mark K., Beauchamp, Vanessa B., Lair, Kenneth D., Scott, Michael L., Sher, A. (2013). Riparian Restoration in the Context of Tamarisk Control. In *Tamarix: A Case Study of Ecological Change in the American West* (pp. 404–425).

Shafroth, Patrick B.Brown, Curtis A., Merritt, D. M. (2010). Saltcedar and Russian Olive Control Demonstration Act Science Assessment: U.S. Geological Survey Scientific Investigations Report 2009-5247.

Shafroth, P. B., Cleverly, J. R., Dudley, T. L., Taylor, J. P., Van Riper, C., Weeks, E. P., & Stuart, J. N. (2005). Control of Tamarix in the western United States: Implications for water salvage, wildlife use, and riparian restoration. *Environmental Management*, *35*(3), 231–246. https://doi.org/10.1007/s00267-004-0099-5

Sher, A. A., Marshall, D. L., & Taylor, J. P. (2002). Establishment patterns of native Populus and Salix in the presence of invasive nonnative Tamarix. *Ecological Applications*, *12*(3), 760–772. https://doi.org/10.1890/1051-0761(2002)012[0760:EPONPA]2.0.CO;2

Sogge, M. K., Sferra, S. J., & Paxton, E. H. (2008). Tamarix as habitat for birds: Implications for riparian restoration in the Southwestern United States. *Restoration Ecology*, *16*(1), 146–154. https://doi.org/10.1111/j.1526-100X.2008.00357.x

Stover, J. E., Keller, E. A., Dudley, T. L., & Langendoen, E. J. (2018). Fluvial geomorphology, root distribution, and tensile strength of the invasive giant reed, Arundo donax and its role on stream bank stability in the Santa Clara River, southern California. *Geosciences (Switzerland)*, *8*(8). https://doi.org/10.3390/geosciences8080304

Stromberg, J. C., Lite, S. J., Marler, R., Paradzick, C., Shafroth, P. B., Shorrock, D., … White, M. S. (2007). Altered stream-flow regimes and invasive plant species: The Tamarix case. *Global Ecology and Biogeography*, *16*(3), 381–393. https://doi.org/10.1111/j.1466-8238.2007.00297.x

Tooth S. 2013. Dryland fluvial environments: assessing distinctiveness and diversity from a global perspective Shroder J., Wohl E.E. (Eds.), Treatise on Geomorphology, Vol. 9,, Fluvial Geomorphology, Academic Press, San Diego (2013), pp. 612-644.

Valente, J. J., McCune, K. B., Tamulonis, R. A., Neipert, E. S., & Fischer, R. A. (2019).

Treatment pattern mitigates negative, short-term effects of stepwise Russian olive eradication on breeding birds. *Ecosphere*. https://doi.org/10.1002/ecs2.2756

Vincent, K. R., Friedman, J. M., & Griffin, E. R. (2009). Erosional consequence of saltcedar control. *Environmental Management*, *44*(2), 218–227. https://doi.org/10.1007/s00267-009-9314-8

Wolman, M.G., and Gerson, R., 1978, Relative scales of time and effectiveness of climate in watershed geomorphology: Earth Surface Processes, v. 3, p. 189–208, doi: 10.1002/esp.3290030207.

Yin, C. H., Feng, G., Zhang, F., Tian, C. Y., & Tang, C. (2010). Enrichment of soil fertility and salinity by tamarisk in saline soils on the northern edge of the Taklamakan Desert. *Agricultural Water Management*, *97*(12), 1978–1986. https://doi.org/10.1016/j.agwat.2009.02.013

Zavaleta, E. (2000). The economic value of controlling an invasive shrub. *Ambio*, *29*(8), 462–467. https://doi.org/10.1579/0044-7447-29.8.462

CHAPTER 4: EVALUATION OF GULLY EROSION FOR ARCHAEOLOGICAL PRESERVATION IN WUPATKI NATIONAL MONUMENT[3]

4.1 Introduction

Hillslope gullies are problematic for cultural sites located across the Southwest (e.g. Pederson et al., 2006) and around the world (e.g. Gouma et al., 2011), putting important cultural artifacts at risk of erosion. Factors that contribute to the formation and development of gullies include processes such as water erosion from overland flow. The geology and topography of the landscape, soil and vegetation cover, and local climate influence erosion. Sediment yields tend to be greatest in semi-arid environments where precipitation is sufficient to generate soils and drive erosion, but limits vegetation growth that stabilizes hillslopes (Langbein and Schumm, 1958). In these environments, in particular, where the disparity between driving forces (precipitation) and resisting forces (vegetation) is increasing due to global climate warming, increased erosional risks are predicted as more extreme weather causes frequent or intense rainfall, and flooding (IPCC, 2021). At Wupatki National Monument (WUPA) located in northern Arizona (Figure 4.1), heavy sporadic rainstorms in the past decade, lack of vegetation, and presence of unconsolidated volcanic-derived cinders exposes archaeological sites to erosion. Mean annual temperature (~15°C) at WUPA is expected to increase and could shift soil moisture and precipitation patterns (Andrews et al., 2019). Wind and water work in concert to shape the landscape by mobilizing and concentrating cinders in lower topographic areas, and then

[3]Chapter published as Wieting, C., S. Rathburn, and J. Kemper. 2024. Evaluation of gully erosion for archaeological preservation in Wupatki National Monument. Natural Resource Report NPS/WUPA/NRR—2024/2630. National Park Service, Fort Collins, Colorado. https://doi.org/10.36967/2302447.

mobilizing them during rainstorms. At WUPA, lithological differences between volcanic cinders and underlying sedimentary rocks, and landscape processes such as surface runoff influence the progression of gullies at or near archaeological sites. This research was conducted to collect baseline geomorphological data and identify archaeological resources of highest vulnerability to landscape erosion from rainfall events. From this study, managers can prioritize long-term management actions needed to protect archaeological resources within WUPA.

4.2 Previous Research

A gully is a relatively deep, eroding channel that forms on valley sides and on valley floors where no well-defined channel previously existed (Schumm et al., 1984). Typically, gullies are narrow, steep-sided channels, usually formed by the erosion of water (Thwaites et al., 2021) from head cut retreat, steepening of the gully walls, and eventually enlargement and collapse (Higgins et al., 1990). Processes responsible for head cut retreat include sapping at the gully base (Emmett, 1968) and concentrated overland flow. Where gullies have been studied on cinder cones (Dóniz et al., 2011), gully formation is attributed to concentrated overland flow during rain events, but gullies in these settings may be initiated by mud and debris flows (Dóniz et al., 2011). In semi-arid climates, gully erosion generally results from overland flow following short, intense precipitation events, and is not typically influenced by piping or seepage (Petersen, 2003; (Pederson et al., 2006).

Research into gully formation began with the recognition that considerable erosion resulted from the conversion from natural vegetative cover to crops, and the need for soil conservation practices, throughout the U.S (e.g. Ireland et al., 1939). Other research identified stages of gully development (Ireland et al., 1939; Bariss, 1972). Several studies have found a

relationship between slope and contributing area that identifies a threshold for gully erosion (Patton and Schumm, 1975; Vandekerckhove et al., 2000; Wu and Cheng, 2005, Pederson et al., 2006). Patton and Schumm (1975) identified a geomorphic threshold valley slope for a given contributing area above which gullies formed in the Piceance Creek Basin, CO. Patton and Schumm (1975) found that the relationship between valley slope and contributing area did not pertain to drainage basins smaller than about 18 km^2 (1800 ha). In these small basins, variations in vegetative cover or variations in the properties of the alluvium prevented development of a critical threshold slope (Schumm et al., 1984). Pederson et al. (2006) also used the slope-area approach to identify threshold slopes and predict gully formation around archaeological sites in Grand Canyon. They identified gully erosion thresholds and found that gradient was the most important control on gully extent, but their topography-based predictive models lacked soil property influences and resulted in many false-positives. This study fills a gap in knowledge of gully formation in small drainage basins (median=0.0285 ha; 285 m2) where volcanic cinders cover underlying sandstone bedrock.

4.3 Study Objectives

To help WUPA managers prioritize long-term management actions to preserve the archaeological record, I evaluated the mechanisms that influence the evolution and expansion of gullies and assessed archaeological site vulnerability. I collected baseline geomorphological data at WUPA in summer 2021. To analyze hydrologic and erosional processes due to lithological differences, I quantified physical and hydraulic differences between Moenkopi- and cinder-dominated sediments. Additionally, I conducted a multiscale five-year geomorphic change analysis using aerial LiDAR (2016) and field-collected data (2021). The larger, coarse-scale

analysis included 35 measured gullies across all of Wupatki Wash, while the high-resolution analysis was focused on a small hillslope in Wupatki Wash. Based on these analyses, I (1) assessed gullies based on changes in gully morphology, and (2) categorized archaeological sites within a small drainage with abundant archaeological sites based on vulnerability from erosion and runoff processes. I hypothesize that a threshold critical slope will be identified for a given contributing area above which gully erosion is expected. In addition, I hypothesize that lithology influences erosion such that Moenkopi-dominated catchments will increase runoff and show greater elevation change in gullies over time.

4.4 Study Area

Located about an hour's drive northeast of Flagstaff, Arizona, WUPA (Figure 4.1) is a culturally diverse area that contains over 2600 prehistoric and historic archaeological sites (Baldwin et al., 2015). Most sites are small one-room field houses with scattered artifacts, but the presence of large pueblos indicate prehistoric communities of people gathered in the WUPA area to trade, play, and reside seasonally (pers. comm., Lisa Leap).

4.4.1 Site Characteristics

There are three dominant geological materials found at WUPA: The Moenkopi Formation, the Kaibab Formation, and eolian cinder deposits. The Moenkopi Formation consists of Triassic (~240 million years old) sandstones, siltstones and mudstones deposited in a variety of geologic settings including shallow marine, beach, tidal flat, lagoon, and floodplain (Billingsley et al., 2007). The term "Moenkopi-derived sediments" is used here to encompass the entire Moenkopi Formation, but generally refers to the sediments derived from sandstone members. The eolian cinder deposits seen at WUPA are Quaternary in age and originated from

Sunset Crater Volcano, located just south of WUPA. Sunset Crater Volcano erupted in 1085, ejected basaltic volcanic fragments, and spread a layer of cinders on top of Moenkopi sedimentary rocks throughout WUPA (Hanson, 2003). Cinder deposits, originally deposited less than 10 cm thick (Hooten et al., 2001), then later redistributed by wind and water, acted as a mulch atop barren desert soils for prehistoric agricultural practices and helped increase infiltration and soil moisture, and decrease runoff (Grattan and Torrence, 2007). Eolian transport of the cinders over time has created dune deposits throughout WUPA (Billingsley et al., 2007). Gullies and rills generally form within volcanic-derived cinders that blanket the Moenkopi Formation, or within Moenkopi sediments themselves. The Kaibab Formation also outcrops within WUPA, but cinder and Moenkopi-derived sediments are ubiquitous and more relevant in this study. I focus our analysis on the eastern portion of the national monument, within Wupatki Wash, a tributary to Deadman Wash (Figure 4.1). The semi-arid study area hosts barren areas and sparsely vegetated sandstone outcrops and badlands (Hansen et al., 2004). Saltbrush (*Atriplex canescens*), Mormon tea (*Ephedra viridis*), Apache plume (*Fallugia paradoxa*), rabbitbrush (*Ericameria nauseosa*), and oneseed juniper (*Juniperus monosperma*) are common at WUPA (Hansen et al., 2004).

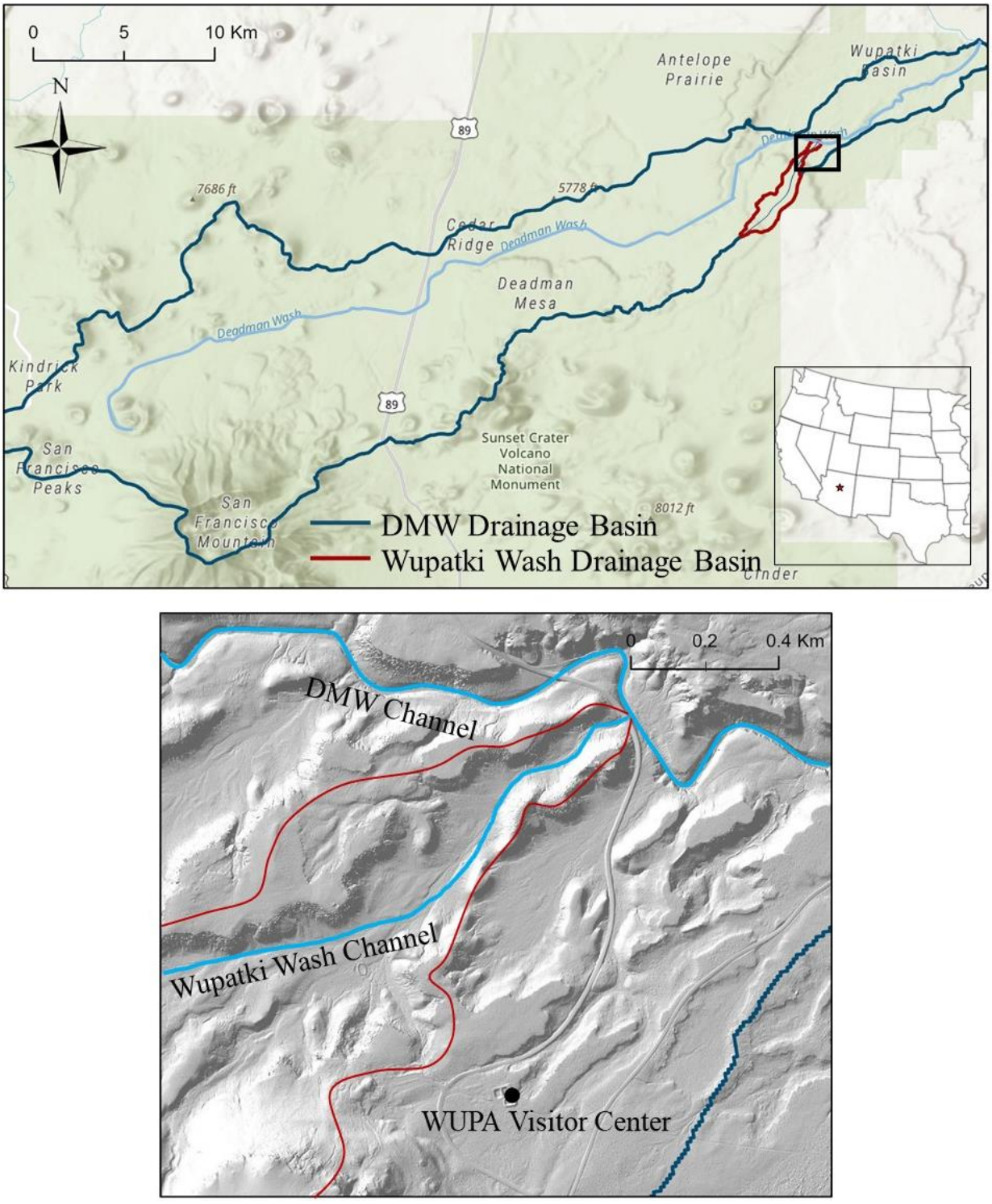

Figure 4.1. Drainage basin map of Deadman and Wupatki Washes. The callout box displays the confluence of the main Wupatki and Deadman Wash channels, near the WUPA Visitor Center.

Wupatki Wash is an ephemeral channel that exhibits discontinuous flow during heavy rains due to the presence of permeable volcanic-derived cinders. WUPA receives an average annual rainfall of around 20 cm, most of which falls during the summer monsoon. Daily precipitation data were gathered from a weather station within WUPA (Station USC00029542) and analyzed to better understand the occurrence and intensity of rainstorms in the region. Several notable events took place in the summers of 2013, 2016, 2018, and 2022 (Figure 4.2). Additional higher temporal resolution (15 minute) precipitation data were received from National Park Service (NPS) staff for the month of August 2022. These data indicate that a 100-to-200-year precipitation event took place on August 15, 2022, when 4.24 centimeters of rain fell within 30 minutes (Figure 4.3). Short-duration, high intensity thunderstorms underscore the need to understand erosion and landscape change in semi-arid environments.

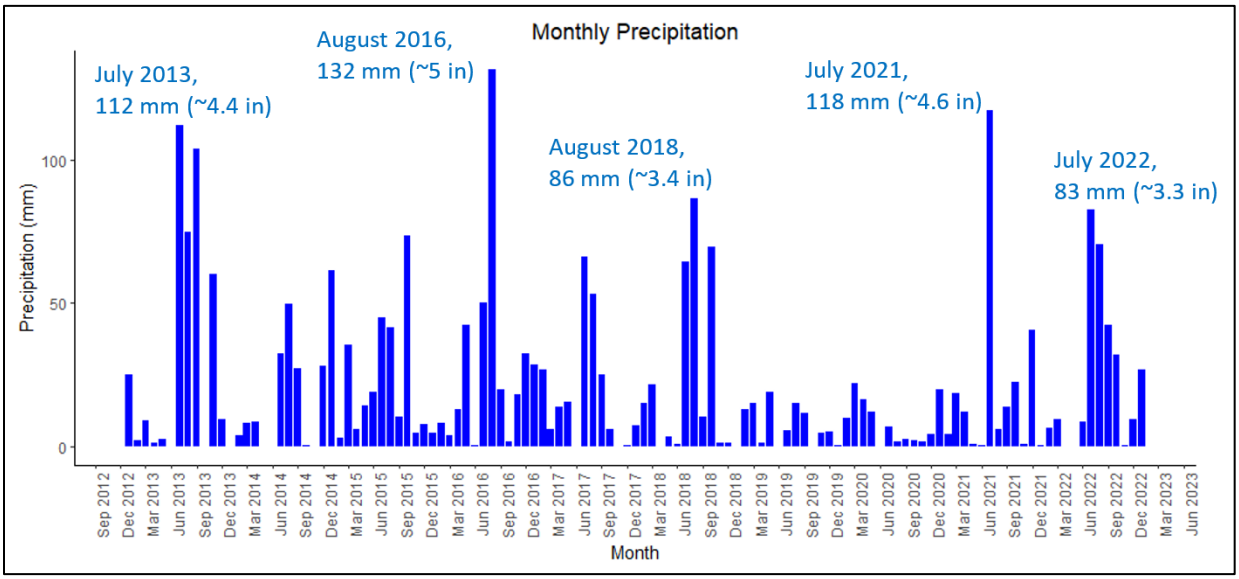

Figure 4.2. Monthly precipitation totals at WUPA, summarized from daily precipitation data. Daily precipitation and other weather data come from COOP station ID USC00029542, located within the monument.

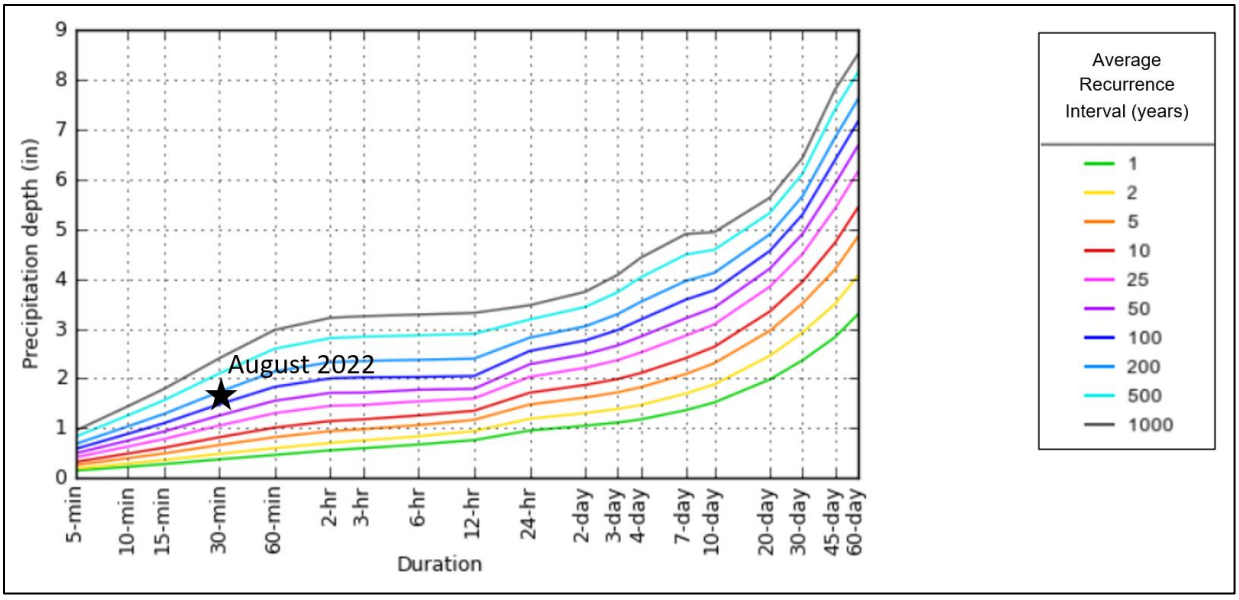

Figure 4.3. The August 15, 2022 rainstorm (1.67 inches in 30 minutes) is the equivalent to a 100- to 200-year precipitation event (NOAA, 2023).

At WUPA, water and sediment concentrate in concave regions of hillslopes due to surface flow off Moenkopi Formation sandstone that forms bands of cliffs (Figure 4.4). Cliff bands are laterally extensive conspicuous features with a near vertical slope (Figure 4.5). Incisional features found along cliff band convexities are generally parallel rills (smaller than gullies, no more than 0.3 m deep; Thwaites et al., 2020) formed within the Moenkopi Formation, due to the lack of accumulated cinder deposits. Gullies at WUPA generally originate at the vertical cliffs or rockfall area of Moenkopi sandstone, have a linear planform (Figure 4.5 and 4.6), are V-shaped in cross-section with banks and bed composed of primarily cinders, and have gradual, inclined gully heads (Thwaites et al., 2020). The elementary gully classification (EGC) was used to further classify gullies at WUPA (Figure 4.6) to help identify gully erosion processes.

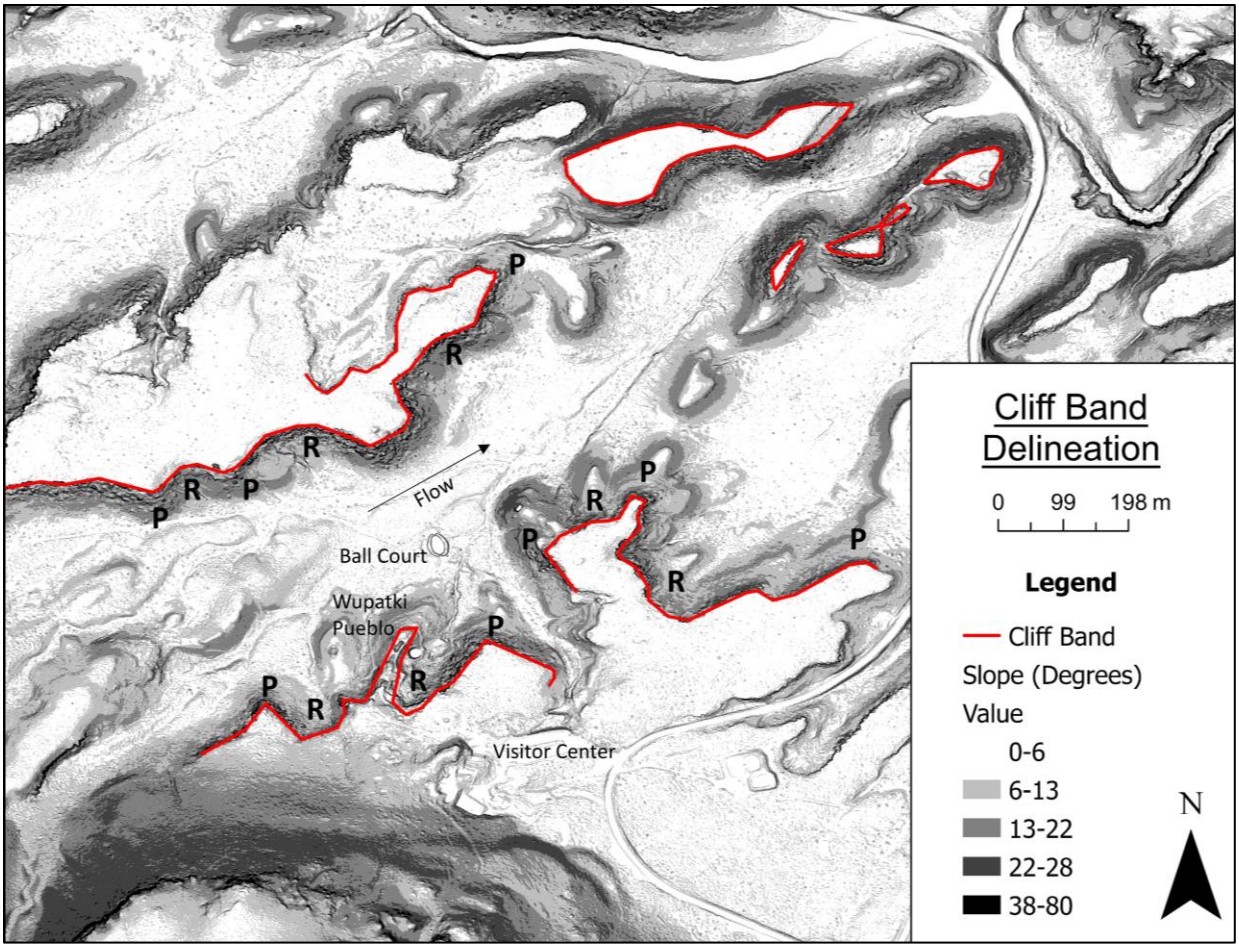

Figure 4.4. Map illustrating locations of points (P) and recesses (R) formed by linear cliff bands of Moenkopi Formation. Map adapted from Anderson (2021).

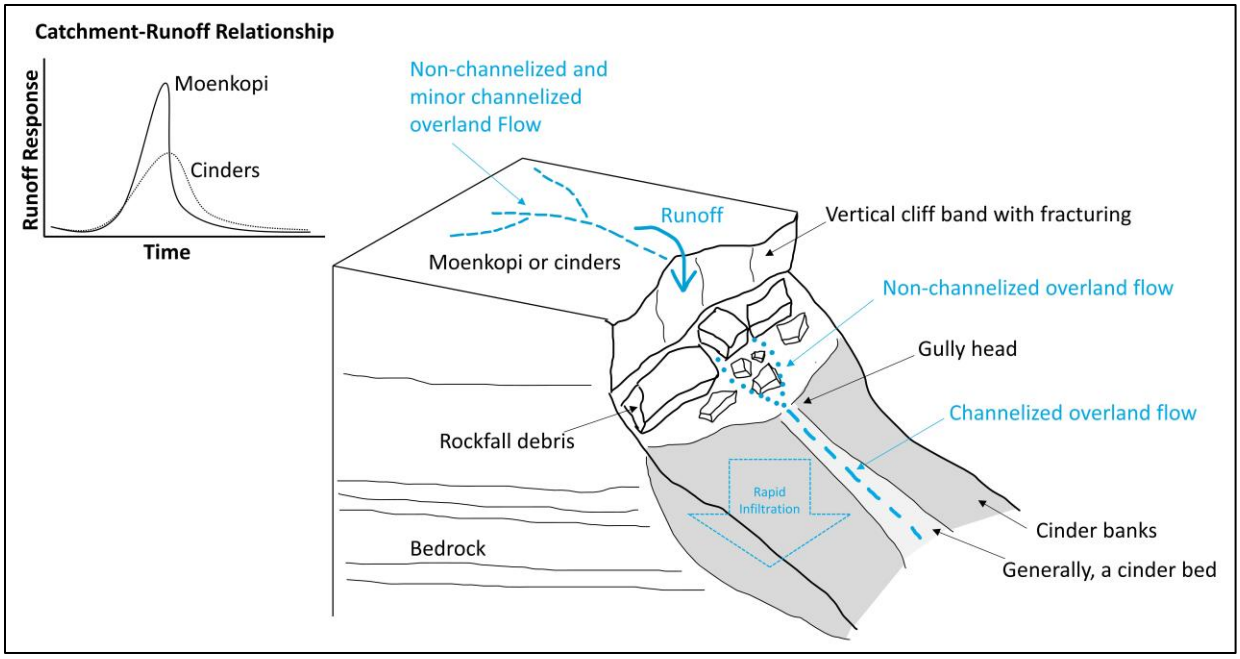

Figure 4.5. Conceptual diagram of the interaction between local geology and hydrological processes including infiltration, overland flow, and runoff. Following a rainstorm, water flows on the surface of catchments as either non-channelized or minor channelized overland flow, pours over cliff bands of Moenkopi sandstone, flows down hillslopes through rockfall, and eventually concentrates in gullies formed within cinder deposits on top of Moenkopi bedrock. Gully heads generally form near the base of rockfall material where channels initiated in cinder deposits. Depending on surface conditions in the gully catchment, I expect differences in the runoff response following a rainstorm (upper left graph): quicker, flashier runoff in catchments composed of predominantly Moenkopi sediments and bedrock compared to a more delayed and muted runoff response from catchments covered with cinders.

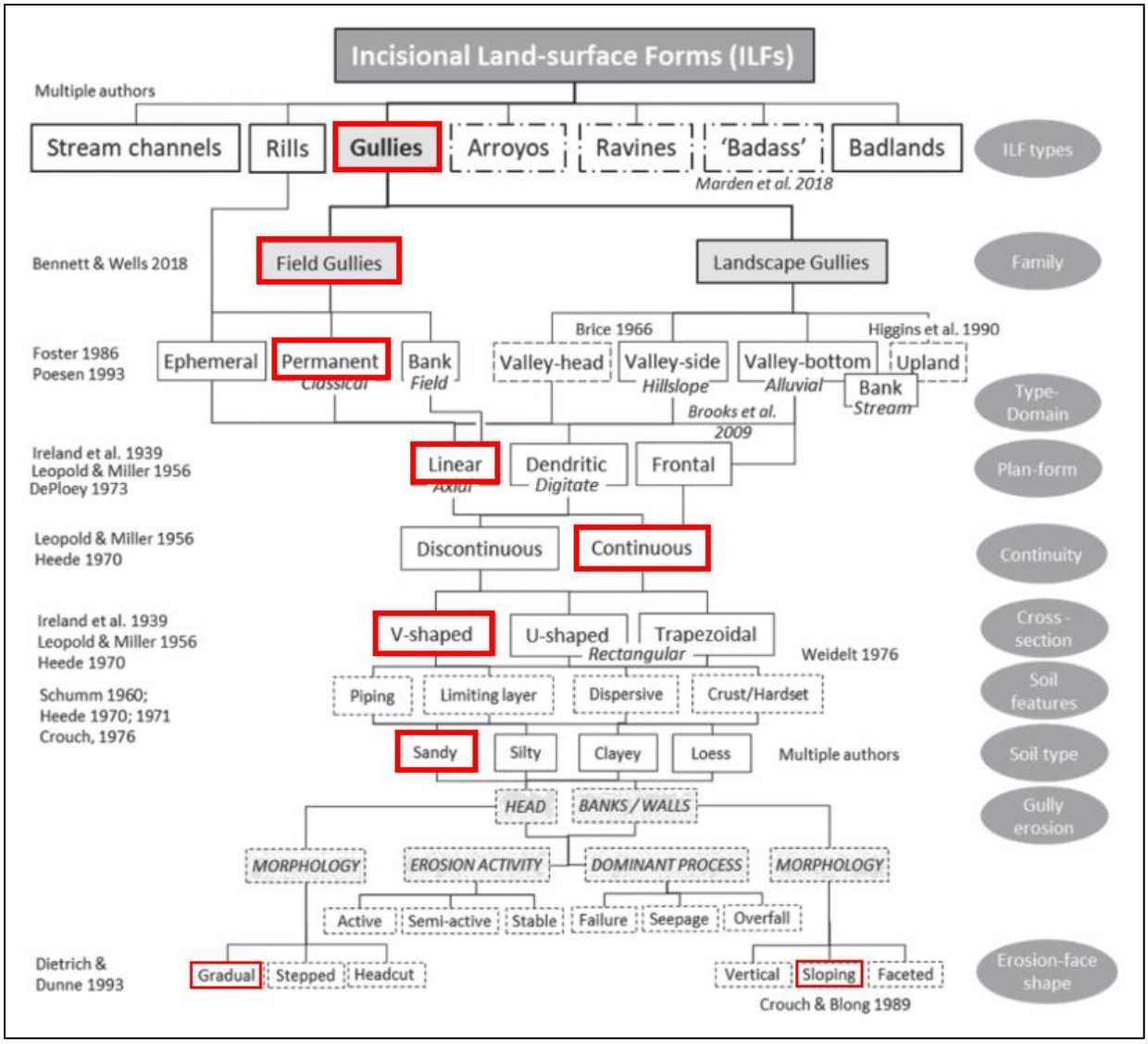

Figure 4.6. Classification of gullies at WUPA (red boxes) using the elementary gully classification proposed by Thwaites et al. (2021). Gully erosion classifications including "erosion activity" and "dominant process" were investigated within this study and thus not outlined.

4.5 Study Methods

4.5.1 Baseline Geomorphological Data Collection

When intense rainstorms occur in a semi-arid environment such as WUPA, surface characteristics determine the amount of water that infiltrates or runs off. A Mini Disk tension

infiltrometer was used to quantify infiltration and estimate field-saturated hydraulic conductivities (Kfs) of surficial sediments in catchment areas of 17 gullies in Wupatki Wash. The infiltrometer was chosen because it is compact and requires minimal water. Water immediately begins infiltrating into the soil at a rate determined by the hydraulic properties of the soil (Decagon Devices, 2014), and the water level on the device is recorded over time. The shortest infiltration experiment ran for 2 minutes and experiments generally were conducted for a maximum of 10 minutes. Where possible, at least 15–20 mL of water was infiltrated during each measurement for adequate calculation of Kfs (Decagon Devices, 2014). Kfs was calculated from infiltration data and Van Genuchten parameters related to the soil type (Decagon Devices, 2014). To ensure good contact between the infiltrometer and the surface, loose litter was removed from the surface. An average value of Kfs was calculated from three measurements conducted in the upper, middle, and lower portion of the catchment. Sediment samples were collected at each gully bed and left/right banks, and then sieved in the laboratory using standard sieving practices (ASTM, 2018). Four sediment types were compared: volcanic-derived cinders, and Moenkopi-derived clay, silty clay, and sand.

Additionally, I collected field-based information on catchment properties (catchment area, vegetation cover, surficial materials, and presence of cliff bands) that influence surface processes to examine linkages between catchments and gullies. Our data collection also tested previously quantified relationships between catchment area and gully head slope to identify topographic thresholds that initiate erosion in gullies (Patton & Schumm, 1975; Pederson et al., 2006). Vegetation cover was recorded as a percentage from 0–100% and then classified as low (0-30%), medium (31-70%), and high (71-100%). Cliff band height was measured using a laser range finder.

4.5.2 Topographic Data Collection and Landscape Analyses

4.5.2.1 Topographic Data Collection

A total of 35 gullies were surveyed using a Topcon Real-Time-Kinematic (RTK) surveying system (Figure 4.7) with sub-centimeter accuracy. At each gully, topographic point data were collected starting at the top of the gully's drainage catchment, down the center of the catchment and gully, and at three representative cross-sections, recording notable slope breaks (Figure 4.8). The three cross-sections were strategically located near the top, middle, and bottom of the gully channel. Ten larger gullies required additional cross-sections. Initially, field data were collected to develop a relationship between catchment area and gully head slope to quantify a topographic threshold at which erosion initiates.

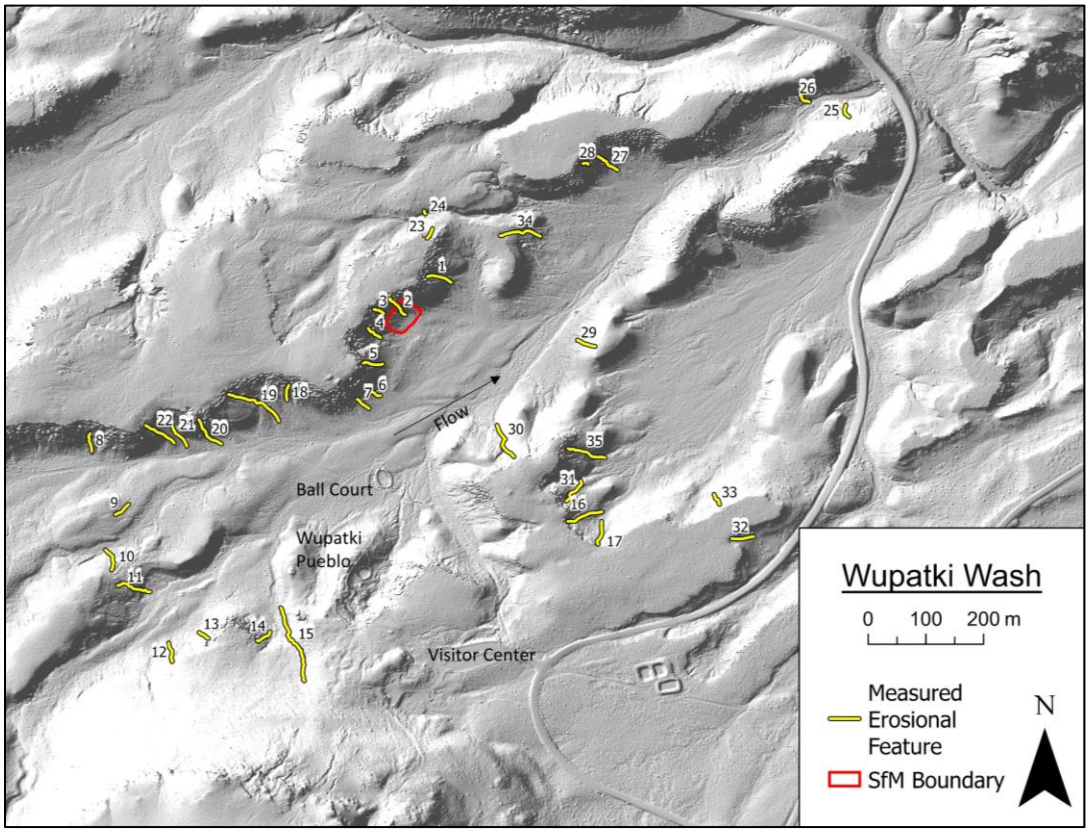

Figure 4.7. The locations of 35 total gullies surveyed within WUPA and nearby archeological resources.

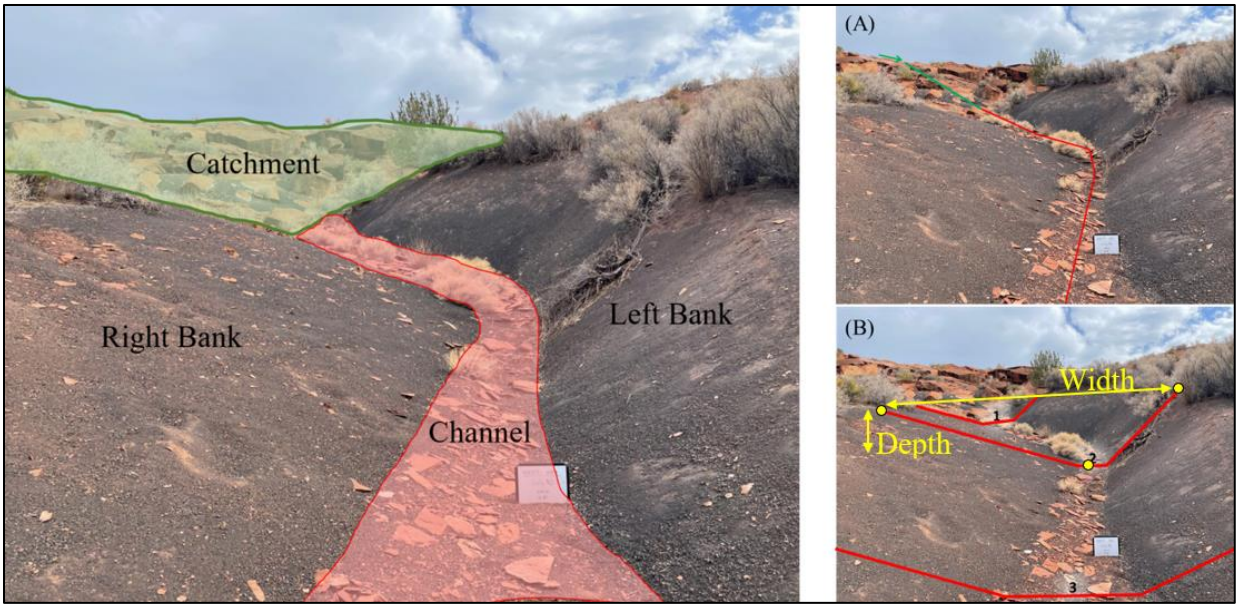

Figure 4.8. Example of topographic surveying methods used at each gully. (A) Surveys began at the top of the catchment, proceeded down the center of the catchment, and down the channel centerline. (B) Three cross-sections across the channel near the top, middle, and bottom of the gully were also surveyed. Yellow dots illustrate examples of points used for gully width and depth calculations for a single cross-section. For gully width, the top of bank locations was used and for gully depth, the vertical distance was calculated between the cross-section minimum elevation (bottom point) and lower of the two top bank elevations.

Longitudinal profiles were created in ArcGIS Pro (version 2.6.0) to compare field-collected (2021) to aerial LiDAR (2016) topographic data. Elevation data were extracted from elevation data collected from the 2016 LiDAR at the exact (x,y) coordinates from the 2021 surveyed point data using the "extract values to points" tool in ArcGIS Pro. Longitudinal profiles were used to calculate changes in gully head slope and median elevation difference (MED) over the five-year period, and cross-sections were used to calculate changes in gully dimensions including width, depth, and length. Gullies were then classified based on MED, and further evaluated for changes in width and depth individually. From cross-section data, top width was used for the average gully width, and the bottom to lowest top value was used for average gully depth (Figure 4.8). I analyzed whether statistical differences existed for average width and average depth changes using a paired nonparametric Wilcoxon signed rank test, with a

significance level of 0.05. The gully head slope was identified as the region near the top of the gully channel where flow concentrates. Changes in gully head slope were used to describe changes to overall gully behavior.

4.5.2.2 Slope-Area Analysis and Gully Prediction

Similar to Pederson et al. (2006), I delineated a topographic threshold to predict gully erosion using gully head slope and catchment area:

$$S_c = aA^{-b} \quad \text{(Eq. 4.1)}$$

Where S_c is the critical slope gradient (m/m), A is the catchment area (ha), a is a threshold coefficient and b is a scaling exponent. Catchment areas were delineated in the field with a handheld GPS, and then verified using WMS software (Aquaveo, 2022) due to difficulties distinguishing catchment boundaries in the field (low slope, homogenous surface material, and lack of channelized flow paths). Ultimately, for consistency, catchment areas obtained from WMS were used. Twenty-one of the 35 gullies were included in this analysis based on similarities in bed and bank materials, presence of a cliff band, and gully morphology. Gully head slope versus catchment area was plotted and fitted to a linear regression. The variables a and b were derived from a threshold line by shifting the regression line down to the base of the main scatter (Pederson et al., 2006).

The slope-area analysis predicts where gullies form was completed using ArcGIS Pro. First, the D∞ algorithm within the flow accumulation tool was used to create a contributing area raster (Tarboton, 1997). Then, two slope rasters were created: a threshold slope raster using the raster calculator tool and variables defined from the threshold line, and an "actual" slope raster

generated from the 2016 aerial LiDAR. The gully prediction map was produced using the raster calculator tool by calculating where “actual” slope exceeds threshold slope.

4.5.2.3 Structure from Motion Analysis

For a high spatial resolution geomorphic change analysis and to evaluate topographic change over a five-year period, I applied the structure from motion (SfM) method on a 0.17 ha region in Wupatki Wash. SfM is a low-cost photogrammetric method that uses digital photographs to create 3-dimensional (3D) surfaces, and has become increasingly popular in geoscience and archaeological applications (e.g. Howland et al., 2018; Westoby et al., 2012; Jones & Church, 2020; Sha et al., 2023). I systematically walked in a grid pattern and used an iPhone 12 attached to a 5-m tall pole (Figure 4.9). At each grid point, four photographs were taken in orthogonal directions to capture a variety of angles for sufficient overlap to estimate 3D structures from 2D images. Agisoft Metashape Professional (Agisoft, 2020) software was used to create a digital elevation model (DEM) from 2,313 photographs and 24 RTK-surveyed control points. A DEM of difference (DoD) was then created using ArcGIS Pro from topography derived from 2016 aerial LiDAR and 2021 photographs (Wheaton et al., 2010). Within ArcGIS Pro, large vegetation patches were removed from the model to eliminate topographic skew from the DoD analysis. Similar to Sholtes et al. (2018), I created two sample polygon shapefiles on relatively flat and steep areas where I did not expect change to occur to correct for bias and remove values within +/- two standard deviations of the error within sampled areas (Wheaton et al., 2010).

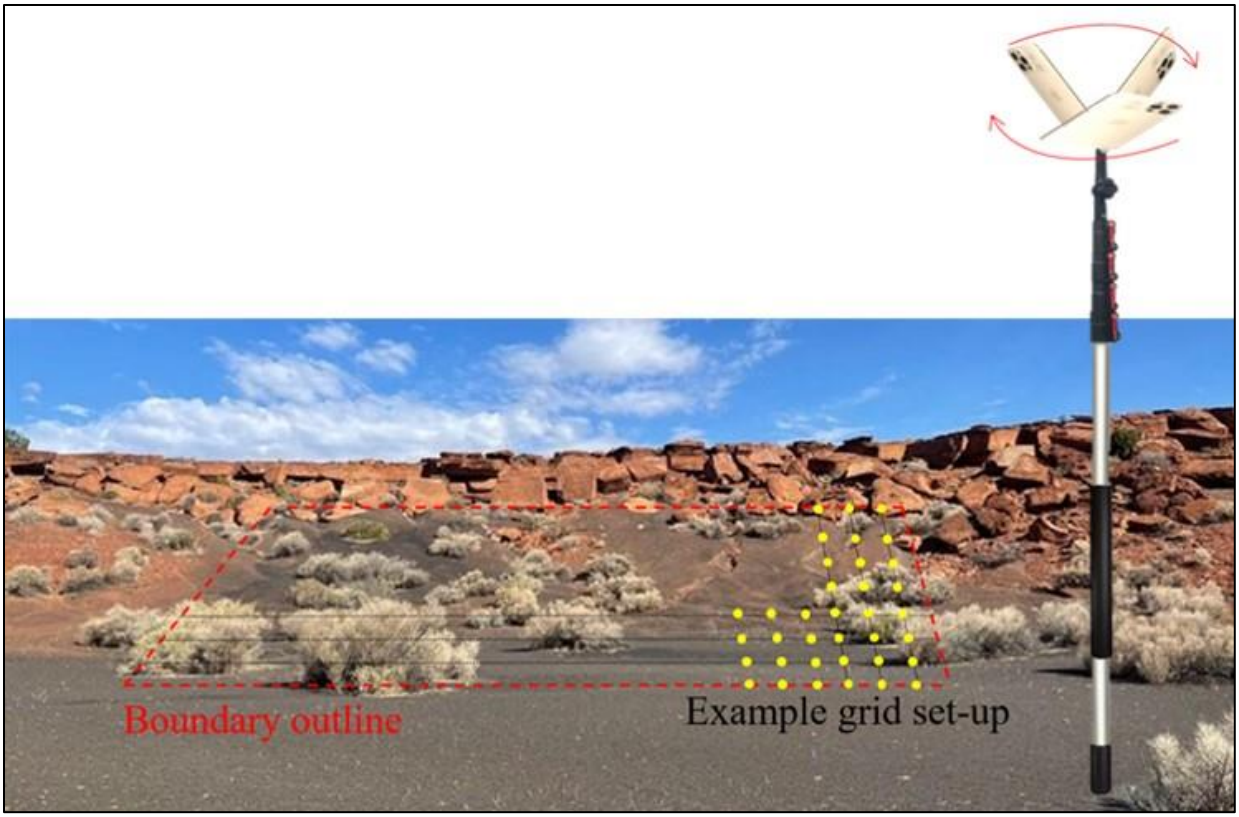

Figure 4.9. Grid system used for collecting photographs for SfM analysis.

4.5.3 Archaeological Site Vulnerability Assessment

Archaeological site vulnerability was classified as either high, moderate, low, or unclassified based on proximity to a cliff band or a measured gully (Figure 4.10) for 54 archaeological sites located in the eastern portion of WUPA. Geomorphically, cliff bands are important features in WUPA because as water flows over the vertical face, higher velocities result in erosion of the underlying materials and downslope concentrated flow paths. Gullies readily form within the volcanic cinders that blanket the Moenkopi Formation (Figure 4.5) below cliff bands. I used the buffer tool in ArcGIS Pro to determine archaeological site proximity to measured gullies and cliff bands. Cliff bands were delineated in ArcGIS Pro using aerial imagery from the National Agriculture Imagery Program (NAIP) that was obtained through the USGS Earth Explorer. If a site was located within 5 m of measured gullies or delineated cliff bands, the

archaeological site was given a high erosion vulnerability classification (Figure 4.10). I chose a conservative buffer of 5 m because of the amount of landscape change observed within the five-year time frame, uncertainty in the coordinates of the archaeological site locations provided, presence of atypical gully head morphology in some locations, and to ensure I captured any archaeological sites with a potential for future erosion. Otherwise, site classification was based on underlying lithology, field observations, or personal communication with NPS staff (Figure 4.10).

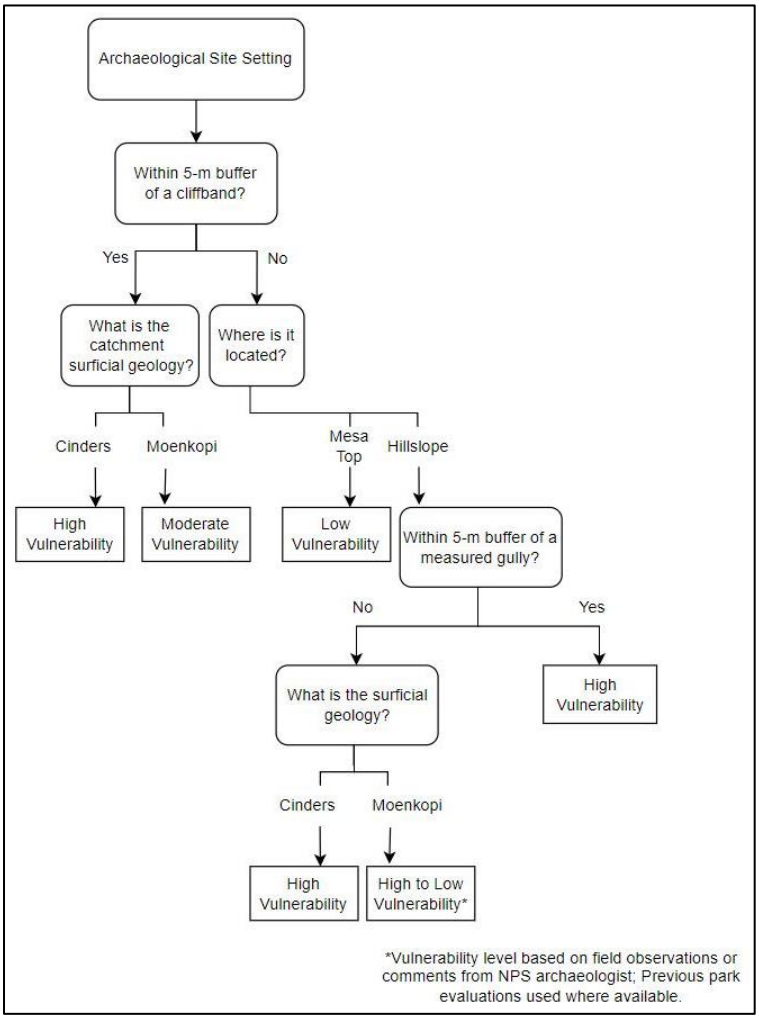

Figure 4.10. Flowchart used to assign erosion vulnerability classifications to archaeological sites.

4.6 Results

4.6.1 Cinder and Moenkopi-derived sediment differences

Infiltration data recorded from the infiltrometer are summarized in Figure 4.11. Water infiltrated quickly into cinder-dominated sediments and resulted in higher cumulative infiltration and faster infiltration rates (slopes of infiltration curves) compared to Moenkopi-dominated sediments (Figure 4.11). Kfs estimates were compared for cinders and Moenkopi-derived sediments of sand, silty clay, and clay (Figure 4.12). Van Genuchten parameters for sand were used for calculations for cinders based on grain size analyses from sediment samples collected in the field. Cinders showed the highest Kfs with an average of 0.21 cm/sec, followed by sand (0.17 cm/sec), silty clay (0.026 cm/sec), and clay (0.012 cm/sec).

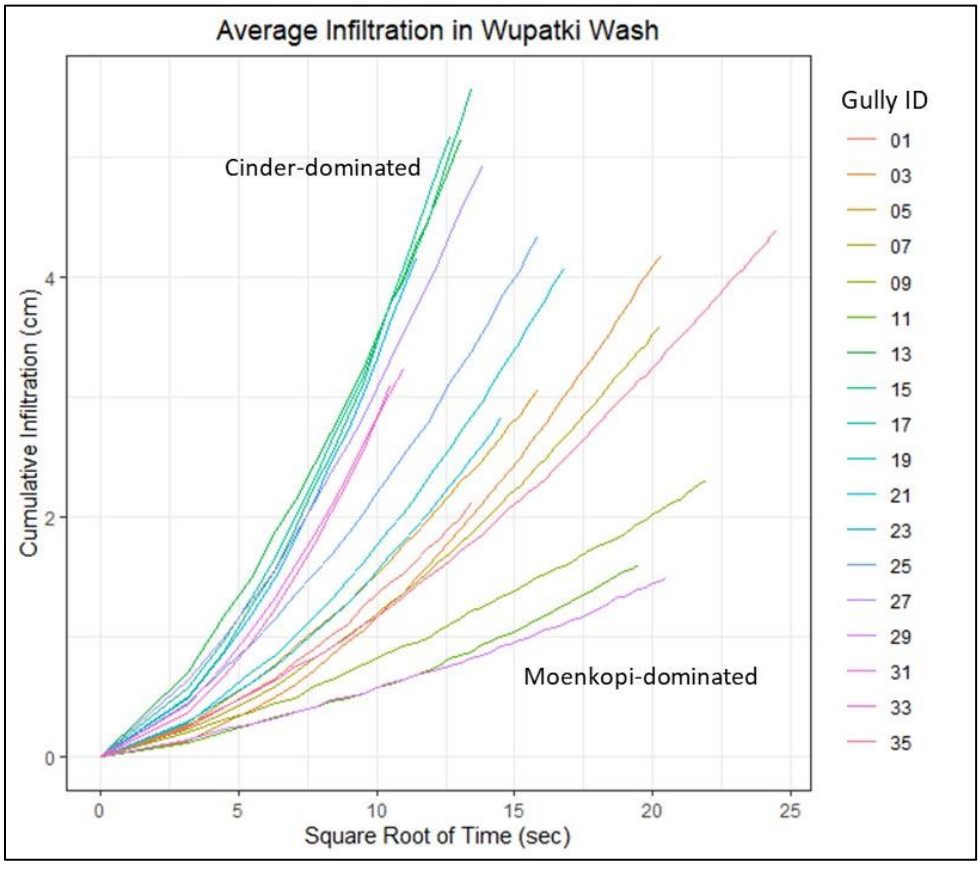

Figure 4.11. Cumulative infiltration curves from infiltrometer experiments. Less water infiltrated into the Moenkopi-dominated sediments compared to the cinder-dominated, and at a slower rate.

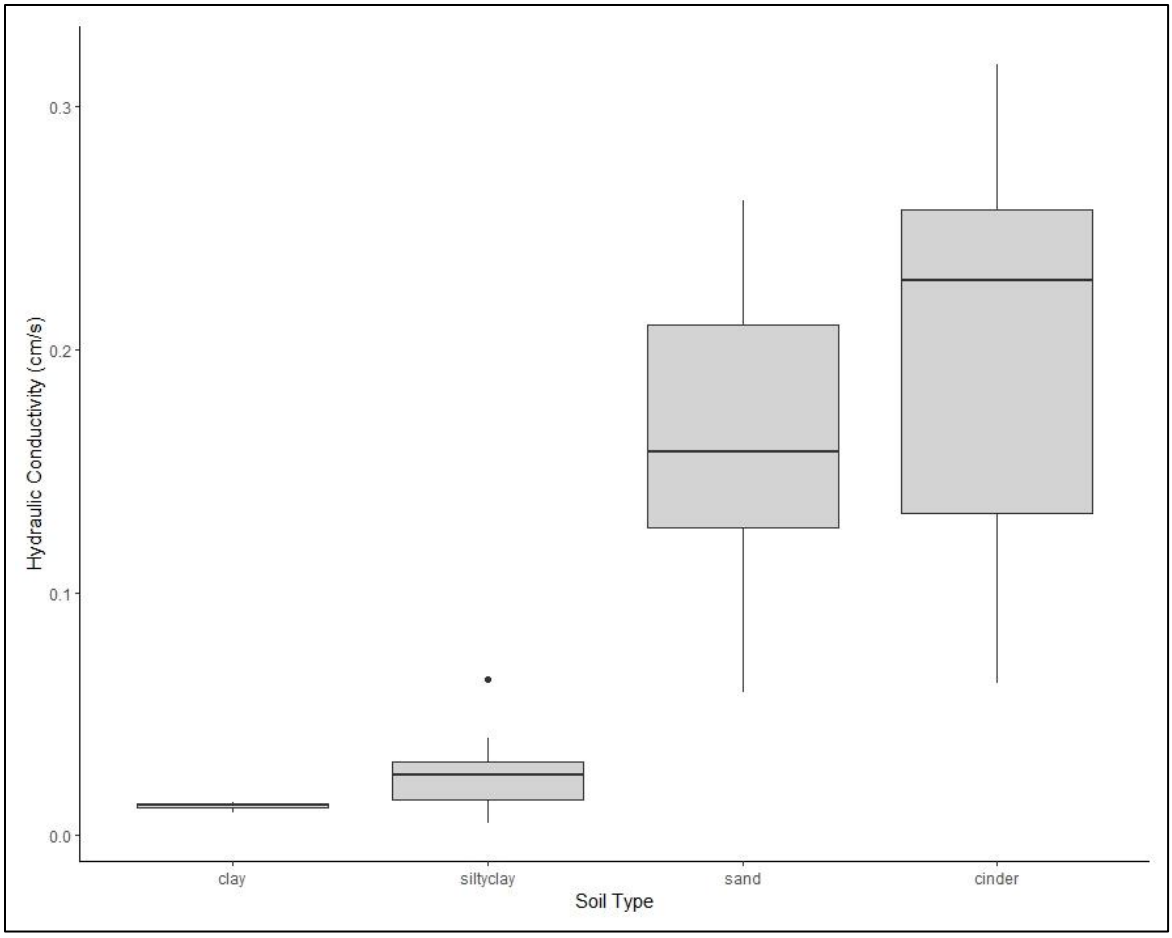

Figure 4.12. Estimates of hydraulic conductivity for various soil types derived from cumulative infiltration data collected in the field using the infiltrometer. Van Genuchten parameters for sand were used for calculation of hydraulic conductivity of cinders.

A total of 28 sediment samples were sieved from 9 measured gullies. Gullies 8, 26, 28, 31, and 32 were composed of mostly cinders, and gullies 7, 19, 20, and 29 (Figure 4.7) contained mostly Moenkopi-derived sediments. The average median grain size was 1.01 mm for cinders and 1.48 mm for Moenkopi-derived sediments (Figure 4.13).

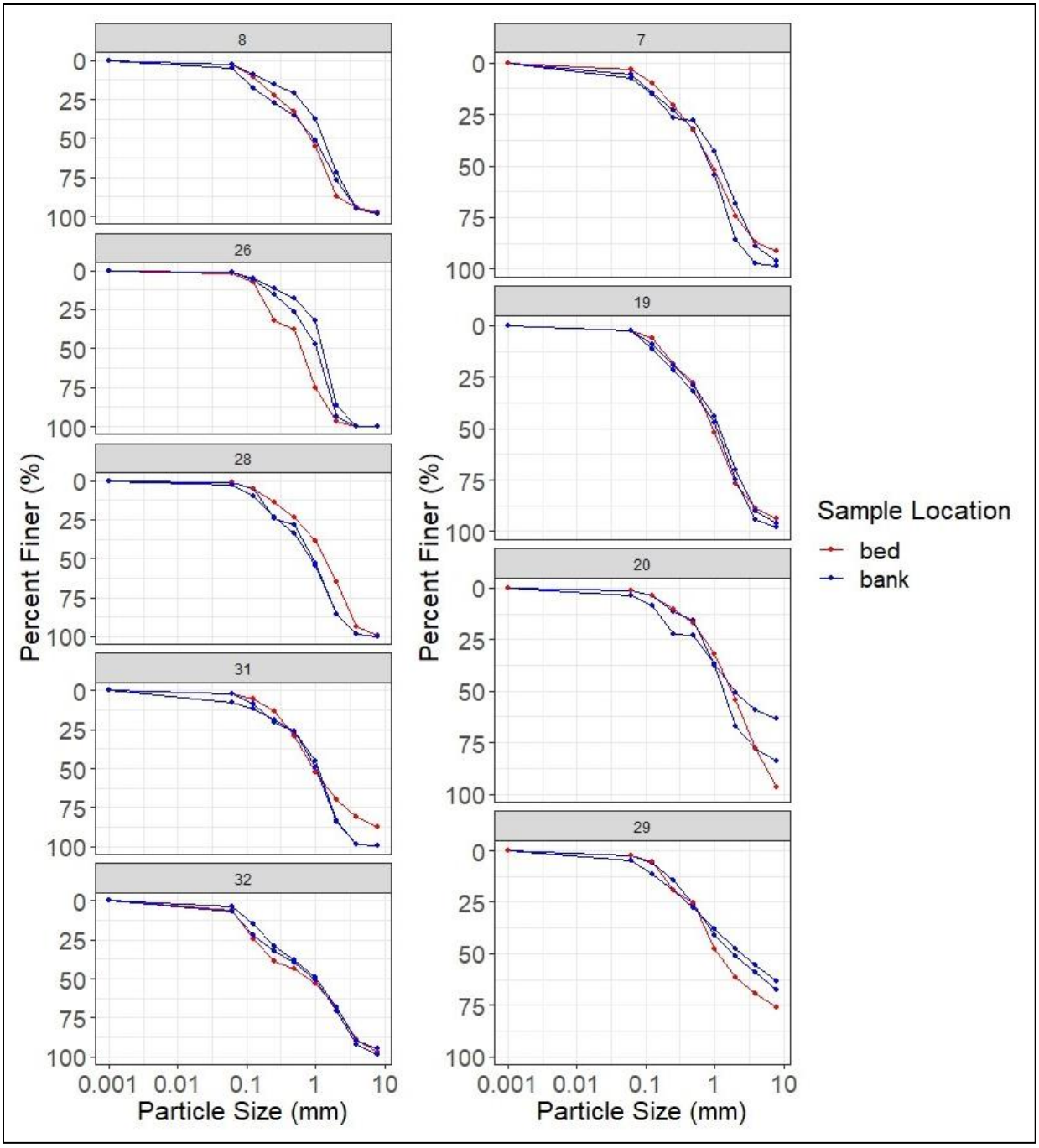

Figure 4.13. Grain size distribution plots for gullies with bed and banks made of cinders (left) and Moenkopi-sediments (right).

4.6.2 Catchment Data

Gully catchments included a cliff band of the Moenkopi Formation in 29 of the 35 measured gullies. The cliff band height ranged from 0.1 to 4.9 m, and generally created rockfall blocks in the lower portion of the catchment near gully heads (Figure 4.5). Catchments generally showed a low percentage of vegetation, but six gullies had a medium percentage of vegetation, and one gully with a high percentage of vegetation. Gully catchment areas ranged from 0.001 to 0.28 ha (Figure 4.14) and catchment slopes ranged from 0.05 to 0.4 percent. Median catchment area and slope were 0.02 ha and 0.2 percent, respectively. Infiltration data recorded in gully catchments have been reported above in Section 4.1.

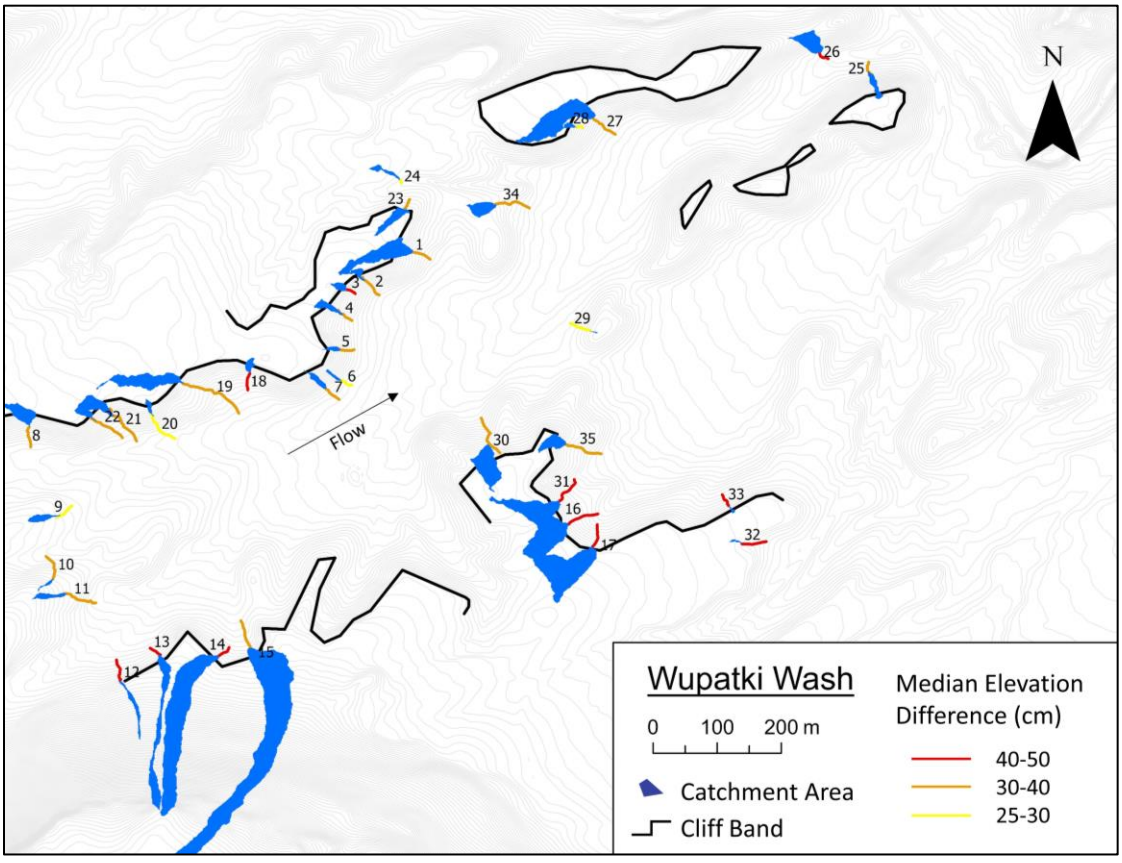

Figure 4.14. Map of gully catchment areas. The catchment area for gully 15 extends South beyond this image.

4.6.3 Slope-Area Analysis and Gully Prediction

I plotted our slope and catchment area data against Pederson et al. (2006) because their study was conducted nearby in Grand Canyon National Park (Figure 4.15). The variables a and b were found to be 0.10 and 0.13, respectively (Figure 4.15). While the general trend of smaller catchment areas show steeper slopes of Pederson et al. (2006) is visible in the data, the data indicate a much weaker relationship between slope and contributing area (R^2=0.28). As a result, a threshold slope for a given catchment area above which gully erosion occurs in Wupatki Wash has almost negligible utility.

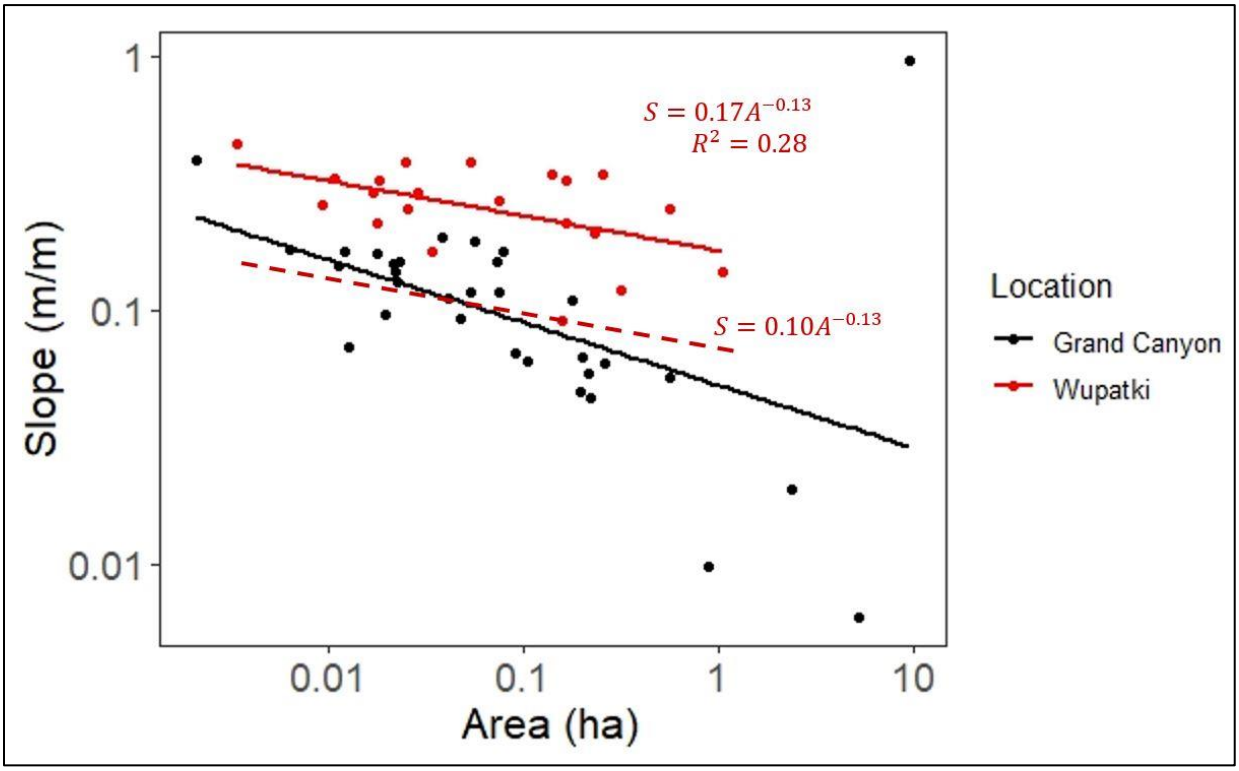

Figure 4.15. Slope-area relationship for 21 of the 35 measured gullies that all contained cliff bands and formed within cinders. The linear regression (solid red line) was shifted downward to the base of the data to create a gully erosion threshold (dashed red line). The values of the threshold coefficient and scaling exponent are 0.10 and 0.13, respectively. Data collected from Grand Canyon National Park are from Pederson et al. (2006).

4.6.4 Gully Change Analysis

4.6.4.1 Width and depth differences from cross-section data

All 35 measured gullies in Wupatki Wash deepened between 2016 to 2021, but only 14 gullies widened (Figure 3.16). Average width did not change significantly from 2016 to 2021 (p=0.77), but statistically significant changes in average depth occurred (p=<0.001). Six gullies incised on average more than 20 cm, 18 gullies incised more than 10 cm, and the rest showed less than 10 cm of incision (Figure 4.7, Figure 4.16). On average, gully 4 narrowed the most by 30 cm, and gully 11 widened the most by 40 cm.

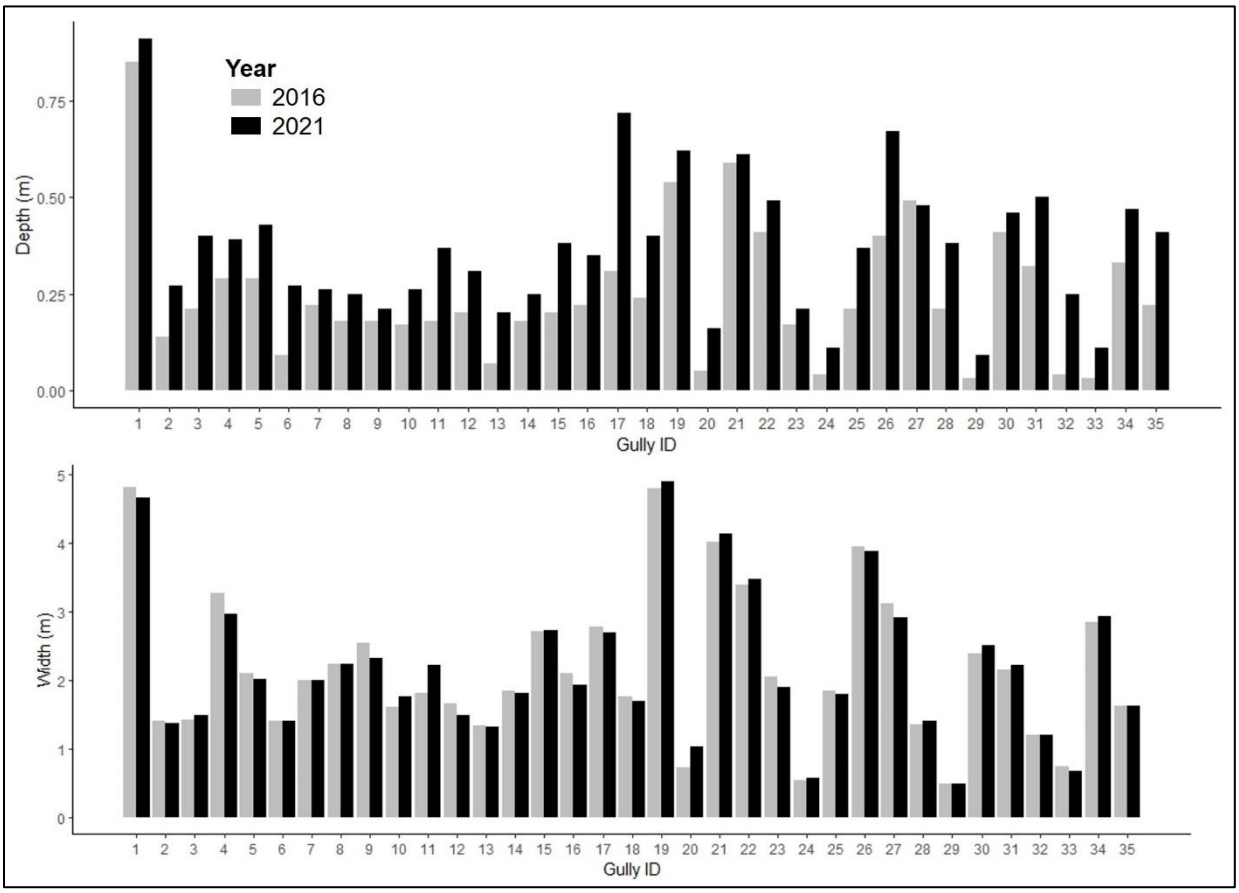

Figure 4.16. Barplots comparing gully geometries from 2016 to 2021. Gully depth (top) and width (bottom) are shown.

4.6.4.2 Median Elevation Difference (MED) and slope changes from longitudinal profiles

Consistent with the findings in cross-sectional changes, longitudinal profiles revealed negative MED for all measured gullies (Figure 4.17). Therefore, all measured gullies have eroded since 2016. Average topographic change was -36 cm and ranged from -52 cm to -25 cm. In addition, the gully slope decreased over the five-year period in 21 of the measured gullies (Figure 4.18). Gully 23 decreased in slope the most from 0.15 to 0.12, and gully 26 increased in slope the most from 0.14 to 0.15 (Figure 4.18).

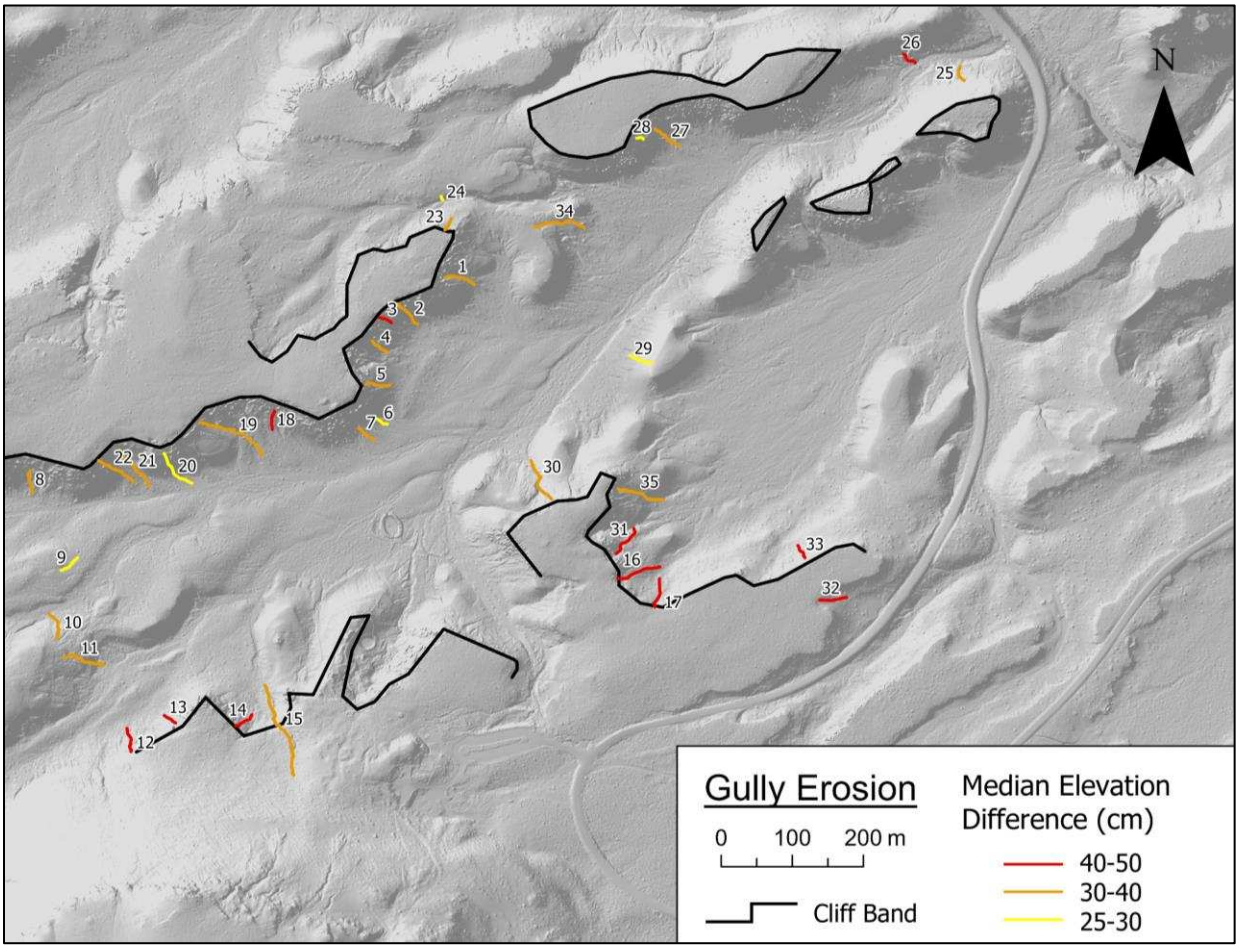

Figure 4.17. Change in median elevation from 2016 to 2021. All measured gullies had a negative MED suggesting widespread erosion.

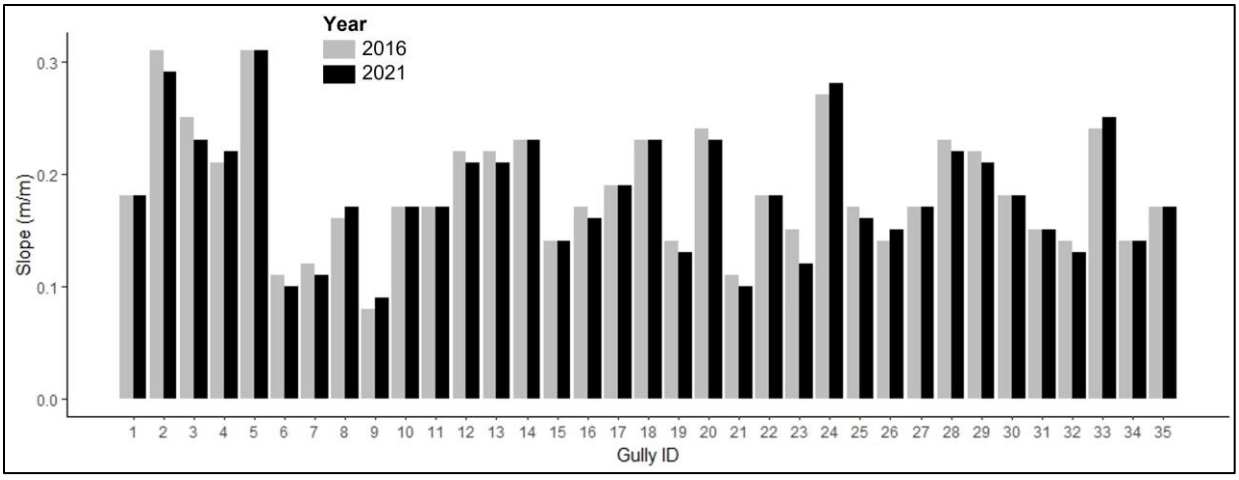

Figure 4.18. Gully slope changes from 2016 to 2021. The slope of gully 23 changed the most, decreasing from 0.15 to 0.12.

4.6.4.3 Median Elevation Difference (MED) and slope changes from SfM Analysis

Using SfM and DoD techniques, both incision and depositional processes were observed on the 0.17 ha hillslope in Wupatki Wash over a five-year time frame (Figure 4.19). Gullies experienced a maximum incision of 0.7 m and maximum deposition of 0.5 m, respectively. Gully incision generally ranged from 0.3 to 0.1 m, but one gully on the northwestern side of the study area filled with cinders with approximately 0.4 m of average deposition (Figure 4.19). Other depositional zones included the downstream regions of gullies and along gully banks.

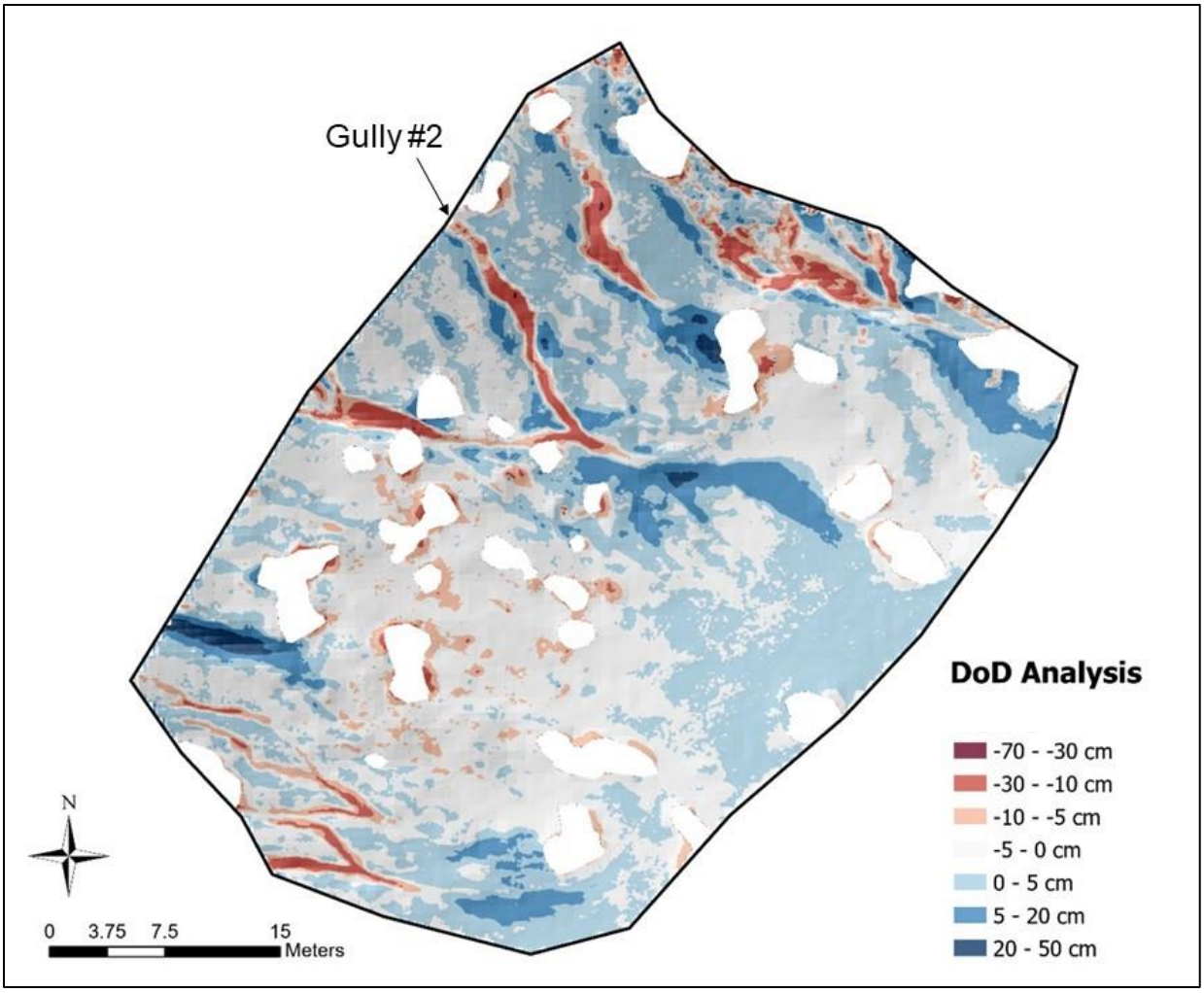

Figure 4.19. Results from a DEM of Differencing (DoD) analysis using 2016 aerial LiDAR and 2021 iPhone imagery. A semi-transparent hill shade of the 2016 DEM was used as the background. White polygons indicate where vegetation was manually removed from the imagery. Refer to Figure 3.7 for the location of the DoD analysis.

4.6.4.4 Archaeological Site Vulnerability Classification

Archaeological sites were classified for erosion vulnerability using geomorphic and geologic field data (Appendix B). Of the 54 sites, 22 were classified in the high category, 14 in the moderate category, and 12 in the low category (Appendix B, Table B1). Seven sites remain unclassified since they were not visited in the field and due to a lack of supporting information. Fifteen sites fell within the cliff band buffer and three sites fell within the measured gully buffer and were given a high vulnerability classification (Figure 4.10; Appendix B, Table B1). Gully

rankings and associated archaeological sites that fall within the measured gully buffer are summarized in Appendix B Table B2.

4.7 Discussion and Conclusions

4.7.1 Discussion

4.7.1.1 Erosion Threshold

The threshold model of erosion suggests that gully formation is controlled by the balance between erosion and deposition of sediment in a watershed, which is influenced by the characteristics of the contributing area. Larger contributing areas have a greater capacity to store water and generate runoff, which reduces the slope angle required to initiate gully erosion. As a result, gullies in larger contributing areas tend to have shallower slopes (Figure 4.15). Conversely, smaller contributing areas have less capacity to store water and generate runoff, which increases the slope angle required to initiate gully erosion. As a result, gullies in smaller contributing areas tend to have steeper slopes. In Wupatki Wash, however, the slope-area relationship is weak and gullies with smaller catchments degrade at a comparable rate as gullies with larger catchments. Thus, my hypothesis about the slope-area relationship was not supported by the data, and I did not find a threshold slope above which gully erosion occurs. I attribute the lack of a strong slope-area relationship found in other studies (e.g., Patton and Schumm, 1975; Montgomery and Dietrich, 1994; Pederson et al., 2006; Wu and Cheng, 2005) to lithological differences and, in particular, the high mobility and permeability of cinders. While the negative slope-area trend normally implies overland flow-driven processes, the weak trend seen at WUPA suggests subsurface flow (through the cinders) is influencing erosion (Vanderkerchove et al., 2000). The slope-area topographic relationship is not sufficient for explaining an erosion

threshold at WUPA. These data are comparable to the spread of contributing areas of Pederson et al. (2006), but the range of slopes of our data is much less (Figure 4.15).

4.7.1.2 Gully Morphology and Change Analysis

In Wupatki Wash, there is no evidence of head cut retreat in gullies. Gully heads are either abrupt at a cliff band or gradual after rockfall debris (Figure 4.5 and 4.6). In either case, gully heads remain fixed in position, while changes in gully slope (Figure 4.18) result from either erosion or aggradation. Gully heads remain fixed in position such that they cannot retreat because of the presence of the rockfall and cliff band in the catchment. Where gully heads are abrupt, the dominant process of gully erosion is pour-over that occurs from runoff over the cliff band (Figure 4.5 and 4.6). Slope breaks (gully knickpoints) did occur within gullies where Moenkopi sandstone outcropped, or Moenkopi colluvium accumulated within the gully bed. I found gullies to form primarily within cinder deposits with steeply sloped sides but not steep head cuts (Figure 3.6). Cross-sectional shape is a function of soil material type, and gully evolution (Thwaites et al., 2021). The gullies at WUPA are 'V' shaped (Figure 4.6), suggesting gullies form in materials with a high level of aggregate stability (Downes, 1946), and the gully is in the channel-eroding or stabilized stage of development (Ireland et al., 1939). However, models of gully development are typically based on weaker materials overlain by a more resistant material (Ireland et al., 1939; Schumm, 1960), which does not apply to WUPA. Generally, I observed gullies form within less-resistant cinders overlying more resistant silty sandstone (Figure 4.8). Cinders do not have a high level of aggregate stability, but gully banks did appear relatively stable at the cinder's angle of repose. The angle of repose of cinders is comparable to that of sand, around 30° (Porter, 1972). Bank collapse was evident in some gullies between patches of vegetation or where Moenkopi bedrock affected the bank. I did not examine gully

vegetation cover within the analysis because only one measured gully had a high amount of vegetation in the catchment and vegetation presence on gully banks was generally very minimal.

As opposed to channel widening from bank undercutting and failure (Pederson et al., 2006), gullies in Wupatki Wash have eroded primarily by channel incision (Figure 4.16 and 4.19). Some gullies contained pieces of Moenkopi colluvium or bedrock within the channel bed, however, which would limit further incision. All measured gullies were eroding, but as seen in Figure 4.19, some gullies at WUPA may be aggrading. Almost all measured gullies contained cliff bands, and I attribute gully erosion to runoff effects following rain events. Where cinders are present in catchments, runoff-generation is likely from saturation-excess overland flow due to the cinder's high permeability. Additionally, cinders are likely transported as a slurry and runoff over cliff bands into downstream gullies. Intermittent debris flows may occur given a sufficiently high rainfall intensity. The lower infiltration rate of Moenkopi-derived sediments suggests infiltration-excess overland flow likely leads to quicker runoff focused into gullies. Cinders are very loose, friable, non-cohesive, and mobile compared to Moenkopi-sediments. They are also slightly finer in grain size (Figure 4.13). Therefore, cinders are detached and transported more easily. For this reason, catchments composed of primarily cinders were found to have larger MEDs than those with surficial Moenkopi-sediments (Figure 4.17). This was an unexpected result, however, as I hypothesized Moenkopi-dominated catchments would increase the magnitude of runoff and MED. Thus, the second hypothesis was also not supported. Depth of cinders was not measured in the field, but I believe is an important control on erosion. Gullies with higher MEDs formed within thick cinder deposits. In addition to water erosion, cinders erode from aeolian processes, but these processes were not evaluated in this investigation.

4.7.1.3 Vulnerability Assessment

A 5-m buffered region around cliff band and measured gullies was used to designate archaeological sites as highly vulnerable to erosion, regardless of surficial catchment lithological properties. These sites experience direct impact from runoff over cliff bands and erosion was observed in all measured gullies. Three other sites (WUPA01455, WUPA01431, and WUPA01413) were given high vulnerability classifications because they are found on cinder hillslopes, which erode more readily compared to hillslopes composed of Moenkopi-sediments (Appendix B Table B1). Moderate and low classifications varied based on site setting, surficial geology, field notes, or field observations from an NPS archaeologist. These classifications were primarily based on lithology and site setting, but additional factors including flow accumulation, local slope, and presence of vegetation could be used to improve archaeological site classifications. Although a large amount of baseline geomorphic data was collected, the classification of archaeological sites was constrained by limited accessibility to measure specific gullies. This analysis could be improved by collecting aerial imagery and performing a large-scale, high spatial resolution landscape change detection analysis to further evaluate archaeological site vulnerability.

4.7.2 Conclusions

This study analyzed gully morphologic changes over a five-year period and classified archaeological sites based on vulnerability to gully erosion. Baseline geomorphological data collected in the summer of 2021 revealed an eroding landscape at WUPA. According to the coarse-scale analysis using longitudinal profile data, all measured gullies showed a negative MED, with a maximum of 50 cm of incision. These data were corroborated with cross-section data, where average gully depth was significantly greater in 2021 than 2016 for all measured

gullies ($p<0.001$). Although statistically significant changes in width were not found, these results provided insight into gully development and growth.

I linked catchment surficial geology to gully erosion, with unexpected results. Although water infiltrated quickly through the cinders, more erosion occurred in gullies with catchments predominantly covered with cinders. Additionally, cinders likely influence gully slope because the size of the catchment was weakly related to the gully head slope. In a semi-arid environment like WUPA, surficial geology, particularly the presence of Moenkopi Formation cliffs, heavily influences runoff processes and gully erosion. With changing precipitation patterns due to a warming climate, I recommend park managers focus monitoring efforts based on the geomorphic-controlled gully and archaeological site classifications. A total of 22 sites were classified as high vulnerability based on our analysis and flow diagram.

References

AgiSoft Metashape Professional (Version 1.6.1) (Software). 2020. Retrieved from https://www.agisoft.com/downloads/installer/.

Anderson, K. 2021. Wupatki Pueblo Geoarcheology Landscape Assessment.

ASTM International. 2018. Standard test methods for particle-size distribution (gradation) of soils using sieve analysis (ASTM D6913-17). ASTM International.

Aquaveo. 2022. WMS: Watershed modeling system [Computer software]. https://www.aquaveo.com/software/wms-watershed-modeling-system.

Baldwin, L., Cultural, M. A., and Program Manager, R. 2015. Archeological Excavation at WS1109, Structure 2 Wupatki National Monument Sunset Crater, Walnut Canyon and Wupatki National Monuments Cultural Resource Division FOIA Exempt: For Internal Use Only Archeological Excavation at WS1109 Structure 2 Wupatki National Monument.

Billingsley, G. H., S. S. Priest, and T. J. Felger. 2007. Geologic map of Wupatki National Monument and vicinity, Coconino County, Northern Arizona.

Decagon Devices. 2014. Mini Disk Infiltrometer Model S Manual.

Dóniz, J., C. Romero, J. Carmona, and A. García. 2011. Erosion of cinder cones in Tenerife by gully formation, Canary Islands, Spain. *Physical Geography* 32(2): 139–160. https://doi.org/10.2747/0272-3646.32.2.139

Downes, R. G. 1946. Tunnelling erosion in north-eastern Victoria. *Journal of the Council for Scientific and Industrial Research* 19: 283–292.

Emmett, W. W. 1968. Gully erosion, Fairbridge, R.W., ed., Encyclopedia of geomorphology. New York, Reinhold, p. 517-519.

Grattan, J., and R. Torrence. 2007. Living under the shadow: Cultural impacts of volcanic eruptions. Left Coast Press.

Gouma, M., G. J. van Wijngaarden, and S. Soetens. 2011. Assessing the effects of geomorphological processes on archaeological densities: A GIS case study on Zakynthos Island, Greece. *Journal of Archaeological Science* 38(10): 2714–2725. https://doi.org/10.1016/j.jas.2011.06.009

Hansen, M., J. Coles, K. A. Thomas, D. Cogan, M. Reid, J. Von Loh, and K. Schulz. 2004. USGS-NPS National Vegetation Mapping Program: Wupatki National Monument, Arizona, Vegetation Classification and Distribution Final Report.

Hanson, S. L. 2003. Roadside geology: Wupatki and Sunset Crater Volcano National Monuments. Arizona Geological Survey.

Higgins, C. G., B. R. Hill, and A. K. Lehre. 1990. Gully development. Special Paper of the Geological Society of America 252: 139–155. https://doi.org/10.1130/SPE252-p139

Howland, M. D., I. W. N. Jones, M. Najjar, and T. E. Levy. 2018. Quantifying the effects of erosion on archaeological sites with low-altitude aerial photography, structure from motion, and GIS: A case study from southern Jordan. *Journal of Archaeological Science* 90: 62–70. https://doi.org/10.1016/j.jas.2017.12.008

Hooten, J. A., M. H. Ort, and M. D. Elson. 2001. Origin of cinders in Wupatki National Monument. Technical Report No. 2001-12. Desert Archaeology, Inc., Tucson, Arizona.

Ireland, H. A. (Hubert Andrew), Sharpe, C. F. Stewart (Charles Farquharson Stewart), and D. H. Eargle. 1939. Principles of gully erosion in the Piedmont of South Carolina. Washington: U.S. Dept. of Agriculture.

Jones, C. A., and E. Church. 2020. Photogrammetry is for everyone: Structure-from-motion software user experiences in archaeology. *Journal of Archaeological Science: Reports*, 30. https://doi.org/10.1016/j.jasrep.2020.102261

Langbein, W. B., and S. A. Schumm. 1958. Yield of sediment in relation to mean annual precipitation. Transactions, American Geophysical Union 39: 1076–1084.

Montgomery, D. R., and W. E. Dietrich. 1994. Landscape dissection and contributing area-slope thresholds — Chapter 11. *In*: Kirkby, M. J. (Ed.). Process models and theoretical geomorphology. John Wiley & Sons Ltd, pp. 221–246.

NOAA. (n.d.). Percent Frequency Distribution Spreadsheet - 02-9542 (Flagstaff, AZ). National Weather Service. https://hdsc.nws.noaa.gov/hdsc/pfds/pfds_printpage.html?st=az&sta=02-9542&data=depth&units=english&series=pds#table

Patton, P. C., and S. A. Schümm. 1975. Gully erosion, northwestern Colorado: A threshold phenomenon. http://pubs.geoscienceworld.org/gsa/geology/article-pdf/3/2/88/3521842/i0091-7613-3-2-88.pdf

Pederson, J. L., P. A. Petersen, and J. L. Dierker. 2006. Gullying and erosion control at archaeological sites in Grand Canyon, Arizona. *Earth Surface Processes and Landforms* 31(4): 507–525. https://doi.org/10.1002/esp.1286

Petersen, P. A. 2003. Mitigation, monitoring, and geomorphology related to gully erosion of archaeological sites in Grand Canyon. MS Thesis, Utah State University, Logan, Utah.

Porter, S. 1972. Distribution, morphology, and size frequency of cinder cones on Mauna Kea Volcano, Hawaii. Geological Society of America Bulletin 83(12): 3607–3612. https://doi.org/10.1130/0016-7606(1972)83[3607:DMASFO]2.0.CO;2

Sha, G., G. Shu, Y. Xiping, et al. Mobile phone imaging point cloud modelling for 3D recording and measurement of small scenes of suspected fossil outcrops found in the field. *Geoheritage* 15: 33 (2023). https://doi.org/10.1007/s12371-022-00780-y

Sholtes, J. S., S. E. Yochum, J. A. Scott, and B. P. Bledsoe. 2018. Longitudinal variability of geomorphic response to floods. *Earth Surface Processes and Landforms* 43(15): 3099–3113. https://doi.org/10.1002/esp.4472

Schumm, S. A., M. D. Harvey, and C. C. Watson. 1984. Incised channels: Morphology, dynamics, and control. Littleton, Colo: Water Resources Publications.

Tarboton, D. 1997. A new method for the determination of flow directions and contributing areas in grid digital elevation models. *Water Resources Research* 33: 309–319.

Thwaites, R. N., A. P. Brooks, T. J. Pietsch, and J. R. Spencer. 2021. What type of gully is that? The need for a classification of gullies. *Earth Surface Processes and Landforms* (October 2020), 1–20. https://doi.org/10.1002/esp.5291

Vandekerckhove, L., J. Poesen, D. O. Wijdenes, J. Nachtergaele, C. Kosmas, M. J. Roxo, and T. De Figueiredo. 2000. Thresholds for gully initiation and sedimentation in Mediterranean Europe. *Earth Surface Processes and Landforms* 25(11): 1201–1220.

Westoby, M. J., J. Brasington, N. F. Glasser, M. J. Hambrey, and J. M. Reynolds. 2012. "Structure-from-Motion" photogrammetry: A low-cost, effective tool for geoscience applications. *Geomorphology* 179: 300–314. https://doi.org/10.1016/j.geomorph.2012.08.021

Wheaton, J. M., J. Brasington, S. E. Darby, and D. A. Sear. 2010. Accounting for uncertainty in DEMs from repeat topographic surveys: Improved sediment budgets. *Earth Surface Processes and Landforms* 35(2): 136–156. https://doi.org/10.1002/esp.1886

Wu, Y., and H. Cheng. 2005. Monitoring of gully erosion on the Loess Plateau of China using a global positioning system. *Catena* 63 154-166.

CHAPTER 5: CONCLUSION

A common thread to each chapter in this dissertation is the analysis of climatic influences including vegetation and lithology on geomorphic processes and channel form within drainage basins. Effective management of natural and cultural resources requires extensive spatial and temporal monitoring to assess geomorphic change. With this study I have provided guidance to restoration practitioners, natural resource managers, and cultural resource managers by highlighting the need for monitoring and providing critical datasets and tools to use for future monitoring efforts. Stream restoration following invasive plant treatment needs to put the river at the forefront and monitor the channel to assess geomorphic changes that may lead to unintended consequences after treatment. Long-term monitoring of channel change using the methods in Chapter 2 is inexpensive and would help to refine our understanding of IRV treatment. Treated reaches eroded more, but the magnitude and longevity of channel response is dependent on the flow regime and amount of revegetation. I suggested a management framework to assist restoration practitioners in determining how much of an increase in channel activity is desired after IRV treatment. Additionally, measuring multiple indices of channel change was important to evaluate how channels respond to invasive plant treatment. When I focused on BIBE in Chapter 3, I represented vegetation as dynamic and flexible to represent the complex structure and behavior of plants and created depth-varied roughness for hydraulic modeling. This was an important contribution to the literature because many studies assume plants behave similarly to rigid cylinders. Additionally, this multiscale analysis at the individual plant, plot, and reach scales was critical to accurately characterizing the vegetation, quantifying inundating discharges, and hydraulic modeling. Invasive giant cane was the most hydraulically rough, decreased conveyance the most, and likely increases sediment deposition and channel narrowing.

Removing giant cane from the hydraulic model suggested improved conveyance, but linking the geomorphic position at which giant cane and other native plants grow is important for understanding their roles in channel narrowing and conveyance. The findings presented from the vegetation analysis at BIBE will contribute to natural resource manager's understanding of vegetation-channel dynamics and inform post-treatment of giant cane monitoring. Lastly, findings from Chapter 4 suggested that effective monitoring of archaeological sites at WUPA relies on an understanding of the surficial processes contributing to erosion. I provided a multiscale analysis of topographic change and characterized local surficial sediments to assess archaeological site vulnerability to erosion, and found that in a predominantly eroding landscape, almost half of the archaeological sites fell into the high vulnerability category. Moreover, a gully catchment area-slope relation was not sufficient for predicting gully erosion due to the highly mobile and porous cinders which influenced gully slope. These findings essentially suggested that gullies with small catchments degrade comparable to those with large catchments. Ultimately, in terms of monitoring, most restoration projects remain un-evaluated (Rubin et al., 2017), or projects that currently use monitoring protocols could be improved. These studies highlight the need for monitoring, additional datasets and future work, and whether it is after treating invasive plants or evaluating cultural resource vulnerabilities, to shift the attention to understanding how local vegetation and lithologic factors influence channel morphology.

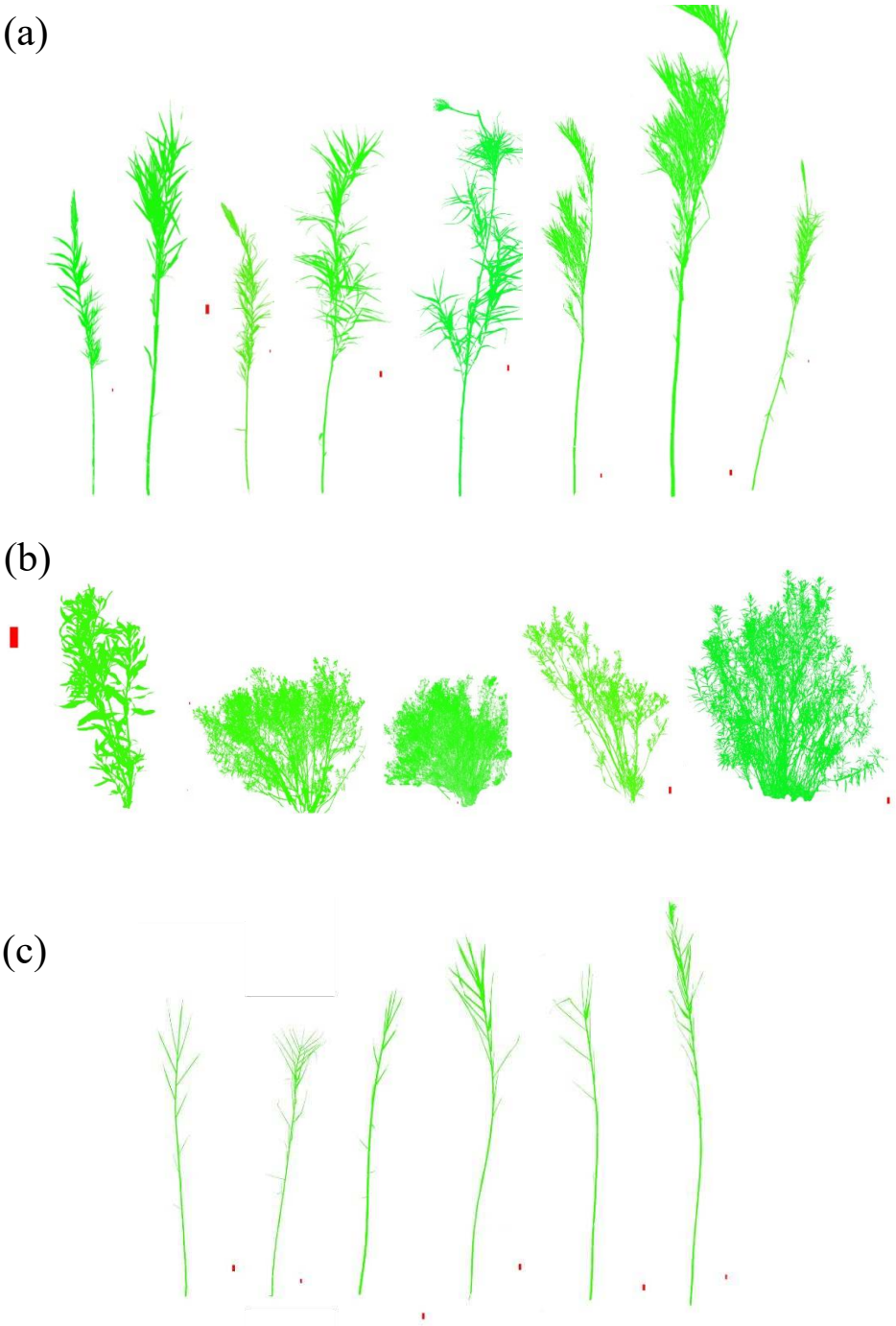

Figure A1. Edited plant photographs used to calculate upright frontal area of (a) giant cane, (b) baccharis, and (c) phragmites. Red scale bars were used to iteratively calculate frontal area with increasing plant height based on pixel size.

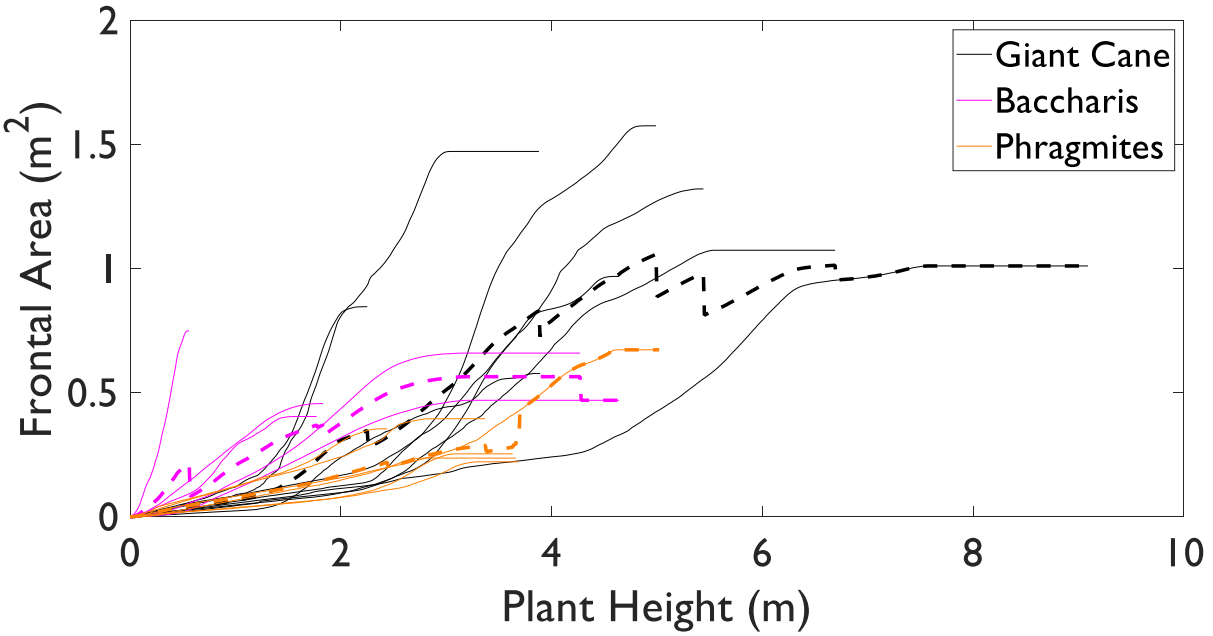

Figure A2. Non-normalized cumulative frontal area curves for individual upright plants. These curves are essentially the raw data from the photographs of plants taken with a red background.

Table A1. Stem count data for vegetation plots. These data were used to calculate upright and deflected frontal area at the plot scale.

PLOT ID	Measurement Height Above Ground (m)	Stem Diameter Class (cm)					Plot Area (m^2)
		0-0.5	0.5-1	1-2	3-4	>4	
'ARU_P1'	0.01	6	6	50	13	0	5.04
'ARU_P1'	1.2	75	14	64	8	0	5.04
'ARU_P2'	0.01	4	5	14	2	0	1
'ARU_P2'	1.2	51	10	9	0	0	1
'ARU_P3'	0.01	3	12	52	5	0	1
'ARU_P3'	1.2	59	46	24	0	0	1
'ARU_P4'	0.01	8	19	24	63	0	1
'ARU_P4'	1.2	21	35	37	32	0	1
'ARU_P5'	0.01	0	0	10	21	0	1
'ARU_P5'	1.2	0	9	13	17	0	1
'ARU_P6'	0.01	3	1	26	68	0	1
'ARU_P6'	1.2	12	8	20	45	0	1
'ARU_P7'	0.01	0	5	32	32	0	1
'ARU_P7'	1.2	34	41	25	21	0	1
'ARU_P8'	0.01	0	0	10	43	0	1

'ARU_P8'	1.2	15	6	10	36	0	1
'ARU_P9'	0.01	4	3	18	84	0	1
'ARU_P9'	1.2	2	1	51	32	0	1
'ARU_P10'	0.01	42	49	86	4	0	1
'ARU_P10'	1.2	406	52	42	0	0	1
'PHR_P1'	0.01	3	13	13	0	0	0.7
'PHR_P1'	1.2	1	16	6	0	0	0.7
'PHR_P2'	0.01	13	34	29	0	0	1
'PHR_P2'	1.2	12	14	30	0	0	1
'PHR_P3'	0.01	7	19	3	0	0	1
'PHR_P3'	1.2	0	6	18	0	0	1
'PHR_P4'	0.01	60	76	45	1	0	1
'PHR_P4'	1.2	105	35	17	0	0	1
'PHR_P5'	0.01	55	55	33	2	0	0.5
'PHR_P5'	1.2	71	41	7	0	0	0.5
'PHR_P6'	0.01	9	50	62	0	0	1
'PHR_P6'	1.2	47	51	31	0	0	1
'BAC_P1'	0.01	13	35	25	1	0	1
'BAC_P1'	1.2	129	96	15	0	0	1
'BAC_P2'	0.01	1	15	17	7	0	1
'BAC_P2'	1.2	75	34	18	0	0	1
'BAC_P3'	0.01	56	38	18	0	0	2.25
'BAC_P3'	0.7	137	21	3	0	0	2.25
'BAC_P4'	0.01	18	32	18	5	0	1
'BAC_P4'	0.4	37	22	15	1	0	1
'BAC_P5'	0.01	62	29	24	0	0	1
'BAC_P5'	0.9	252	30	15	0	0	1
'BAC_P6'	0.01	14	28	26	3	0	1
'BAC_P6'	0.7	55	34	10	0	0	1
'BAC_P7'	0.01	103	75	74	11	0	2.25
'BAC_P7'	1.6	163	65	27	0	0	2.25

Table A2. Plant characteristics used to calculate deflected frontal area and vegetation roughness.

Plant ID	Plant Height (m)	Average Stem Diameter (cm)	Flexural Rigidity ($N*m^2$)	Upright Frontal Area (m^2)	Canopy Area (m^2)
Baccharis1	0.57	0.0065	0.0073	0.0469	0.0625
Baccharis2	4.28	0.018	0.5792	4.2258	6.4
Baccharis3	4.65	0.0217	21.3305	5.3308	11.34
Baccharis4	1.78	0.0142	0.3594	0.3004	0.742
Baccharis5	1.84	0.0217	0.8833	0.9593	2.1
Phragmites1	2.45	0.0102	0.0736	0.0364	0.1024
Phragmites2	3.7	0.015	0.5309	0.0910	0.4096
Phragmites3	3.67	0.0108	0.06884	0.0534	0.225
Phragmites4	3.64	0.0108	0.2042	0.0915	0.36
Phragmites5	3.38	0.0092	0.2788	0.0485	0.1225
Phragmites6	5.03	0.013	0.8956	0.1617	0.2401
Arundo1	5.4	0.0222	9.85592	0.5366	0.406
Arundo2	2.25	0.0133	0.36897	0.1255	0.1482
Arundo3	6.65	0.0203	2.77139	0.5932	0.552
Arundo4	3.85	0.0121	0.47422	0.2872	0.195
Arundo5	3.85	0.0173	1.84670	0.5086	0.88
Arundo6	4.95	0.0189	2.83816	0.4767	0.3025
Arundo7	4.6	0.0234	3.90578	0.6358	0.6561
Arundo8	9.05	0.024	2.75333	0.6473	0.64

Table A3. Plot characteristics used to calculate deflected frontal area and vegetation roughness.

Plot ID	Plot Height[A] (m)	Flexural Rigidity ($N*m^2$)	Cumulative Upright Frontal Area (m^2)	Buoyancy	Plot Area (m^2)
BAC_P1	2.6	0.579	2.0614	0	1
BAC_P2	3	0.579	1.4132	0	1
BAC_P3	1.36	0.579	0.6111	0	2.25
BAC_P4	2.7	0.579	0.8303	0	1
BAC_P5	3.3	0.579	2.1062	0	1
BAC_P6	2.2	0.579	0.8478	0	1
BAC_P7	3.15	0.579	3.849	0	2.25
PHR_P1	3.645	0.2415	0.5668	0	0.7
PHR_P2	3.645	0.2415	1.4982	0	1
PHR_P3	3.645	0.2415	0.6963	0	1
PHR_P4	3.645	0.2415	2.2746	0	1
PHR_P5	3.645	0.2415	1.7368	0	0.5
PHR_P6	3.645	0.2415	2.5528	0	1
ARU_P1	5.075	2.76	4.5184	0	5.04
ARU_P2	5.075	2.76	1.0494	0	1

ARU_P3	5.075	2.76	2.7861125	0	1
ARU_P4	5.075	2.76	6.10485	0	1
ARU_P5	5.075	2.76	2.4340125	0	1
ARU_P6	5.075	2.76	5.8953	0	1
ARU_P7	5.075	2.76	4.4431375	0	1
ARU_P8	5.075	2.76	4.2043125	0	1
ARU_P9	5.075	2.76	6.1154375	0	1
ARU_P10	5.075	2.76	6.308575	0	1

[A]Plot heights were not recorded, and so average plant height was used.

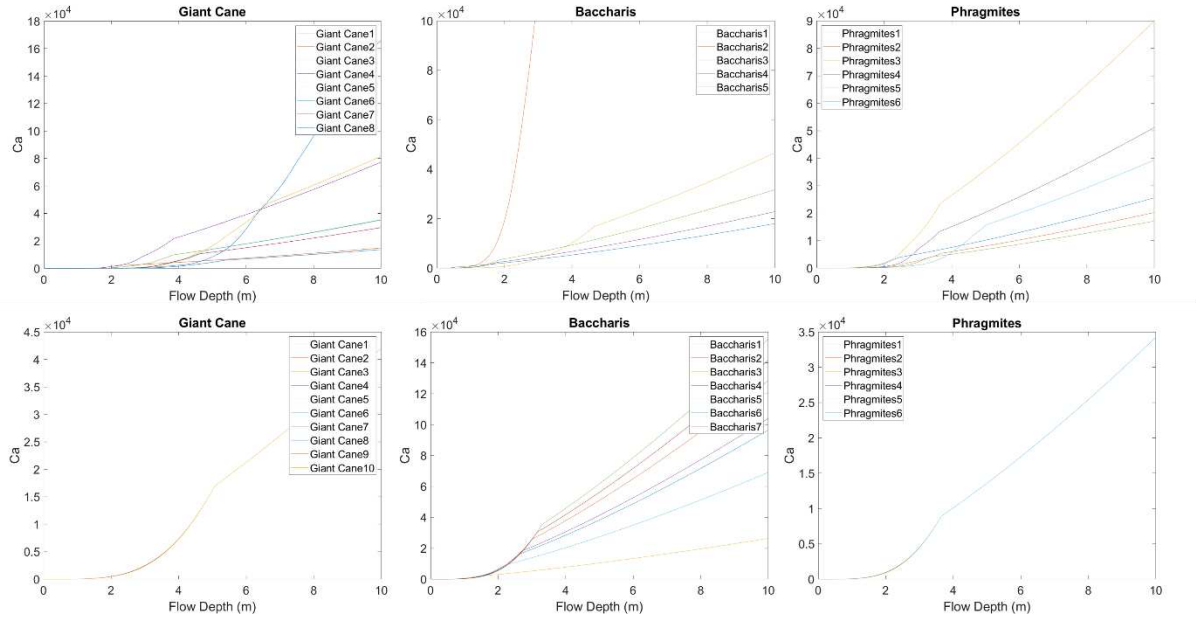

Figure A3. Cauchy versus flow depth at the plant scale (top) and plot scale (bottom) for giant cane, baccharis, and phragmites.

Table A4. Elevation statistics for each plant species-geomorphic surface combination with respect to the 2018 low-water surface elevation.

Dataset	Area of plant type on each surface (m^2)	Mean (m)	Median (m)	Standard Deviation (m)	Skewness
Phragmites-FS3	0	0	0	0	--
Phragmites-FS2	1141	2.265	2.090	1.257	0.460
Phragmites-FS1	1537	1.398	1.060	1.221	0.709
Phragmites-AC	260	0.253	0.134	0.383	4.194

Baccharis-FS3	0	0	0	0	--
Baccharis-FS2	3254	2.468	2.384	1.677	0.619
Baccharis-FS1	5785	2.216	2.297	1.160	-0.078
Baccharis-AC	4997	1.362	1.227	0.826	0.705
Giant cane-FS3	0	0	0	0	--
Giant cane-FS2	3954	4.803	4.873	1.880	-0.221
Giant cane-FS1	2370	2.917	3.106	1.578	-0.136
Giant cane-AC	210	0.420	0.274	0.443	2.239
Elevation-FS3	6438[a]	11.735	11.801	1.963	0.429
Elevation-FS2	59077[a]	6.779	7.238	2.396	-0.654
Elevation-FS1	28441[a]	3.038	3.212	1.375	-0.336
Elevation-AC	32218[a]	0.814	0.358	0.876	1.478

[a]Total area of each geomorphic surface.

Table A5. Summary statistics of flow depth and velocity within vegetated regions across all simulated discharges.

Discharge_Variable_Simulation	Mean	Median	Standard Deviation	Maximum	Minimum
Q100_Vel_GC	0.312077	0.272	0.247729	1.424	0
Q100_Vel_Bac	0.567825	0.569	0.362862	1.631	0
Q100_Vel_Phrag	0.425848	0.397	0.304749	1.545	0
Q100_Vel_BedOnly	0.885605	0.961	0.462617	1.95	0
Q100_Vel_AllPlants	0.498968	0.492	0.32608	1.611	0
Q100_Vel_NoGC	0.551901	0.526	0.374155	1.837	0
Q200_Vel_GC	0.492453	0.459	0.341589	2.109	0
Q200_Vel_Bac	0.837216	0.855	0.450754	2.371	0
Q200_Vel_Phrag	0.654854	0.646	0.401472	2.226	0
Q200_Vel_BedOnly	1.192436	1.274	0.538967	2.64	0
Q200_Vel_AllPlants	0.756436	0.773	0.422915	2.318	0
Q200_Vel_NoGC	0.821088	0.817	0.463773	2.483	0
Q500_Vel_GC	0.939374	0.919	0.488896	3.259	0
Q500_Vel_Bac	1.350075	1.381	0.547172	3.822	0
Q500_Vel_Phrag	1.155789	1.162	0.529946	3.451	0
Q500_Vel_BedOnly	1.590866	1.643	0.642641	5.23	0
Q500_Vel_AllPlants	1.2227	1.241	0.553448	3.169	0
Q500_Vel_NoGC	1.360331	1.379	0.534397	3.643	0
Q1000_Vel_GC	1.433167	1.446	0.530681	4.058	0
Q1000_Vel_Bac	1.775657	1.776	0.556641	4.541	0
Q1000_Vel_Phrag	1.627168	1.629	0.536243	4.342	0
Q1000_Vel_BedOnly	1.912006	1.905	0.669608	4.768	0
Q1000_Vel_AllPlants	1.622818	1.672	0.590701	4.424	0
Q1000_Vel_NoGC	1.811312	1.7915	0.563641	4.575	0

Q1490_Vel_GC	1.747858	1.735	0.527498	5.051	0.057
Q1490_Vel_Bac	2.024788	1.996	0.658503	5.547	0.07
Q1490_Vel_Phrag	1.919019	1.92	0.579524	5.358	0.098
Q1490_Vel_BedOnly	2.10325	2.065	0.815463	5.739	0.114
Q1490_Vel_AllPlants	1.912737	1.934	0.62824	5.428	0.165
Q1490_Vel_NoGC	2.038917	1.987	0.694256	5.575	0.048
Q100_depth_GC	1.176353	1.152	0.871129	4.104	-0.93
Q100_depth_Bac	1.124697	1.114	0.84294	3.961	-1.004
Q100_depth_Phrag	1.150453	1.132	0.857077	4.029	-0.954
Q100_depth_BedOnly	1.09676	1.103	0.814189	3.861	-1.013
Q100_depth_AllPlants	1.142631	1.125	0.852607	4.018	-0.967
Q100_depth_NoGC	1.130347	1.121	0.844479	3.964	-1.013
Q200_depth_GC	2.028151	2.081	1.157843	5.362	-0.92
Q200_depth_Bac	1.879783	1.9075	1.112461	5.099	-0.948
Q200_depth_Phrag	1.950372	1.988	1.133373	5.218	-1.027
Q200_depth_BedOnly	1.778831	1.793	1.083925	4.945	-0.986
Q200_depth_AllPlants	1.921301	1.953	1.124744	5.184	-0.974
Q200_depth_NoGC	1.888417	1.92	1.116131	5.109	-0.933
Q500_depth_GC	4.06265	4.318	1.626139	7.824	-1.096
Q500_depth_Bac	3.746058	3.956	1.577688	7.408	-1.125
Q500_depth_Phrag	3.884466	4.117	1.59732	7.584	-1.066
Q500_depth_BedOnly	3.600475	3.784	1.562702	7.199	-0.999
Q500_depth_AllPlants	3.826999	4.056	1.59386	7.524	-1.073
Q500_depth_NoGC	3.764612	3.979	1.589244	7.419	-1.104
Q1000_depth_GC	6.496217	6.897	2.010727	10.493	-1.234
Q1000_depth_Bac	6.112315	6.432	1.993266	10.027	-1.102
Q1000_depth_Phrag	6.259709	6.61	2.004474	10.209	-1.376
Q1000_depth_BedOnly	5.962668	6.256	1.989932	9.852	-0.683
Q1000_depth_AllPlants	6.213992	6.569	2.00481	10.179	-1.384
Q1000_depth_NoGC	6.118997	6.4365	1.993629	10.034	-1.087
Q1490_depth_GC	8.735732	9.131	2.009485	12.729	1.007
Q1490_depth_Bac	8.366756	8.675	2.010405	12.3	0.818
Q1490_depth_Phrag	8.505523	8.838	2.00673	12.458	0.887
Q1490_depth_BedOnly	8.239536	8.512	2.018722	12.169	0.752
Q1490_depth_AllPlants	8.472154	8.799	2.007095	12.44	0.875
Q1490_depth_NoGC	8.370407	8.672	2.011538	12.307	0.833

Table A6. Summary statistics of flow depth and velocity within the active channel across all simulated discharges.

Discharge_Variable_Simulation	Mean	Median	Standard Deviation	Maximum	Minimum
Q100_Vel_GC	1.340162	1.363	0.241166	1.959	0.173
Q100_Vel_Bac	1.335808	1.346	0.189587	1.89	0.326

Q100_Vel_Phrag	1.338503	1.359	0.212102	1.885	0.319
Q100_Vel_BedOnly	1.333462	1.352	0.206858	1.865	0.324
Q100_Vel_AllPlants	1.335932	1.35	0.192847	1.856	0.326
Q100_Vel_NoGC	1.33115	1.33	0.175157	1.888	0.317
Q200_Vel_GC	1.600366	1.618	0.293626	2.34	0.281
Q200_Vel_Bac	1.596647	1.6	0.216631	2.222	0.484
Q200_Vel_Phrag	1.599016	1.611	0.249422	2.276	0.366
Q200_Vel_BedOnly	1.588659	1.596	0.198326	2.256	0.494
Q200_Vel_AllPlants	1.593201	1.596	0.235798	2.228	0.485
Q200_Vel_NoGC	1.593329	1.608	0.223615	2.177	0.485
Q500_Vel_GC	1.939373	1.967	0.344356	2.802	0.31
Q500_Vel_Bac	1.934991	1.935	0.246235	2.897	0.308
Q500_Vel_Phrag	1.938679	1.956	0.282426	2.686	0.539
Q500_Vel_BedOnly	1.941282	1.919	0.226098	3.707	1.064
Q500_Vel_AllPlants	1.947181	1.959	0.272174	2.605	0.438
Q500_Vel_NoGC	1.930674	1.924	0.252186	3.003	0.315
Q1000_Vel_GC	2.151035	2.12	0.322349	3.691	1.165
Q1000_Vel_Bac	2.156479	2.148	0.272182	4.061	1.306
Q1000_Vel_Phrag	2.157792	2.151	0.282727	3.899	1.242
Q1000_Vel_BedOnly	2.158806	2.125	0.289557	4.248	1.387
Q1000_Vel_AllPlants	2.179612	2.18	0.288379	3.948	1.215
Q1000_Vel_NoGC	2.143234	2.133	0.275172	4.076	1.32
Q1490_Vel_GC	2.307029	2.303	0.32463	4.41	1.299
Q1490_Vel_Bac	2.309179	2.316	0.314236	4.76	1.426
Q1490_Vel_Phrag	2.311484	2.323	0.303686	4.616	1.371
Q1490_Vel_BedOnly	2.319357	2.316	0.352088	4.903	1.317
Q1490_Vel_AllPlants	2.347786	2.353	0.310175	4.648	1.329
Q1490_Vel_NoGC	2.297869	2.306	0.322175	4.772	1.362
Q100_depth_GC	2.213684	2.215	0.505238	4.406	0.669
Q100_depth_Bac	2.110389	2.124	0.499269	4.31	0.511
Q100_depth_Phrag	2.162272	2.171	0.501454	4.36	0.588
Q100_depth_BedOnly	2.025009	2.04	0.497948	4.218	0.389
Q100_depth_AllPlants	2.14707	2.152	0.500444	4.341	0.567
Q100_depth_NoGC	2.116893	2.133	0.498563	4.334	0.514
Q200_depth_GC	3.496355	3.495	0.504764	5.692	1.952
Q200_depth_Bac	3.294725	3.308	0.493009	5.5	1.656
Q200_depth_Phrag	3.390893	3.398	0.496527	5.594	1.796
Q200_depth_BedOnly	3.151708	3.178	0.494204	5.355	1.446
Q200_depth_AllPlants	3.351649	3.353	0.494725	5.547	1.734
Q200_depth_NoGC	3.307099	3.323	0.491996	5.532	1.67
Q500_depth_GC	6.010141	6.004	0.517088	8.216	4.483
Q500_depth_Bac	5.67398	5.7	0.510486	7.902	3.674
Q500_depth_Phrag	5.816312	5.826	0.502172	8.038	4.191

Q500_depth_BedOnly	5.49823	5.528	0.522684	7.75	3.715
Q500_depth_AllPlants	5.749169	5.764	0.503902	7.97	4.071
Q500_depth_NoGC	5.680508	5.71	0.507619	7.932	3.984
Q1000_depth_GC	8.953623	8.955	0.51823	10.634	7.513
Q1000_depth_Bac	8.573986	8.605	0.520804	10.267	6.915
Q1000_depth_Phrag	8.723756	8.749	0.509248	10.399	7.154
Q1000_depth_BedOnly	8.423605	8.444	0.548046	10.135	6.671
Q1000_depth_AllPlants	8.67923	8.705	0.511928	10.375	7.063
Q1000_depth_NoGC	8.580447	8.612	0.522275	10.29	6.913
Q1490_depth_GC	11.19722	11.207	0.513146	12.824	9.71
Q1490_depth_Bac	10.84018	10.867	0.538986	12.515	9.135
Q1490_depth_Phrag	10.97405	11.004	0.518645	12.63	9.353
Q1490_depth_BedOnly	10.71849	10.733	0.569526	12.419	8.929
Q1490_depth_AllPlants	10.94149	10.974	0.521197	12.616	9.29
Q1490_depth_NoGC	10.8441	10.869	0.541908	12.532	9.128

Table A7. Summary statistics of flow depth and velocity within the unvegetated floodplain across all simulated discharges.

Discharge_Variable_Simulation	Mean	Median	Standard Deviation	Maximum	Minimum
Q100_Vel_GC	0.532716	0.4	0.490989	1.639	0
Q100_Vel_Bac	0.666683	0.708	0.529986	1.665	0
Q100_Vel_Phrag	0.590968	0.526	0.505662	1.649	0
Q100_Vel_BedOnly	0.83224	1.003	0.58111	1.778	0
Q100_Vel_AllPlants	0.624189	0.585	0.524598	1.674	0
Q100_Vel_NoGC	0.674932	0.7075	0.528875	1.682	0
Q200_Vel_GC	0.677274	0.676	0.505447	2.309	0
Q200_Vel_Bac	0.811234	0.882	0.545932	2.14	0
Q200_Vel_Phrag	0.734056	0.788	0.52054	2.101	0
Q200_Vel_BedOnly	0.957388	1.062	0.635455	2.482	0
Q200_Vel_AllPlants	0.779157	0.8515	0.536024	2.005	0
Q200_Vel_NoGC	0.807329	0.872	0.546573	2.155	0
Q500_Vel_GC	1.099968	1.198	0.611288	2.655	0
Q500_Vel_Bac	1.230598	1.376	0.647318	2.504	0
Q500_Vel_Phrag	1.158441	1.294	0.628877	2.606	0
Q500_Vel_BedOnly	1.303994	1.467	0.710389	4.275	0
Q500_Vel_AllPlants	1.180242	1.267	0.647497	2.837	0
Q500_Vel_NoGC	1.240941	1.397	0.643597	3.268	0
Q1000_Vel_GC	1.062432	1.134	0.749997	2.656	0
Q1000_Vel_Bac	1.157606	1.306	0.806616	2.595	0
Q1000_Vel_Phrag	1.104934	1.223	0.776668	2.588	0
Q1000_Vel_BedOnly	1.209584	1.361	0.86997	3.236	0
Q1000_Vel_AllPlants	1.09116	1.193	0.798156	2.638	0

Q1000_Vel_NoGC	1.168481	1.333	0.806051	2.683	0
Q1490_Vel_GC	1.182577	1.259	0.778253	2.86	0
Q1490_Vel_Bac	1.265666	1.36	0.851087	3.469	0
Q1490_Vel_Phrag	1.224817	1.319	0.813812	3.041	0
Q1490_Vel_BedOnly	1.295854	1.364	0.916359	3.923	0
Q1490_Vel_AllPlants	1.203585	1.272	0.830268	2.825	0
Q1490_Vel_NoGC	1.275314	1.383	0.859041	3.641	0
Q100_depth_GC	0.670731	0.567	0.727492	3.408	-2.134
Q100_depth_Bac	0.647194	0.5695	0.704472	3.265	-1.408
Q100_depth_Phrag	0.659023	0.57	0.715543	3.333	-1.335
Q100_depth_BedOnly	0.651711	0.608	0.685953	3.167	-1.527
Q100_depth_AllPlants	0.653613	0.568	0.712221	3.322	-1.367
Q100_depth_NoGC	0.653293	0.581	0.706959	3.269	-1.416
Q200_depth_GC	1.132573	0.975	1.003133	4.667	-2.564
Q200_depth_Bac	1.071166	0.918	0.965653	4.422	-2.707
Q200_depth_Phrag	1.098193	0.941	0.983765	4.523	-2.731
Q200_depth_BedOnly	1.025155	0.867	0.941577	4.275	-1.84
Q200_depth_AllPlants	1.087859	0.93	0.975092	4.49	-2.81
Q200_depth_NoGC	1.075963	0.919	0.969037	4.458	-2.715
Q500_depth_GC	2.479652	2.423	1.551513	7.159	-6.426
Q500_depth_Bac	2.229266	2.117	1.478132	6.84	-6.751
Q500_depth_Phrag	2.333255	2.25	1.509716	6.978	-4.381
Q500_depth_BedOnly	2.117545	1.967	1.450668	6.683	-6.601
Q500_depth_AllPlants	2.290167	2.194	1.498894	6.908	-6.451
Q500_depth_NoGC	2.239988	2.119	1.488278	6.869	-6.497
Q1000_depth_GC	3.484745	3.802	2.660535	10.039	-10.782
Q1000_depth_Bac	3.285327	3.6275	2.529324	9.672	-8.095
Q1000_depth_Phrag	3.351225	3.669	2.58569	9.815	-8.95
Q1000_depth_BedOnly	3.202872	3.558	2.493465	9.535	-7.878
Q1000_depth_AllPlants	3.335056	3.659	2.562322	9.785	-7.901
Q1000_depth_NoGC	3.291995	3.6345	2.530385	9.689	-8.12
Q1490_depth_GC	4.787774	5.243	3.395798	12.249	-13.689
Q1490_depth_Bac	4.578144	4.982	3.236825	11.919	-12.367
Q1490_depth_Phrag	4.657602	5.051	3.290794	12.041	-13.283
Q1490_depth_BedOnly	4.505744	4.888	3.189511	11.821	-11.738
Q1490_depth_AllPlants	4.633573	5.0255	3.282821	12.026	-13.351
Q1490_depth_NoGC	4.582904	4.982	3.237146	11.933	-12.391

SA1. Derivation of vegetation roughness for use in SRH-2D modeling

The reduction in bed shear stress due to vegetation (F_τ) was set equal to the vegetation form drag (F_D) to derive the equation for vegetation roughness (n_v).

$$F_\tau = F_D$$

$$\rho g H S = \frac{1}{2}\rho C_D \left(\frac{A_{eff}}{A_c}\right)\textcircled{V}^2 \quad \rightarrow \quad V = \frac{H^{\frac{2}{3}} S^{\frac{1}{2}}}{n}$$

$$gHS = \frac{1}{2} C_D \left(\frac{A_{eff}}{A_c}\right)\left(\frac{H^{\frac{2}{3}} S^{\frac{1}{2}}}{n}\right)^2$$

$$gHS = \frac{1}{2} C_D \left(\frac{A_{eff}}{A_c}\right)\left(\frac{H^{\frac{4}{3}} S}{n^2}\right)$$

$$n^2 = \frac{\frac{1}{2} C_D \left(\frac{A_{eff}}{A_c}\right) H^{\frac{4}{3}}}{gH}$$

$$n_v = \sqrt{\left(\frac{A_{eff}}{A_c}\right)\frac{C_D H^{\frac{1}{3}}}{2g}}$$

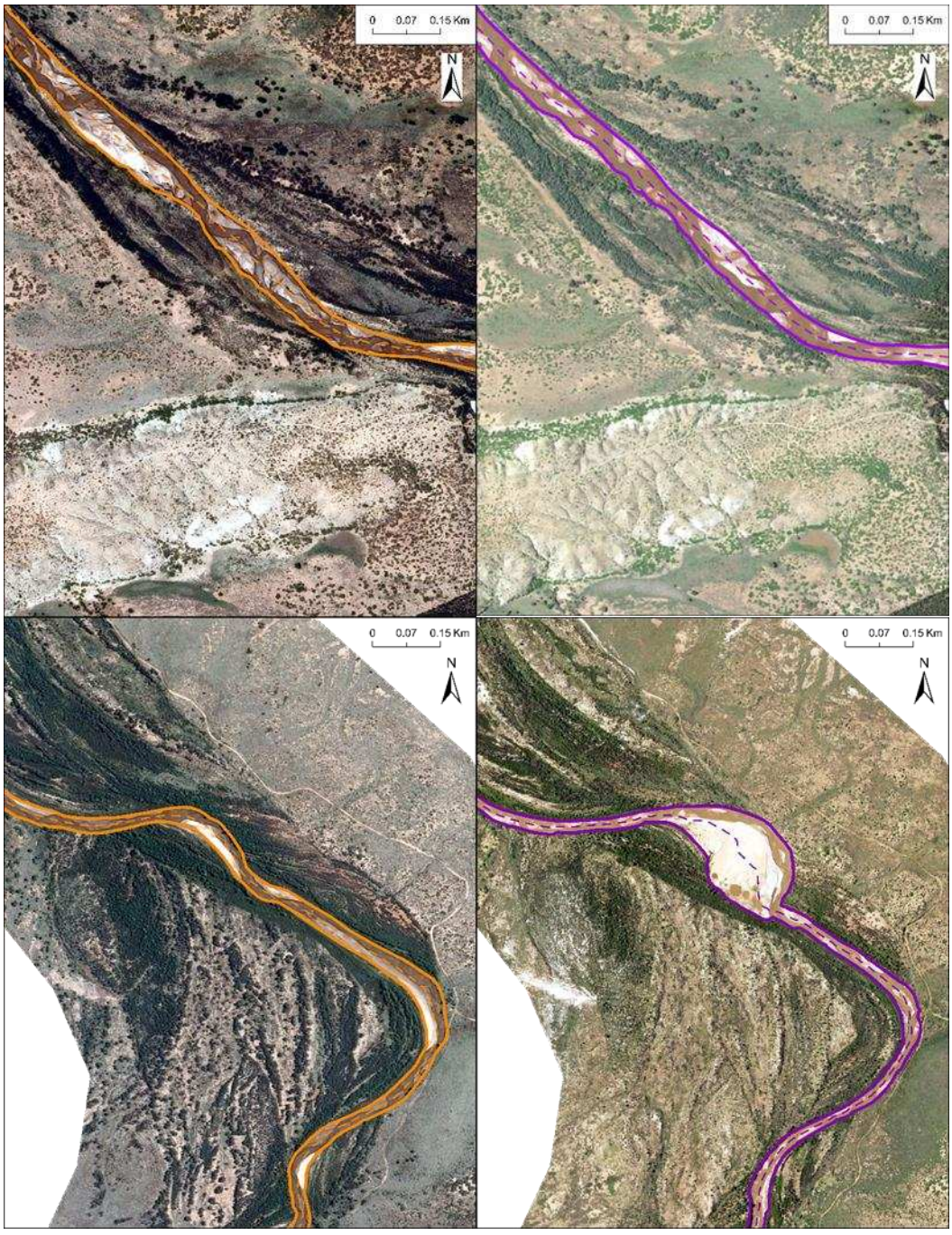

Figure B1. Example of active channel delineations at the untreated (top) and treated (bottom) reaches of the Pecos River NM site. This example highlights a portion of the reach where a large change in channel morphology occurred due to IRV treatment. The channel was delineated and then a centerline was mapped using pre-treated imagery in 2009 (left) and post-treated imagery in 2020 (right).

APPENDIX C: CHAPTER FOUR SUPPLEMENTARY MATERIALS

Table C1. Archaeological site vulnerability assessment based on proximity to cliff bands and measured gullies.

Site Number	Site Type	Location	Vulnerability
WUPA01107	Structure	Within cliff band buffer	High
WUPA01108	Structure	Within gully buffer	High
WUPA01109	Structure	Within cliff band buffer	High
WUPA01110	Structure	Within cliff band buffer	High
WUPA01380	Structure	Unknown; did not visit	Unclassified
WUPA01381	Structure	Within gully buffer	High
WUPA01383	Habitation, Protected	Below cliff band	High
WUPA01384	Habitation, Protected	Within cliff band buffer	High
WUPA01387	Habitation, Protected	Within cliff band buffer	High
WUPA01388	Structure, Other	Moenkopi hillslope	Moderate
WUPA01395	Habitation, Open Air	Mesa top	Low
WUPA01400	Habitation, Open Air	Moenkopi hillslope	Moderate
WUPA01404	Structure	Moenkopi hillslope	Low
WUPA01406	Structure	Moenkopi hillslope	Moderate
WUPA01407	Structure	Moenkopi hillslope	Moderate
WUPA01410	Other	At downstream end of gully 30	Moderate
WUPA01412	Other	Unknown; did not visit	Unclassified
WUPA01413	Structure	Cinder hillslope	High
WUPA01414	Structure	Within cliff band buffer	High
WUPA01418	Structure	Moenkopi hillslope	Moderate
WUPA01419	Structure, Other	Mesa top	Low

Site Number	Site Type	Location	Vulnerability
WUPA01430	Habitation, Open Air	On very small hillslope	Low
WUPA01431	Structure	Cinder hillslope	High
WUPA01433	Structure	Moenkopi hillslope	Moderate
WUPA01434	Habitation	Moenkopi hillslope	Moderate
WUPA01439	Structure, Other	Moenkopi hillslope	Low
WUPA01442	Structure	Mesa top	Low
WUPA01444	Structure	Moenkopi hillslope	Moderate
WUPA01445	Habitation	Within cliff band buffer	High
WUPA01446	Structure	Within cliff band buffer	High
WUPA01447	Habitation	Within gully buffer	High
WUPA01448	Habitation	Moenkopi hillslope	Moderate
WUPA01448	Habitation	Moenkopi hillslope	Moderate
WUPA01449	Structure	Moenkopi hillslope	Moderate
WUPA01454	Structure	Moenkopi hillslope	Moderate
WUPA01455	Structure, Other	On cinder hillslope beneath rock fall	High*
WUPA01457	Habitation, Protected	Within cliff band buffer	High
WUPA01458	Structure	Within cliff band buffer	High
WUPA01459	Structure, Other	On Moenkopi hillslope beneath rock fall	Moderate*
WUPA01494	Structure	Mesa top	Low
WUPA01495	Burial/Grave/Inhumation	Unknown; did not visit	Unclassified
WUPA01496	Artifact Scatter	Unknown; did not visit	Unclassified
WUPA01497	Structure, Other	Within cliff band buffer	High
WUPA01498	Structure, Other	Unknown; did not visit	Unclassified

Site Number	Site Type	Location	Vulnerability
WUPA01499	Structure, Other	Thin layer of cinders overlaying Moenkopi bedrock	Low*
WUPA01500	Habitation, Protected	Mesa top	Low
WUPA01511	Structure, Other	Within cliff band buffer	High
WUPA01512	Habitation, Protected	Shallow cinder basin	Low*
WUPA01513	Structure, Other	Within cliff band buffer	High
WUPA01518	Structure	Unknown; did not visit	Unclassified
WUPA01519	Habitation	Within cliff band buffer	High
WUPA01520	Structure, Other	Within cliff band buffer	High
WUPA01521	Habitation, Open Air	Unknown; did not visit	Unclassified
WUPA01522	Check Dam	Adjacent to WUPA wash tributary bed	Low*
WUPA02674	Habitation, Open Air	Mesa top	Low

*Classification based on NPS archaeologist comments.

Table C2. A summary table of gully catchment characteristics and erosion ranking of yellow, orange, and red based on the change in median elevation (Figure 17). Additionally, archaeological sites that fell within the buffered region of a gully are provided.

Gully ID	Average Cliff Height (m)	Vegetation Cover in Catchment [A]	Catchment Material	Median Elevation Difference (m)	Archaeological Sites Within Buffer
1	1.6	low	Moenkopi	-0.351 [C]	–
2	2.0	low	Thin cinder cover	-0.337 [C]	–
3	1.9	low	Moenkopi	-0.431 [B]	–
4	2.2	low	Moenkopi	-0.344 [C]	–
5	2.3	low	Moenkopi	-0.343 [C]	–
6	2.0	medium	Moenkopi	-0.309 [D]	–
7	1.8	low	Moenkopi	-0.337 [C]	–
8	3.1	low	Thin cinder cover	-0.360 [C]	–
9	0	low	Moenkopi	-0.288 [D]	–
10	0	low	Blue-grey basaltic fragments with cinders	-0.325 [C]	–
11	0.9	medium	Blue-grey basaltic fragments with cinders	-0.327 [C]	–
12	1.8	medium	Thin cinder cover	-0.432 [B]	–
13	2.3	low	Cinders	-0.423 [B]	WUPA01381

Gully ID	Average Cliff Height (m)	Vegetation Cover in Catchment [A]	Catchment Material	Median Elevation Difference (m)	Archaeological Sites Within Buffer
14	0.9	low	Cinders	-0.493 [B]	–
15	2.5	high	Cinders	-0.381 [C]	–
16	2.0	low	Thin cinder cover	-0.440 [B]	–
17	1.8	medium	Cinders	-0.509 [B]	–
18	1.7	low	Thin cinder cover	-0.418 [B]	WUPA01447
19	2.8	medium	Thin cinder cover	-0.311 [C]	–
20	0.7	low	Thin cinder cover	-0.274 [D]	–
21	1.9	medium	Cinders	-0.327 [C]	WUPA01108
22	2.8	low	Moenkopi	-0.318 [C]	–
23	1.1	low	Cinders	-0.352 [C]	–
24	0.1	low	Moenkopi	-0.278 [D]	–
25	4.9	low	Moenkopi	-0.356 [C]	–
26	0	low	Moenkopi	-0.468 [B]	–
27	1.1	low	Cinders	-0.336 [C]	–
28	1.2	low	Thin cinder cover	-0.302 [D]	–
29	0	low	Moenkopi	-0.283 [D]	–

Gully ID	Average Cliff Height (m)	Vegetation Cover in Catchment [A]	Catchment Material	Median Elevation Difference (m)	Archaeological Sites Within Buffer
30	1.5	low	Moenkopi	-0.355 [C]	–
31	1.4	low	Thin cinder cover	-0.539 [B]	–
32	0.4	low	Cinders	-0.453 [B]	–
33	1.0	low	Cinders	-0.435 [B]	–
34	0.0	low	Moenkopi	-0.325 [C]	–
35	1.2	low	Moenkopi	-0.376 [C]	–

[A] Vegetation cover was recorded as a percentage from 0-100% and then classified as low (0-30%), medium (31-70%), and high (71-100%).

[B] Gullies ranked red eroded on average from 40-50 cm.

[C] Gullies ranked orange eroded on average from 30-40 cm.

[D] Gullies ranked yellow eroded on average 25-30 cm.